Vortex-Induced Vibration, Absence of Lock-in and Fluid Force Deduction

Thesis by

Mohammad Reza Gharib

In Partial Fulfillment of the Requirements
for the Degree of Doctor of Philosophy

California Institute of Technology
Pasadena, California

1999
(Submitted March 25, 1999)

To my mother Fatemeh Noroozi

Acknowledgements

I would like to thank my research advisor Professor Anthony Leonard for his great guidance, insight, and patience. He taught me simplicity and clarity through our numerous discussions. I was fortunate to have close contact with Professor Anatol Roshko who during many meetings gave me great direction and motivation. I thank Professor Morteza Gharib for the great inspiration and energy he invested in me. I would like to thank Dr. Flavio Noca for sharing his expertise in experimental techniques and Dr. Ron Henderson, Dr. Douglas Shiels and Mark Brady for their advice on computations. I also thank Professor Norden Huang who generously provided the Empirical Mode Decomposition software. Communications with Professor Theodore Wu and Professor Thomas Caughey were most fruitful. I thank Ali Kiany, Bahram Valiferdowsi, Joe Haggerty, and Larry Frazier for guiding me through machining parts and Steve Hasse for his help in designing the traverse and the optical setup. Many thanks go to Shahla Shahsavary and Jean Anderson at the Aeronautics Library for their help. Acknowledgements also go to Lory Cameron, Dimity Nelson, and Kathleen Hamilton for their administrative assistance. Christine Milrod helped me immensely both emotionally and technically throughout the writing process. Finally, I thank all my family members especially my mother, Fatemeh Noroozi, my brothers Shahrokh, Khosrow and Fereydoon Gharib for their continuous support throughout the years.

Abstract

Vortex-induced vibration (*VIV*) of elastically supported cylinders in cross-flow is studied experimentally for cylinder mass ratios (average cylinder density / fluid density), $2.1<m^*<72$. .For small mass ratios below 10, a new *VIV* mode is discovered which does not involve a lock-in behavior. The oscillation and the shedding frequencies coalesce and deviate slightly from the nominal Strouhal frequency of $St=0.2$ to smaller values with increasing free stream velocity U. With increasing mass ratio above 10 ($m^*>10$), the frequency growth with free stream velocity U appears to approach the lock-in limit while the amplitude and the frequency range of oscillations diminish. Additionally, a novel technique is employed to deduce the unsteady lift coefficient on the body using *VIV* time traces of the cylinder displacement and their numerical derivatives.

An analytical study of the dynamical equation shows that the oscillation amplitude (A/D) is inversely proportional to effective stiffness, $k^*_{eff}=(m^*/U^2)(1-(f/f_n)^2)$, where U represents the non-dimensional flow speed and f/f_n, the ratio of the oscillation to natural frequencies. It is hence maintained that at high mass ratio cases studied previously ($m^*>100$), lock-in behavior ($f/f_n \sim 1$ for $U \sim 1$) is a prerequisite for nominal vibration amplitudes. At low values of mass ratio, however, k^*_{eff} is minimized naturally without a need for lock-in.

Through a detailed study of a large number of cases with low to medium mass ratios in different experimental settings, it is additionally argued that lock-in is a sporadic phenomenon that appears at various mass ratios. The few occurrences of lock-in at low mass ratios with nominal damping and the unexpected absence of any oscillations at medium mass ratios ($m^* \sim 30$), except for a few cases exhibiting lock-in tendencies indicate that lock-in is not as common as classically believed.

Table of Contents

List of Figures

Symbols

A = cylinder oscillation amplitude

$A^* = A / D$ = non-dimensional cylinder oscillation amplitude

C_L = lift coefficient = $2 F_L / \rho_f U_\infty^2 D$

C_y =lift coefficient in y direction = $2 F_y / \rho_f U_\infty^2 D$

D = cylinder diameter

F_y = transverse force on cylinder

L = cylinder length

Re = *Reynolds* number = $U_\infty D / \nu$

St = Strouhal frequency = $f_s D/U_\infty$

$U = U_\infty/\omega_n D$ = non-dimensional flow speed

$U_{Amax} = U_\infty / \omega_{Amax} D$ = non-dimensional flow speed using ω_{Amax}

U_∞ = free stream velocity

$Y=y/D$ = non-dimensional displacement

b = damping coefficient

$b^* = m^* \zeta/U=2b/L/(\rho U_\infty D)$ = non-dimensional damping

f = oscillation frequency

f_s = shedding frequency

f_n = system natural frequency

f^* = non-dimensional cylinder oscillation frequency = $f D/ U_\infty$

k = spring constant

$k^* = k/L/(1/2 \rho_f U_\infty^2) = m^*/U^2$ = non-dimensional stiffness

$k^*_{eff} = k^* - (2\pi f^*)^2 m^* = (m^*/U^2)(1-(f/f_n)^2)$ = effective stiffness

$m = 1/4\ \pi \rho D^2$ = cylinder mass

m^* = non-dimensional mass coefficient = $2m/(\rho_f D^2 L)$

$t^* = tD/ U_\infty$ = non-dimensional time

$y^* = y/D$ = non-dimensional transverse cylinder position

ρ = cylinder density

ρ_f = fluid density

ϕ = phase fluid force and displacement

λ =oscillation wave length

ν = kinematic viscosity

$\tau = \omega_n t$ =non-dimensional time

$\omega_n = \sqrt{k/m} = 2\pi f_n$ = system natural frequency

ω_{Amax} = oscillation frequency at maximum amplitude

ω^* = non-dimensional oscillation frequency either $\omega D/U = 2\pi f^*$, or ω/ω_n

?$\zeta = b/\sqrt{km}$ = fraction of the critical damping

Abbreviations

EMD= Empirical Mode Decomposition (Huang [1998])

FFT = fast Fourier Transform

VIV = Vortex-induced vibration

WR= Williamson and Roshko [1988]

CHAPTER 1

Introduction

1. Introduction

Vortex shedding behind flexible bluff bodies occurs in many engineering situations, such as bridges, stacks, towers, transmission lines, offshore platforms, heat exchangers, marine cables, flexible risers in petroleum productions and other marine applications (see Blevins [1990], Ramberg and Griffin [1976]). The vortex wakes tend to be very similar regardless of the geometry of the structure. The shedding of vortices from alternate sides creates a periodic surface pressure fluctuation that can cause elastic structures to vibrate. Until recently, the legendary collapse of the Tacoma Narrows Bridge in Washington was attributed to vortex-induced vibration (*VIV*) (Billah and Scanian [1991]).

VIV is generally associated with the so called "lock-in" phenomenon, where the motion of the structure is believed to dominate the shedding process, thus synchronizing the shedding frequency. Lock-in is classically defined as the self-tuning of the vortices to the system natural frequency ($f_s \sim f_n$) within a certain range of stream velocities (Feng [1968]). Lock-in can also refer to the coalescence of the shedding, oscillation and the natural frequency of the system ($f_s \sim f \sim f_n$) for a range of flow speeds. Numerous studies in *VIV* literature support the common existence of lock-in (Blevins [1990], Griffin [1973], Brika and Laneville [1993] Blackburn and Henderson [1996]). Lock-in is a household term commonly believed to be achieved with any elastic structure in cross flow by varying the flow speed (Blevins [1990]).

Contrary to this conventional belief, a lock-in behavior as observed by Feng [1968] is absent from almost all cases encountered in the present study. In fact, a new *VIV* mode is discovered that does not rely on lock-in. It is shown that unlike the traditional belief, lock-in ($f \sim f_n$) is not the only cause of *VIV*. A more complete description for *VIV* involves minimizing a new parameter termed "effective stiffness", $k^*_{eff}=m^*/U^2(1-(f/f_n)^2)$, introduced by Gharib et al. [1997], where m^* is the structure to fluid mass ratio and U is the non-dimensional free stream velocity. With this definition, effective stiffness can be minimized through small values of m^* as well as a lock-in behavior ($f/f_n \sim 1$). Since most previous experiments involved large values of m^*, considerable *VIV* amplitudes could be observed if and only if lock-in occurred. At low mass ratios, *VIV* can occur with or without a lock-in behavior. Additionally, the absence of lock-in in most low mass ratio cases studied (chapter 4) and the large number of cases with medium mass ratios that exhibited no steady *VIV* indicate that lock-in is not as common a phenomenon as usually believed. When *VIV* is established at large mass ratios, however, it is accompanied with lock-in.

The preliminary experiments, *O1* and *O2*, described in chapter 5, involved low density cylinders in cross flow that did not show any signs of lock-in. The shedding frequency in these studies grew proportionally to the increasing flow speeds with a smaller than expected Strouhal number. This surprising no-lock-in phenomenon was initially attributed to either the low structural density or the two-degree-of-freedom (figure eight) motion of the cylinder. The reasoning behind the first hypothesis was that the motion of a light structure is probably dominated by the flow momentum. The latter was solely based on a main difference between the experimental setup at hand and those described in literature; a difference that could possibly bring about more system compliance to fluid forces. Since figure eight oscillation is more common in nature, such deviation from classical literature could have major consequences.

An experimental setup involving a variety of mass ratios and one or two-degree-of-freedom cylinder motion was designed to resolve the non-lock-in behavior. Early on, 1D oscillations were detected that involved no lock-in behavior. This eliminated the role of 2D vibration in the absence of lock-in. To reduce the number of structural parameters involved, main focus was turned to 1D oscillations, where with increasing values of the structural mass ratio, a gradual tendency to lock-in was observed (chapter 4). The oscillation amplitudes, however, seemed to dwindle with increasing mass ratios far from the values observed in Feng's experiment. This differentiated the low mass ratio cases at hand as a new *VIV* mode with no lock-in. The large amplitudes detected in Feng's experiment [1968] were solely due to lock-in.

Partial lock-in cases detected in few low mass ratio cases in chapter 5 proved that the occurrence of lock-in does not rely on the mass ratio either. This sporadic appearance of lock-in, however, is the only manner considerable *VIV* amplitudes can be achieved at large mass ratios.

In chapter 2, the basic concepts, the previous approaches and the new "effective stiffness" parameter are discussed in detail. Additionally, Empirical Mode Decomposition, a new signal processing tool for extracting frequency information is introduce at the end. In chapter 3, the experimental setup is described with detailed views in the appendix A.1. The one-dimensional results are presented in chapter 4 in increasing values of mass ratio m^*. The two dimensional results, along with the preliminary experiments providing the first signs of the non-lock-in response, are discussed in chapter 5. Chapter 6 concentrates on a new technique for deducing time-dependent fluid forces using the oscillation trace and dynamical system modeling is provided.

CHAPTER 2

Basic Concepts, Previous Work and Introducing Effective Stiffness

$$k^*_{eff} = -\omega^{*2} m^* + k^* = \frac{m^*}{U^2}\left(1 - \left(\frac{f}{f_n}\right)^2\right)$$

$$k^*_{eff}\ A^* = C_y$$

2. Basic Concepts, Previous Work and Introducing Effective Stiffness

In this chapter, we review the basic concepts such as bluff body wakes, vortex lock-in, non-dimensional parameters and the equations of motion relevant to vortex-induced vibration (*VIV*). We subsequently focus on previous studies and approaches such as the harmonic oscillator, computational simulations and forced oscillations experiments. We finally introduce the effective stiffness parameter, which is the central foundation for clarifying the *VIV* phenomena observed in this thesis. Through this novel parameter, we will explore the role of mass ratio in determining *VIV* amplitudes and the shedding frequency response.

2.1. Bluff Bodies and Vortex Shedding

Bluff bodies are blunt unstreamlined bodies that involve boundary layer separation in a free stream above a minimum *Reynolds* number. The fluid flow around two-dimensional bluff bodies usually involves shedding of spanwise vortices with alternate signs. The growth and movement of these vortices creates a fluctuating lift and drag force on the body. The non-dimensional shedding frequency, $St=f^*=fD/U_\infty$, where U_∞ is the free stream velocity and D the characteristic width of the body, is known as the Strouhal frequency. In the case of a stationary cylinder, the fluid force can closely approximate a periodic sine wave with a Strouhal frequency close to a constant value of $St\sim0.2$ for a large range of Reynolds numbers.

2.2. Flow-Induced and Vortex-Induced Vibration (*VIV*)

Any fluctuating fluid force on an elastic structure may cause flow-induced vibration with possible catastrophic consequences. The vortex-induced vibration (*VIV*) is a form of flow-induced vibration where the fluctuating lift force is due to vortex shedding and where the Strouhal frequency is close to the natural frequency of the system or a fraction thereof. As depicted in Figure 2.1, the body movement may affect the wake flow in a complicated manner resulting in an unpredictable fluid force. The connection between the vorticity field and the fluid force $F_y(t)$ is realized through the vorticity-momentum equation ($F\ (t) = \rho \frac{d}{dt} \int (\underline{x} \times \underline{\omega}(\underline{x})) d\underline{x}$ for a stationary body), where $\omega(x)$ represents the vorticity field and the integral is evaluated over the entire field. A modified version is available for an integral over a finite box encompassing the body (Noca [1996]). The relationship between the force $F_y(t)$ and the body movement can be imagined via a structural equation including a restoring force, inertia and damping. A simple case of such structure is an elastically held cylinder in cross flow with mass m, elastic stiffness k and a structural damping b with a fluctuating fluid force $F_y(t)$. The least understood portion of the *VIV* cycle in Figure 2.1 is the effect of the body displacement $y(t)$ on the vorticity field. This part can be viewed as a purely fluid mechanical problem involving the Navier-Stokes equations as commonly done in direct numerical simulations (*DNS*), or more simply as a vortex dynamic problem. In the latter view, knowledge of vortex patterns and properties is employed to obtain a simple physical understanding of the phenomenon. Experiments involving forced prescribed motions $y(t)$ of a cylinder attempt to achieve such understanding.

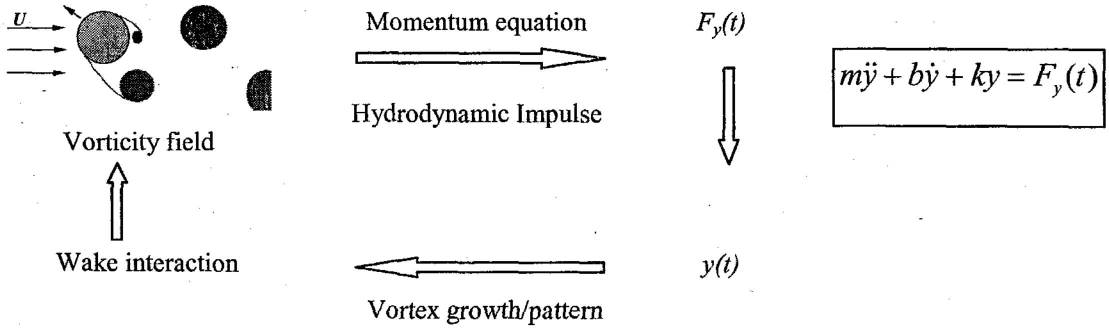

Figure 2.1 Vortex-induced vibration and movement-induced vorticity

2.3. Vortex Lock-in

Vortex lock-in is traditionally described as the coalescence of the Strouhal shedding frequency and the structural frequency, such that for a range of free stream velocities, the shedding frequency tunes or locks itself to the natural frequency of the structure. It is believed that the motion of the body affects the vortex shedding pattern such that the vortices are shed at the frequency of structural motion. The phenomenon is thought to allow a wider range of velocities for a system resonance with possible catastrophic consequences. Lock-in has been observed in numerous laboratory experiments and flow simulations involving cables, cantilevers, bridge models, and elastically held cylinders performing one- and two-degree-of-freedom oscillation (Feng [1968], Griffin [1973], King and Prosser [1972], Blevins [1990], Brika and Laneville [1993], Blackburn and Henderson (1996)). Feng's experiment involved self-excited vibration of a cylinder in a wind tunnel while Blackburn and Henderson studied two-dimensional oscillation of a cylinder with $m^*=10$ at $Re=250$ through numerical simulation.

2.4. Effects of Structural Motion on Vortex Wake

Free or Forced cross stream vibration of a circular cylinder with frequencies near the vortex shedding frequency has pronounced effects on the shedding process (Sarpkaya [1979], Williamson and Roshko [1988], Blevins [1990], Griffin and Hall [1991], Henderson and Blackburn (1998)). In general, cylinder vibration, at sufficiently large amplitudes, can affect the vortex growth period and phase, resulting in stronger vortices with altered patterns. It can increase the drag, lift and the spanwise correlation of the wake. The three-dimensionality is suppressed and the near wake is more organized. Within a range of forced oscillation amplitudes and frequencies, the shedding frequency may be shifted to, or even be synchronized with, the vibration frequency. The effects are less pronounced when the vibration frequency equals a multiple or a submultiple of the shedding frequency. Large amplitude forced cylinder vibrations can shift the vortex shedding frequency by as much as 40%. Such effects are not limited to circular cylinders. The vortices are usually shed near the maximum cylinder displacement. There is also an abrupt 180 degrees shift in phase as the oscillation frequency passes through the Strouhal shedding frequency (Bishop and Hassan [1964], Zdravkovitch [1982], Ongoren and Rockwell [1988]). At amplitudes above one-half diameter, a break up of the symmetric vortex patterns has been observed and interpreted as a self-limiting fluid force behavior at large amplitudes (Griffin and Ramberg [1974], Williamson and Roshko [1988], Griffin and Hall [1991]). As presented in chapter 5, however, vibration amplitudes above one diameter are in fact possible. Vortex synchronization may also occur in stream-wise as well as rotational oscillations of a cylinder. Figure 2.2 shows the increased lift in arbitrary units in the forced oscillation experiments of Bishop and Hassan [1964].

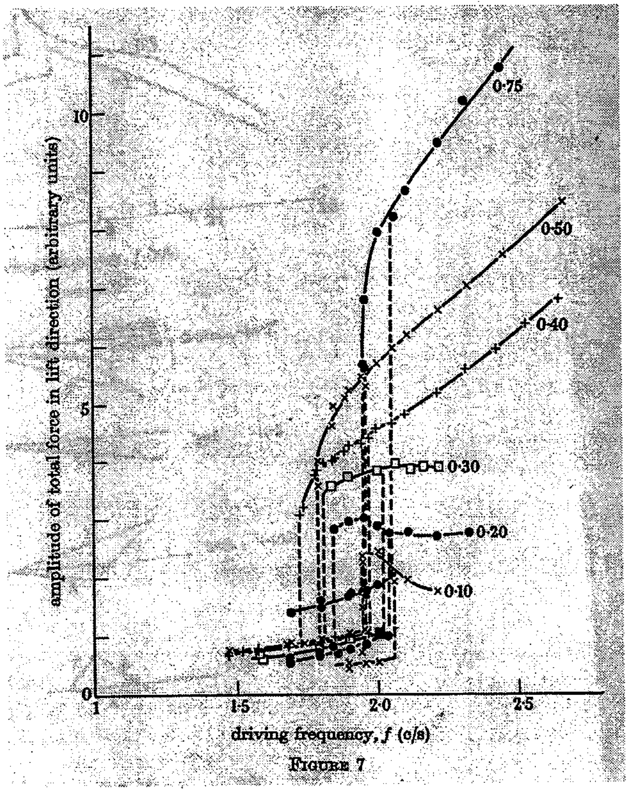

Figure 2.2 Increased lift in forced oscillation of a cylinder in cross flow, lift vs. forcing frequency for $0.10<A/D<0.75$ (Bishop and Hassan [1964])

2.5. Dimensional Analysis

Figure 2.3 and Equation 2.1 present a list of related parameters in the *VIV* problem. The input parameters are geometry and dimensions of the body, D and L, the structural stiffness k, damping b, and mass m, the free stream velocity U_∞, fluid viscosity ν and the fluid density ρ_f.

$$A, f = F(D, L, k, b, m, U_\infty, \nu, \rho_f; geometry) \qquad \textbf{Equation 2.1}$$

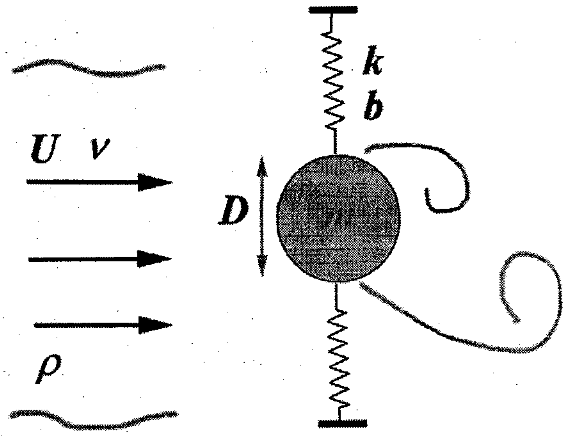

Figure 2.3 Flow-structure parameters in *VIV*

Since there are three fundamental dimensions in the problem (time, length and mass), there need to be five non-dimensional input parameters present in the problem. In Equation 2.2, the most relevant input parameters (D, b, m, U_∞, ν) are non-dimensionalized using $(L, \rho_f$, and $k)$ where $\omega_n = 2\pi f_n = (k/m)^{1/2}$.

$$\frac{A}{D}, \frac{f}{f_n} = f(\frac{D}{L}, \frac{U_\infty D}{\nu}, \frac{m}{\rho_f D^2 L}, \frac{b}{\sqrt{km}}. \frac{U_\infty \sqrt{m}}{\sqrt{k}D}) \qquad \textbf{Equation 2.2}$$

renaming terms:

$$A/D, f/f_n = f(D/L, Re, m^*, \zeta, U) \qquad \textbf{Equation 2.3}$$

where

$$m^*=\frac{2m}{\rho_f D^2 L},\ \zeta=\frac{b}{2\sqrt{km}},\ U=\frac{U_\infty}{\sqrt{k/mD}}=1,\ Re=\frac{U_\infty D}{\nu}$$ **Equation 2.4**

The parameter m^* is the cylinder to fluid mass ratio, ζ is the fraction of the critical damping and U is the non-dimensional free stream velocity. It is also possible to non-dimensionalize the parameters using U_∞ and D so that they are valid at vanishing values of k and m (section 2.9). The structural damping $\zeta=0.5(b/\sqrt{(km)})$ is usually about a few percent.

Since experiments are usually performed in either air or water, the values of fluid density ρ_f and ν are fixed. The damping b is usually due to the elastic structural components such as cantilevers and springs and hence affected by varying k. In general, changing any of the physical parameters ($D, L, k, b, m, U_\infty, \nu, \rho_f$) except ρ_f in an experiment can affect more than one of the non-dimensional parameters (m^*, ζ, U, Re). Varying ρ_f would only affect viscosity ν in an indirect way.

In most materials including metals, structural damping is due to a variety of phenomena that usually dissipate an amount of energy per cycle proportional to A^2, but weakly dependent on frequency ω [Bert 1973]. The textbook viscous damping term by' is simply a dissipative model and not realistic. The mass ratio m^* is mostly $O(1)$ in hydrodynamic applications and $O(10^2)$ in aeroelastic experiments. Since $U=U_\infty/(2\pi f_n D)= 1/(2\pi f^*)\ (f/f_n)$, and $f/f_n \sim 1$ in *VIV* and $f^* \sim 0.2 \sim 1/(2\pi)$, U is usually close to 1 ($U \sim 1$) in *VIV*. It is worth noting that in laboratory experiments, a single-frequency periodic motion may not always be realized and in fact, multiple frequencies co-exist (Chapter 4).

To simplify Equation 2.3, one may assume that the output parameters are less sensitive to the *Reynolds* number (*Re*) and three-dimensional effects (*L*). Since U is usually close to one in *VIV*, one may consider a fixed value of U where the amplitude A/D is the maximum.

$$A_{\max}/D,\ f/f_n = f(m^*, \zeta)$$ **Equation 2.5**

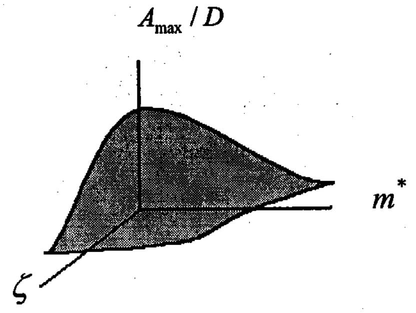

Figure 2.4 Maximum oscillation amplitude A_{max}/D vs. m^* and ζ (conceptual)

Conceptually, the A_{max}/D defines a surface as a function of ζ and m^* (Figure 2.4). The oscillation amplitude at zero mass ratio and damping is finite due to the added mass effect due to body acceleration. The amplitude can reasonably be assumed to diminish with increasing structural mass ratio or damping. The added mass is sometimes included in the mass ratio values reported in literature (Blevins [1990]).

Many scholars such as Griffin [1973] have considered the dependence of A_{max}/D on a single parameter $S_G = 2\pi m^*\zeta$ known as the mass-damping or the Scruton number. Gharib et al. [1997] and Shiels [1998] have computationally explored the limiting cases of zero mass and/or zero damping. In such limits, the number of parameters is reduced and the effects of m^* and ζ can be studied separately (see section 2.9).

2.6. Differential Equation of Motion

The fluid-structure system can be treated as a mechanical system with a fluid forcing function

$$m\ddot{y} + b\dot{y} + ky = 1/2 c_y(t)\rho_f U_\infty^2 DL$$ **Equation 2.6**

where the terms on the left-hand side represent the mechanical system and the terms on the right-hand side are due to the fluid. Letting

$$y = DY\,,\ \tau = \omega_n t\,, \qquad \partial/\partial t = (\partial\tau/\partial t)\,(\partial/\partial\tau) = \omega_n\,\partial/\partial\tau$$

Equation 2.7

and substituting in Equation 2.6 gives:

$$mD\omega^2{}_n\ddot{Y} + b\omega_n D\dot{Y} + kDY = 1/2\,C_y(t)\rho_f U_\infty^2 DL$$

Equation 2.8

$$\ddot{Y} + \frac{b}{m\omega_n}\dot{Y} + \frac{k}{m\omega^2{}_n}Y = C_y(t)\frac{U_\infty^2}{\omega^2{}_n}\frac{\rho_f L}{2m}$$

Equation 2.9

multiplying the right-hand side by D^2/D^2 and reorganizing m^*:

$$\ddot{Y} + \frac{b}{m\omega_n}\dot{Y} + \frac{k}{m\omega^2{}_n}Y = C_y(t)\left(\frac{U_\infty}{\omega{}_n D}\right)^2\frac{\rho_f LD^2}{2m}$$

Equation 2.10

after renaming terms:

$$\ddot{Y} + 2\zeta\dot{Y} + Y = \frac{U^2}{m^*}C_y$$

Equation 2.11

where the following identities are valid as before

$$2\zeta = \frac{b}{m\omega_n}\,,\ U = \frac{U_\infty}{\omega_n D}\,,\ m^* = \frac{2m}{\rho_f LD^2}\,,\ \omega_n = \sqrt{\frac{k}{m}}$$

Equation 2.12

The dot in $\dot{Y}$ refers to a derivative with respect to τ. As seen in Equation 2.11, the fluid force is inversely proportional to the mass ratio m^* and hence quite small in aeroelastic applications (m^*>100). The free stream velocity U is close to 1 in *VIV* as mentioned before.

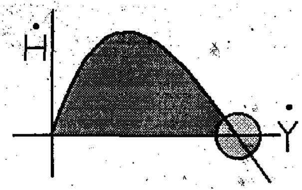

$$\dot{H} = \frac{d}{dt}\frac{1}{2}(Y^2 + \dot{Y}^2) = \frac{U^2}{2m^*}C_y\dot{Y} - 2\zeta\dot{Y}^2 \qquad \textbf{Equation 2.13}$$

Figure 2.5 ***VIV*** **equilibrium**

The energy conservation equation is given in Equation 2.13, where $\frac{d}{dt}\frac{1}{2}(Y^2 + \dot{Y}^2)$ represents the rate of change of the energy stored in the system and $\frac{U^2}{2m^*}C_y\dot{Y} - 2\zeta\dot{Y}^2$ is the work done by the fluid minus the energy dissipated by the structure per unit time. Since any damping model has a negative contribution, it is imperative that $C_y\dot{Y}$ on average have a positive value for *VIV* to occur, that is C_y and $\dot{Y}$ must hold a phase difference $|\phi|<\pi/2$ and as close to zero as possible. As shown in Figure 2.5, assuming C_y is independent of $\dot{Y}$, the system has one equilibrium point for *VIV* where $<\dot{H}>=0$. Since C_y is on the order of 1, a maximum $\dot{Y}$ value from $\frac{U^2}{2m^*}C_y\dot{Y} - 2\zeta\dot{Y}^2 = 0$ requires a minimum value of $\frac{m^*\zeta}{U^2}$ which is related to and sometimes used as the mass-damping, S_G parameter mentioned in section 2.5. Although this parameter may affect the amount of energy input into the system, it may not solely be responsible for the maximum amplitude of vibration achieved. The lift coefficient C_y has been shown to have unpredictable behavior at various values of oscillation frequency and amplitude (Gharib et al. [1997]).

2.7. Previous Studies

In this section, we briefly summarize some of the general experimental and numerical approaches used in the literature. Experimental methods usually involve either forced or free vibrations of a cylinder in cross flow and the theoretical approaches range from simple harmonic (sine wave) wake forces to complex Navier-Stokes solvers.

2.7.1. Harmonic Oscillator

This technique models vortex shedding as a harmonic lift force at a fixed or amplitude-dependent lift coefficient $C_L(A^*)$ (Blevins and Burton [1976]). It gives consistent results for maximum amplitudes A^*_{max} when $C_L(A^*)$ is obtained from free elastic experiments. It does not model lock-in and is limited to resonance. The technique is often modified to include a phase in lift force C_L. That is the lift component is assumed to have two components in and out of phase with the displacement $y^*(t)$ (Sarpkaya [1978], Staubli [1983], Moe and Wu [1990]). The force components are calculated by fitting lift force traces from forced oscillation experiments to terms in and out of phase with the displacement. This method assumes amplitude-dependent lift and vortex synchronization, that is the fluid and the structure are assumed to be synchronized. This method does not model near-resonant behavior.

2.7.2. Fluid or Wake Oscillator Models

In fluid oscillator models, vortex shedding is represented as a non-linear, usually van der Pol type, oscillator that is self-limiting (Hartlen and Currie [1970]). The wake oscillator *ODE* is usually forced through cylinder displacement velocity (Parkinson [1972]) as:

$$\ddot{C}_y - A\Omega_0\dot{C}_y + B/\Omega_0\dot{C}_y^3 + \Omega_0{}^2C_y = D\dot{Y}$$ **Equation 2.14**

In this equation, $\Omega_0 = f_s/f_n$ is the ratio of the shedding to natural frequency and A, B, and D are constants obtained from stationary and forced cylinder experiments (Smirnov and Pavlihina [1957], Bishop and Hassan [1964], Jones [1968], Tanaka and Tanahara [1969]). Some physical basis for this model comes from the fact that it produces a sinusoidal lift coefficient for a stationary cylinder where the forcing term is zero and a self-limiting behavior through the van der Pol nonlinearity. Wake oscillator is an ad hoc model simplifying the complicated separated flow by a simple one-degree-of-freedom equation and a "poor man's computational flow solution" (Blevins [1990]). It fails to capture many aspects of *VIV* in a convincing manner. A few researchers (Berger [1987], Griffin and Skop [1973], Hall and Iwan [1984]) have produced various modifications to this model with limited improvements.

2.7.3. Vortex Patterns and the Williamson-Roshko (*WR*) Plane

A classical experiment by Bishop and Hassan [1964] involved forced oscillations of a cylinder in cross flow. By studying the unsteady forces through a force balance, the fluid force and phase were examined for a set of oscillation amplitudes and frequencies (see Figure 2.2). An abrupt shift in phase and a large increase in lift and drag forces were observed as the oscillation frequency was swept through the shedding frequency in cross flow.

Following the same thought, Williamson and Roshko (*WR*) [1988] studied patterns of vortex shedding from a towed cylinder forced in sinusoidal motion for a large variety of oscillation amplitudes and frequencies. No force or vorticity field measurements, however, were made. Figure 2.6 shows the resulting plane, where the vertical axis represents the forced oscillation amplitude *A/D* and the horizontal axis indicates the oscillation to shedding period ratio, *T/Ts* (or alternately, the towed distance traveled, λ/D). Vortex patterns of two alternate single vortices and two pairs (or two stretched single) per shedding cycle are indicated as *2S* and *2P* while *P+S* refers to a pair and single vortices shed in one shedding cycle. The usual von Karman *2S* pattern is naturally recovered at small amplitudes and/or small frequencies.

It was found that the resonance region explored by Bishop and Hassan [1964] lies across the boundary between the *2S* and *2P* regions. According to Williamson [1988], the critical curve in Figure 2.6 corresponds to the transition from *2S* to *2P* while I and II are curves where the forces on the body show a sharp “jump” in Bishop and Hassan’s experiment [1964]. The changes observed in the lift and drag forces could hence be attributed to the change in vortex shedding pattern.

A series of computational experiments were later conducted by Blackburn and Henderson [1996] at a low Reynolds number of $Re=250$ crossing the presumed *2S-2P* boundary. The results ranged from stable asymmetric *2S* and *S+P* patterns to transient ones with no steady *2P* modes. It is worth noting that λ/D in free oscillation studies is equivalent to $1/f^*$

$$\lambda/D=U_\infty T/D=(fD/U_\infty)^{-1}=1/f^*$$

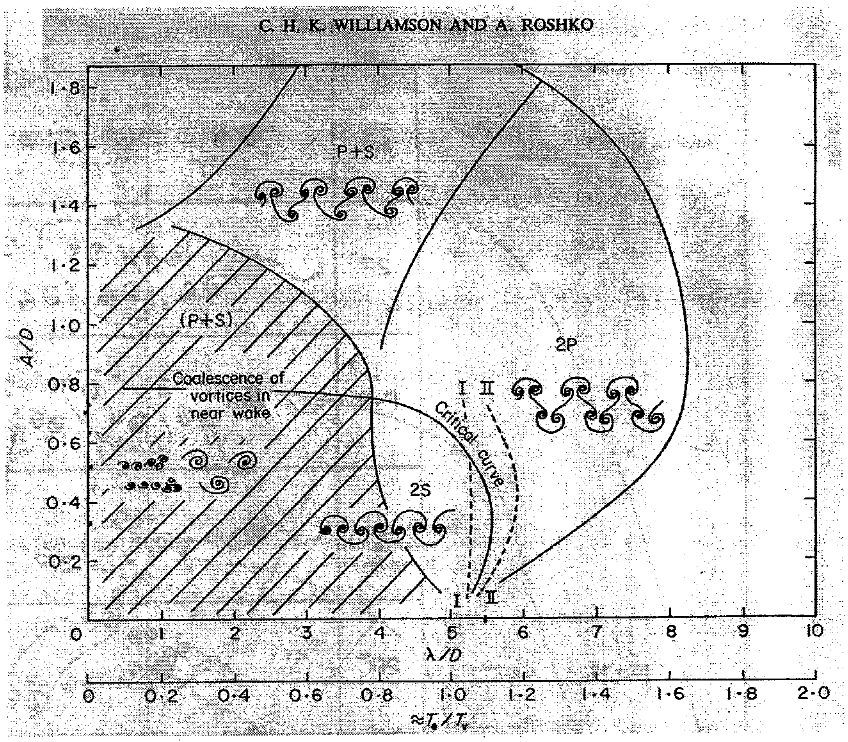

Figure 2.6 Williamson and Roshko plane [1988], forced oscillation shedding modes, *A/D* vs. *λ/D* (non-dimensional distance traveled)

Since f^* in free *VIV* experiments is usually shifted to values less than 0.2 ($f^*<0.2$, Feng [1968], Shiels [1998]), λ/D tends to shift to $\lambda/D>5$ at large amplitudes. It is also plausible that the vortex pattern and lift coefficient results for a forced experiment (pure sine wave) may differ from those observed in a free elastic oscillation (quasi-periodic oscillations with co-existing shedding and structural frequencies).

2.7.4. Direct Numerical Simulations

Computational Fluid Dynamics (CFD) employs a variety of techniques including discrete vortex (Sarpkaya [1989], Blevins [1991]) and vortex blob methods (Shiels [1998]), as well as grid-based finite-difference (Hall and Griffin [1993]) and spectral element techniques (Newman and Karniadakis [1996], Blackburn and Henderson [1996]), to achieve flow field solutions to the Navier-Stokes equations. The lift force computed from the surface pressure on the cylinder or the hydrodynamic impulse within a box encompassing the cylinder are used to obtain the cylinder motion through an assumed structural equation. Despite the valuable detailed information provided by such techniques, the flow-structure problems are usually limited to low Reynolds number values. Figure 2.7 shows the root-mean-square values for *A/D* and the oscillation frequency response in the two-degree-of-freedom *VIV* simulation by Blackburn and Henderson.

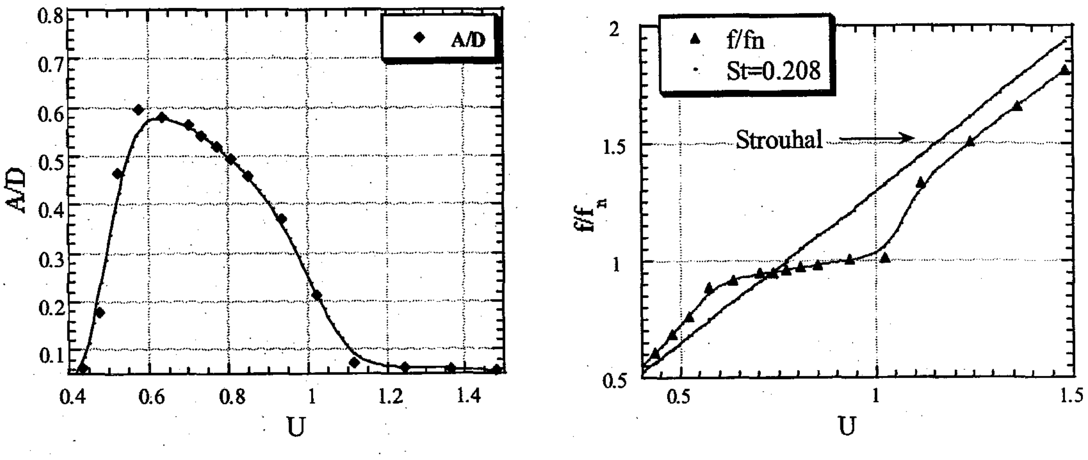

Figure 2.7 *A/D* (rms) vs. *U*, 2D, *x* and *y* oscillations, *Re*=250, ζ=0.01, m^*=20, *St*=0.2077 (Blackburn and Henderson [1996])

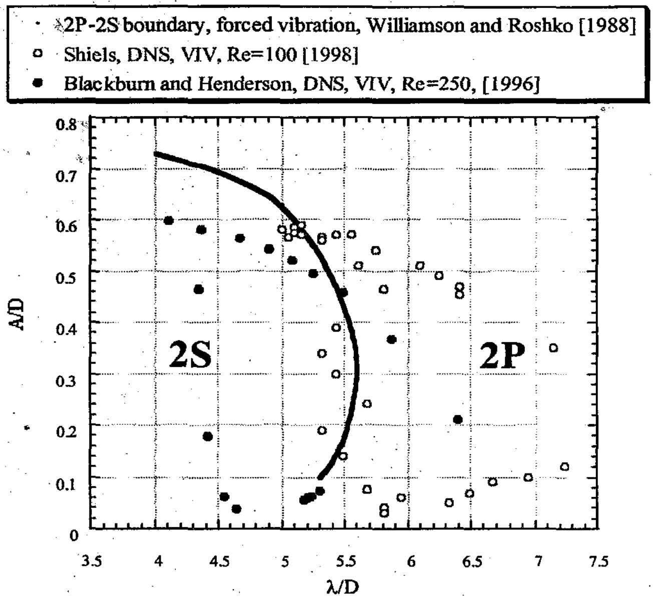

Figure 2.8 Computational *VIV* results at *Re*=100 and *Re*=250 on the Williamson-Roshko plane using $\lambda/D = 1/f^*$

Figure 2.8 shows the free *VIV* computational results of Shiels [1998] and Blackburn and Henderson [1996] on the *WR* plane. Since the Strouhal shedding frequency ($St=(\lambda/D)^{-1}$) for a stationary cylinder ($A/D=0$) is 0.208 at *Re*=250 and slightly lower (*St*=0.172) at *Re*=100, we observe a shift in values of λ/D between the two studies. Despite the two-dimensional nature of oscillations in the BH data and the difference in the Reynolds numbers, the A/D-λ/D (or A/D-f^*) domain seem to be quite similar. Unlike experimental studies, every point in both studies was started from rest. The *2P-2S* boundary is purely for reference. Shiels reported single vortex wakes only. It is noteworthy that unlike most laboratory experiments, both studies seem to present deviations from the nominal Strouhal shedding to larger values (f^*_{VIV}>nominal *St*, Figure 2.7).

2.7.5. Passive *VIV* Experiments

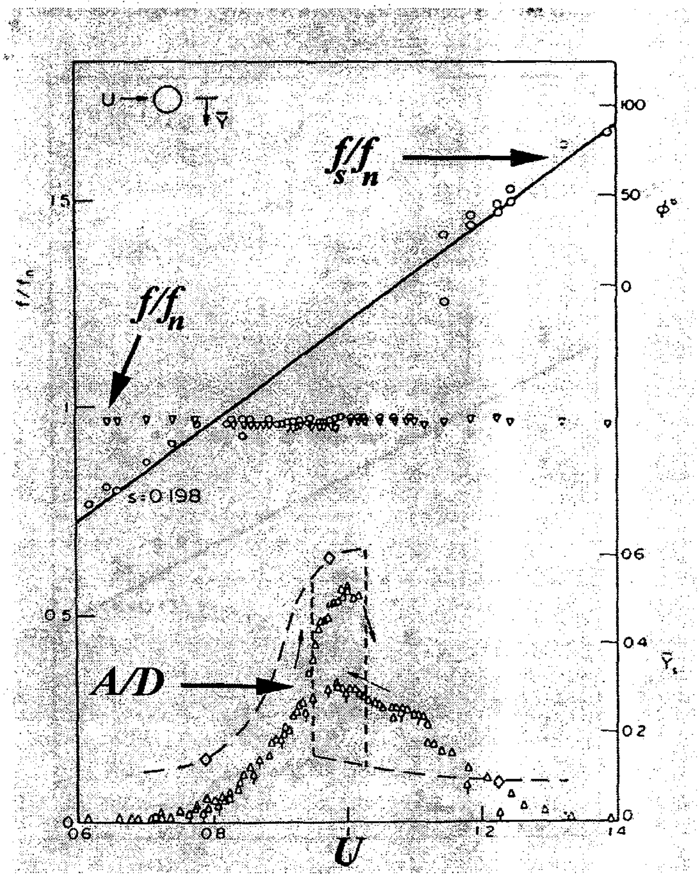

Figure 2.9 Feng's experimental data, $A/D=\Delta$, $f_s/f_n=\circ$, $f/f_n=\nabla$, $C_y=\diamond$, vs. U (ref. Parkinson [1989])

Measurements on scaled laboratory models (Griffin and Ramberg [1982], Blevins [1990]) or explorative studies are usually made on elastically supported cylinders. They include elastically held circular cylinders limited in one dimension (Feng [1968], Khalak and Williamson [1997]), two dimensions (Sarpkaya [1995]), or flexible cantilevers in cross flow (King and Prosser [1972], Brika and Laneville [1993]). The non-dimensional parameters involved are A/D, $f/f_n=f(D/L, Re, m^*, \zeta, U)$ as mentioned before. Detailed flow information such as the vorticity field can be obtained using Digital Particle Image Velocimetry (*DPIV*). The unsteady fluid forces can be calculated using a force balance connected to the model. Such experiments are limited by scale and non-zero values of the viscous or structural damping. The application of a force balance and a *DPIV* setup, although immensely helpful, can be quite challenging. Figure 2.9 shows results by Feng [1968] and Figure 2.10, additional data by Feng and Parkinson [1972] as quoted by Berger [1987].

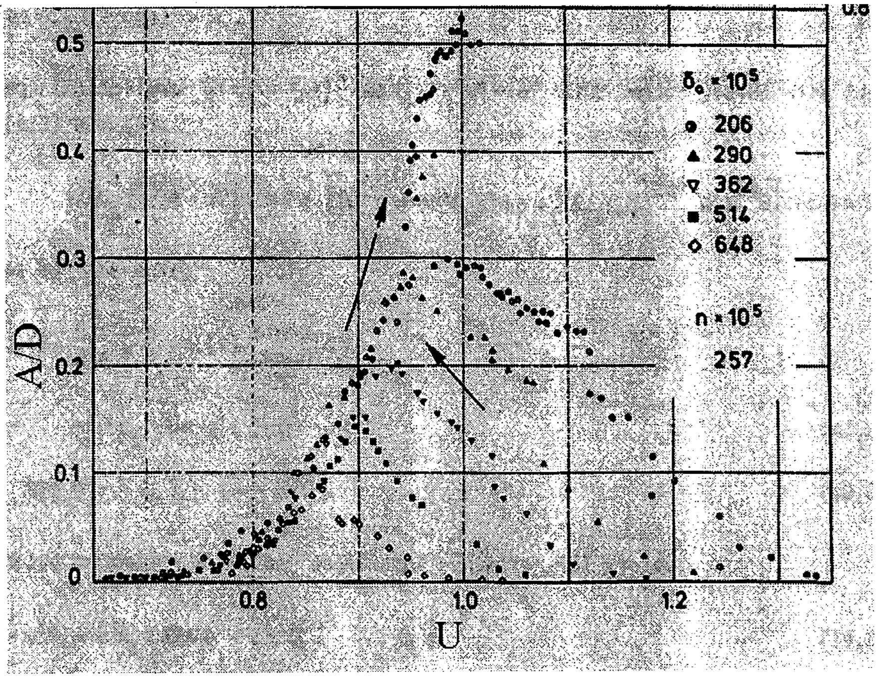

Figure 2.10 Oscillation amplitude A/D vs. free stream velocity U for various damping parameters ($0.0206<\delta=2\zeta<0.0648$, $m^*=1/n=389$, additional data by Feng quoted by Berger [1987], not present in other papers)

Figure 2.11 shows the cantilever results by Brika and Laneville [1993] on the Williamson and Roshko plane. In this case, since f/f_n is very close to 1 (lock-in), $\lambda/D=2\pi U$.

To overcome limitations with mass ratio and damping, Hover and Triantafyllou [1997] combined force-feedback with on-line numerical simulation to create a virtual structure in a water tunnel.

Most experiments have reported the existence of the lock-in behavior at various values of mass ratio and damping. Experiments conducted by Feng [1968] and Brika and Laneville [1993] also reported a hysteretic behavior indicating the importance of history (as in the direction, in which a certain flow speed U is approached). Khalakh and Williamson [1997] also reported the possibility of multiple branch behavior (oscillation modes) at low values of mass and damping. Brika and Laneville [1993] and Tamura [1998] have pointed out the effects of initial displacement on the final *VIV* amplitude. The Reynolds number is usually treated as a less important factor. Complex wake conditions such as large variations in the size of the near wake in range $2000<Re<5000$ have been observed by various researchers (Norberg [1994]).

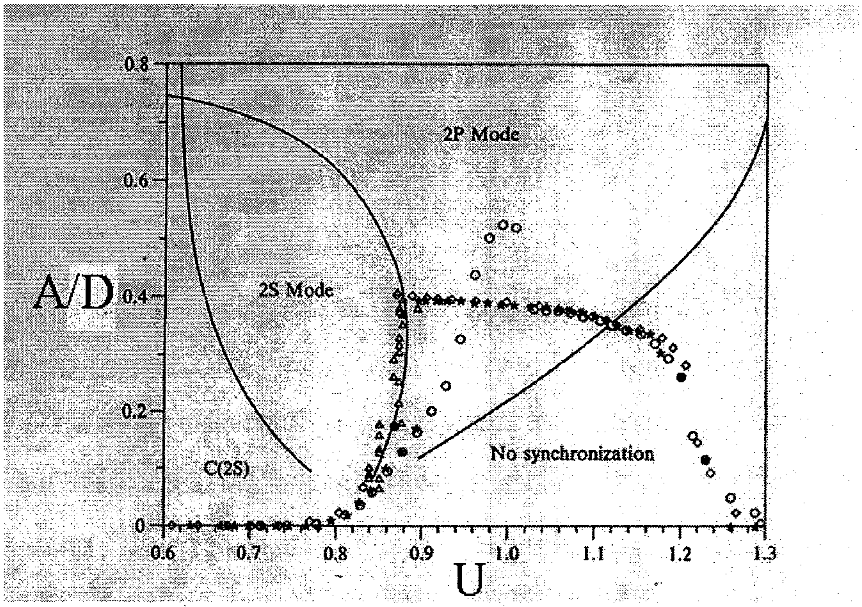

Figure 2.11 One-dimensional oscillations of a cantilever (Brika and Laneville [1993]) on *WR* plane

2.8. Empirical Mode Decomposition (*EMD*) and Quasi-Periodicity

Empirical Mode Decomposition (*EMD*) is a modern technique for extracting modes with different frequency scales from a given experimental signal (Huang [1998]). It employs a sifting technique connecting the local extrema (or alternatively the inflection points) within a trace as a measure of the characteristic time scales and possible intrinsic modes. Through successive iterations, *EMD* extracts components with different time scales that are numerically orthogonal and complete. *EMD* is capable of extracting such phenomena as sudden jolts, different sources of noise, intermittency, and most important of all various source signals arising from different physical phenomena. *EMD* is an alternative to the well-known Fast Fourier Transform (*FFT*) and Wavelet Spectrum. *EMD* replaces the idea of a sinusoidal fundamental with higher harmonics with that of a non-linear or quasi-periodic signal that is not necessarily stationary. The sifting technique can be combined with Hilbert transform to obtain time-dependent frequency and amplitudes. *EMD* signal processing has produced invaluable results in various areas from earthquake engineering to environmental and non-linear mechanics. Empirical Mode Decomposition will be used in chapter 4 to analyze the separate effects of fluid and structural forces and the nature of quasi-periodicity within *VIV* signals.

2.9. Introducing Effective Stiffness

In order to have valid parameters at vanishing values of k and m and also to separate the contribution due to structural forces, inertia, stiffness, and damping and the fluid force, Gharib et al. [1997] and Shiels [1998] non-dimensionalized time and other parameters using flow variables D and U_∞. This resulted in development of a new non-dimensional parameter called effective stiffness. Effective stiffness k^*_{eff} relates the lift force C_y to the oscillation amplitude A/D ($C_y = k^*_{eff}\ A/D$) just as a spring stiffness relates an exterior force F to the spring displacement y ($F = -ky$). This concept is the central part of the arguments behind *VIV* phenomena observed in the present work. Starting with the dimensional *ODE* in Equation 2.6:

$$m\ddot{y} + b\dot{y} + ky = 1/2\, C_y(t)\rho_f U_\infty^2 DL$$

Equation 2.15

and using U_∞/D and D to non-dimensionalize time and space:

$$y = DY,\ t^* = tU_\infty / D,\ \partial/\partial t = (\partial t^*/\partial t)\ (\partial/\partial t^*) = U_\infty/D\ \partial/\partial t^*$$

Equation 2.16

through substitution, one obtains:

$$\frac{mU_\infty^2}{D^2}D\ddot{Y}+\frac{bU_\infty}{D}D\dot{Y}+kDY=1/2\,C_y(t)\rho_f U_\infty^2 DL$$ **Equation 2.17**

simplifying and dividing by the right-hand side terms,

$$\frac{m/L}{1/2\,D^2\rho_f}\ddot{Y}+\frac{b/L}{1/2\,\rho_f U_\infty D}\dot{Y}+\frac{k/L}{1/2\,\rho_f U_\infty^2}Y=C_y(t)$$ **Equation 2.18**

renaming terms

$$m^*\ddot{Y}+b^*\dot{Y}+k^*Y=C_y$$ **Equation 2.19**

where

$$m^*=\frac{m/L}{1/2\,D^2\rho_f},\ b^*=\frac{b/L}{1/2\,\rho_f U_\infty D},\ k^*=\frac{k/L}{1/2\,\rho_f U_\infty^2}$$ **Equation 2.20**

Comparing identities in Equation 2.12 and Equation 2.20

$$k^*=\frac{m^*}{U^2},\ b^*=\frac{2m^*\zeta}{U},\ m^*=\frac{m/L}{1/2\,D^2\rho_f},\ f^*=\frac{fD}{U_\infty}=\frac{1}{2\pi U}\frac{f}{f_n},\ A^*=\frac{A}{D}$$ **Equation 2.21**

Alternately, comparing the coefficients in Equation 2.11, $\frac{m^*}{U^2}(\ddot{Y}+2\zeta\dot{Y}+Y)=C_y$, and Equation 2.19, $m^*\ddot{Y}+b^*\dot{Y}+k^*Y=C_y$, while distinguishing the difference between derivatives with respect to t^* and τ ($\partial Y/\partial\tau=U\ \partial Y/\partial t^*$) makes the first two identities in Equation 2.21 evident.

Assuming a sinusoidal oscillation, $Y(t^*)=A^*\sin(\omega^* t^*)$, and fluid force with a phase ϕ, $C_y(\tau)=C_{y0}\sin(\omega^* t^*+\phi)$, we proceed with Equation 2.19 by substitution:

$$-\omega^{*2}m^{*}A^{*}\sin(\omega^{*}t^{*})+b^{*}\omega^{*}A^{*}\cos(\omega^{*}t^{*})+k^{*}A^{*}\sin(\omega^{*}t^{*})= C_{y}\sin(\omega^{*}t^{*})\cos(\phi)+C_{y}\cos(\omega^{*}t^{*})\sin(\phi)$$ **Equation 2.22**

Since the above identity is true for all values of t^*, coefficients in front of $sin(t^*)$ and $cos(t^*)$ must be equal.

$sin(\omega^* t^*)$: $$(-\omega^{*2}m^{*}+k^{*})A^{*}=C_{y}\cos(\phi)$$ **Equation 2.23**

$cos(\omega^* t^*)$: $$b^{*}\omega^{*}A^{*}=C_{y}\sin(\phi)$$ **Equation 2.24**

The term $k^{*}{}_{eff}=-\omega^{*2}m^{*}+k^{*}$ is called the effective stiffness. Since $k^{*}=\frac{m^{*}}{U^{2}}$ and $\omega^*=\omega D/U_\infty=\omega/\omega_n(1/U)$ the effective stiffness may be related to the classical parameters in the following manner:

$$k^{*}{}_{eff}=-\omega^{*2}m^{*}+k^{*}=\frac{m^{*}}{U^{2}}\left(1-\left(\frac{f}{f_{n}}\right)^{2}\right)$$ **Equation 2.25**

In a series of computational experiments, Gharib et al. [1997] and Shiels [1998] showed that at vanishing values of b^*, the fluid may respond through a single frequency f^* (pure sine wave response) making $k^{*}{}_{eff}$ the universal fluid-structural parameter through $k_{eff}^{*}A^{*}=C_{y}$. That is varying values of m^* and k^* independently while keeping $k^{*}{}_{eff}=-\omega^{*2}m^{*}+k^{*}$ constant resulted in the same flow field, oscillation amplitudes and frequencies. The C_y behavior, however, was found quite unpredictable.

$$k_{eff}^{*}A^{*}=C_{y} \qquad (\text{for } b^*=0)$$ **Equation 2.26**

$$k^{*}{}_{eff}=-\omega^{*2}m^{*}+k^{*}$$ **Equation 2.27**

In the presence of damping b^*, Equation 2.24 gives

$$\left(k_{eff}^{*\,2} + (b^*\omega^*)^2\right)A^{*2} = C_y^{\,2}$$ **Equation 2.28**

$$\tan(\phi) = b^*\omega^* / k_{eff}^*$$ **Equation 2.29**

The existence of the damping parameter directly influences the phase ϕ and indirectly modifies the lift coefficient C_y and the frequency f^*. It is also noteworthy that $b^*=2\zeta m^*/U$ is similar to the mass-damping parameter, $S_G=2\pi m^*\zeta$, introduced before.

2.9.1. Effective Stiffness and Zero Mass and Damping

Gharib et al. [1997] and Shiels [1998] used the idea of zero mass and/or damping to explore the relative importance of the two parameters. Non-dimensionalizing the variables using D and U_∞ was necessary for exploring such limits and provided a new tool for considering individual force components (m^*, b^*, k^*, and C_y). At vanishing values of damping ($b^*=0$), flow responses close to a pure sine wave resulted in a simple solution to the flow-structure equation in Equation 2.19 in the following form.

$$k_{eff}^* A^* = C_y \qquad (\textit{for } b^*=0)$$ **Equation 2.30**

where the effective stiffness $k^*_{eff} = -\omega^{*2} m^* + k^*$ became the singular structural parameter. A unique amplitude response A^* was obtained for every value of k^*_{eff} regardless of the individual values of mass or stiffness (Figure 2.12).

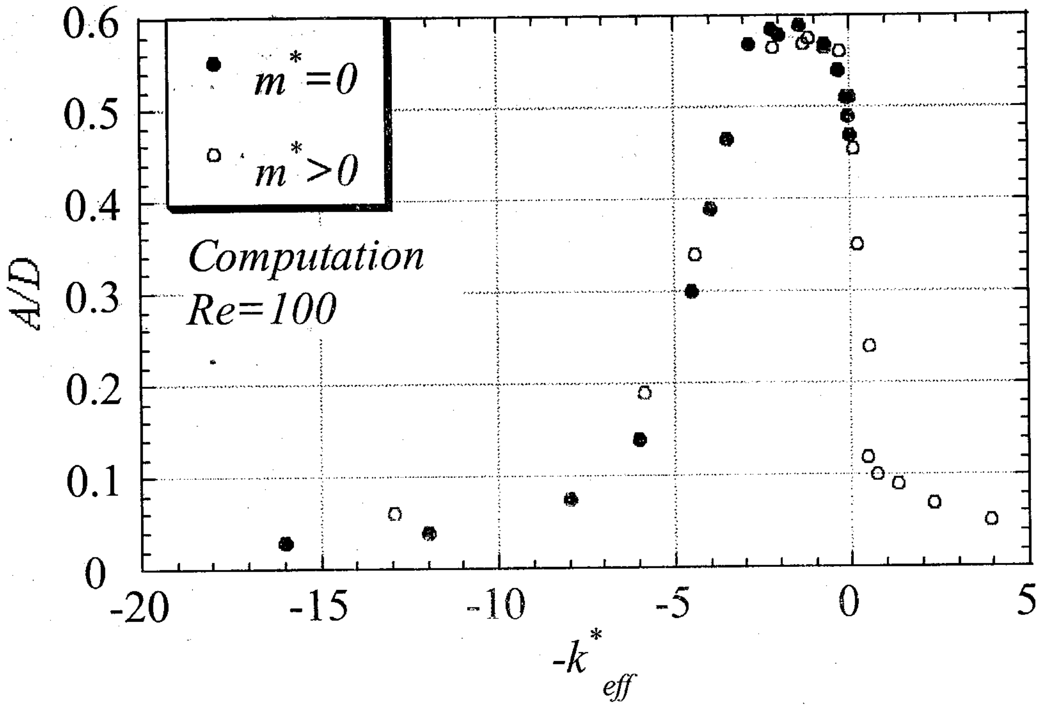

Figure 2.12 Universal curve for amplitude, *A/D*, vs. Effective stiffness, $-k^*_{eff}$, for $b^*=0$, *Re*=100 (Gharib et al. [1997] and Shiels [1998])

CHAPTER 3

Experimental Setup and Procedure

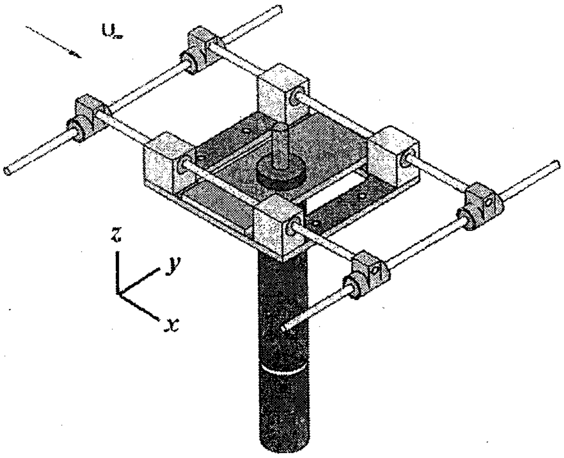

3. Experimental Setup and Procedure

3.1. General Description of the Experimental Setup

Figure 3.1 shows a general schematic of the experimental setup. A cylinder of diameter *D* and length *L* was supported vertically along *z* in a water tunnel with the free stream velocity U_∞ in the *x* direction. The cylinder was attached to a traverse free to move in cross-stream direction *y* as well as the stream-wise *x*. In one-dimensional cases (chapter 4), small clamps were used to confine the traverse to oscillate in *y* only. The entire setup rested on a platform that suppressed free surface waves.

The lower end of the cylinder was 0.25 inch away from the bottom wall within the boundary layer with no end plates. A laser LED, attached vertically to the traverse, transmitted the location of the cylinder to an optical setup that in turn mapped the above trace to a smaller area on a position-detector. The *x* and *y* trace signals created by the latter were amplified and finally saved in a Macintosh IIv computer. An *LDA* setup upstream recorded the mean free velocity U_∞, and a hot-film anemometer, downstream, detected the wake shedding frequencies within the shear layer. Two accelerometers connected to the traverse were used to record the acceleration in the *x* and *y* directions. The signals from all above probes were sampled using a 12 bit MacAudios data acquisition card and recorded and analyzed using Superscope data acquisition software. The data files were later converted and reanalyzed using Matlab computational software and signal processing toolbox. An analog frequency analyzer was also used to obtain long interval frequency assessments of the wake signals.

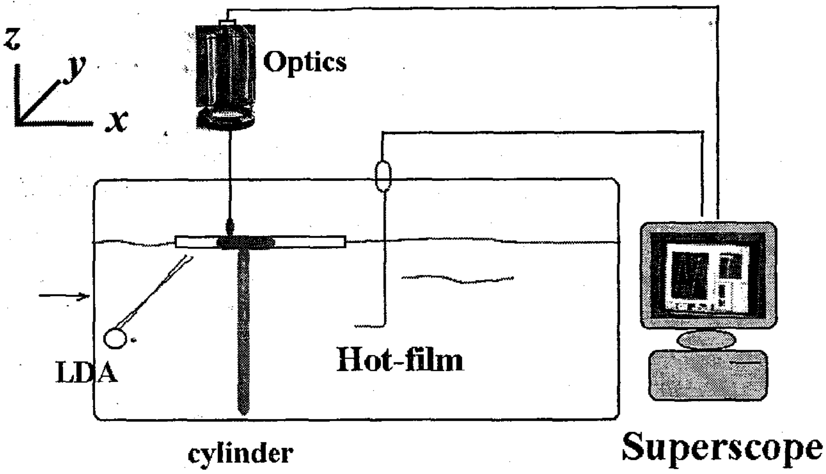

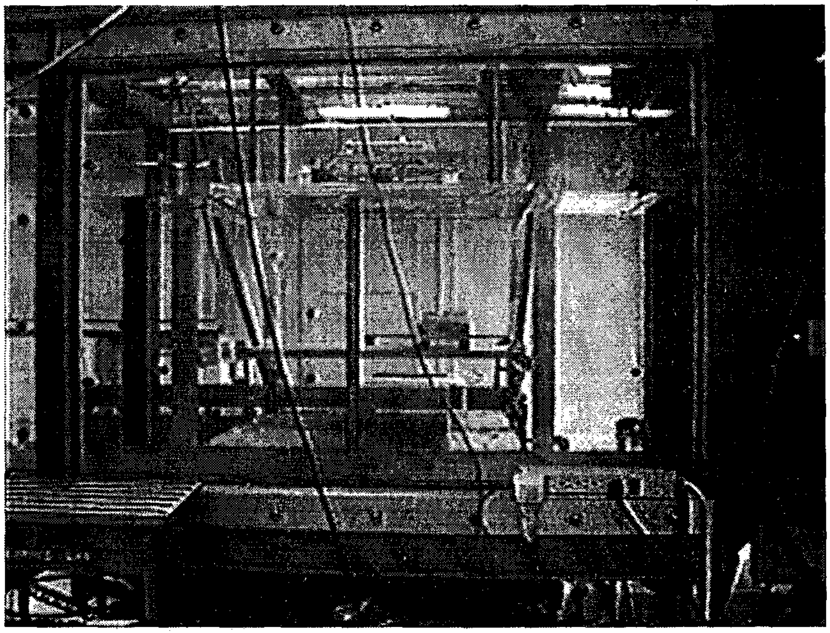

Figure 3.1 General overview of the setup

3.2. Water Tunnel

The experiments were conducted in the Free Surface Water Tunnel (FSWT) housed in the Hydrodynamics Laboratory at the Graduate Aeronautical Laboratories at the California Institute of Technology (GALCIT). The Free Surface Water Tunnel has a closed circuit circulation system lying in a vertical plane. The water stream passing through the working section is confined at the side walls and the bottom.

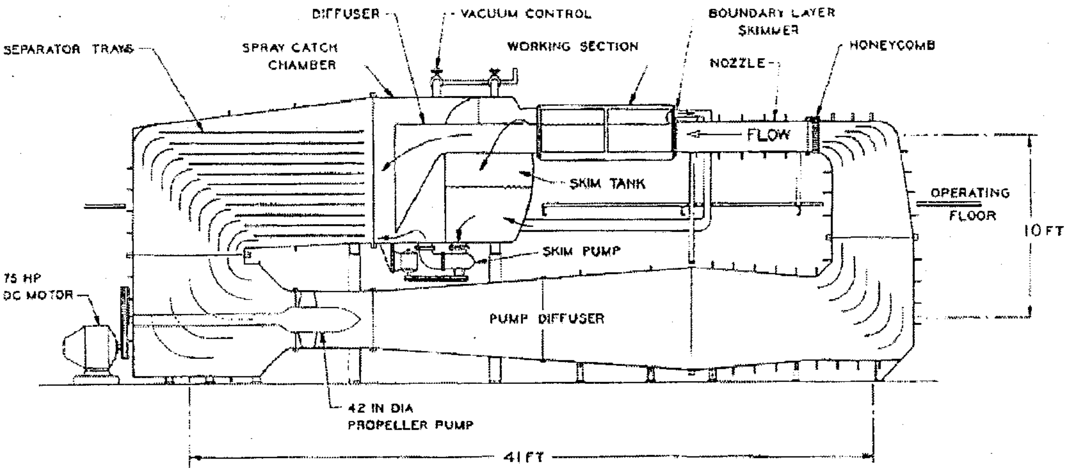

Figure 3.2 Schematic of the Free Surface Water Tunnel

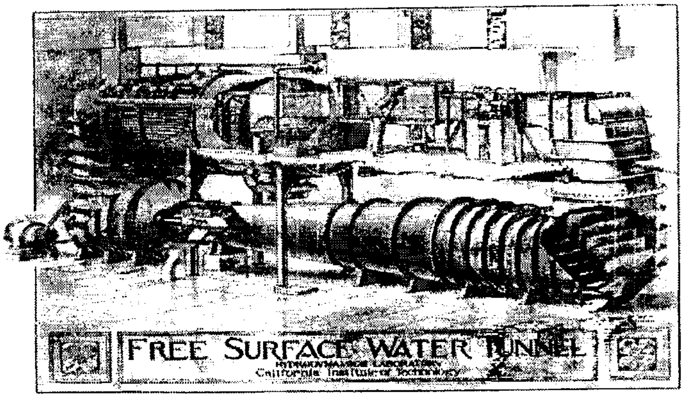

Figure 3.3 The closed circuit and the test section on the upper floor

The test section was 20 in. (508 mm) wide and 30 in. (762 mm) deep. The water depth was kept at 22.5 in. (572 mm) to provide an 8 in. (203 mm) air space above the free surface. The section was 8 ft (2. 44 m) in length and bounded on all sides by Plexiglas windows. Water velocity in the section could be regulated from zero to 25 ft/sec (7. 62 m/s). All experiments presented involved velocities below 120 cm/s.

3.3. Cylinder Models

A variety of cylinders were designed to accommodate different possible diameters and mass-ratios. All but one cylinder model were solid Plexiglas or metal rods. Diameters ranged from 0.25 to 2.1 inches. To accommodate the smallest mass ratio cases *R2* and *R3*, a hollow 0.1 inch thick Mylar tube of 2.1 inches diameter was used with plugged ends. Aluminum caps and a threaded rod running through this cylinder kept it steady and free of bending. All models had tapped ends such that they could be firmly attached flush with the traverse without any bending or vibration during the runs. All cylinder models were 22.25 inches long. The top end of each cylinder was attached to the main traverse 1.0 inch above the free surface. The actual length of the cylinders submerged in water was less than 21.25" due to the free surface deformations around the cylinder during the runs. The length L used in computing the mass ratios m^* was 22.25".

3.4. Traverse

The basic design of the traverse is shown in Figure 3.4. The small inner traverse is free to move in the y direction through two sets of bearings on rods attached to two sets of bearing moving along x. Since m_x, the portion of the traverse moving in x was part of m_y, the segment moving in y, m_x was less than m_y at all times (m_x =700 g, m_y =1310g). The cylinder models were attached to the center plate via bolts running through tapped holes in the center of each cylinder. The outer rods were held using brackets connected upon a stainless steel frame bolted down to a Plexiglas platform described below (Figure 3.4).

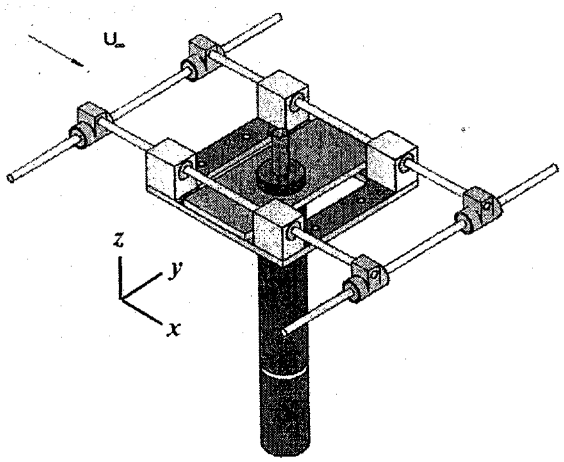

Figure 3.4 Traverse and the bearing setup

3.5. The Plexiglas Platform and the Tunnel Mounting

A rectangular Plexiglas platform of 18 inches width and 2 feet length was used to support brackets holding the outer rods of the traverse. The Plexiglas platform was 1.0 inch thick with a rectangular hole in the middle to accommodate an area for the cylinder to run through and oscillate. This platform was aligned using a level before every run. It did not reach the side walls of the tunnel and was supported using vertical threaded rods to the top of the tunnel. The spring holders were brackets that were attached to the platform in an adjustable manner.

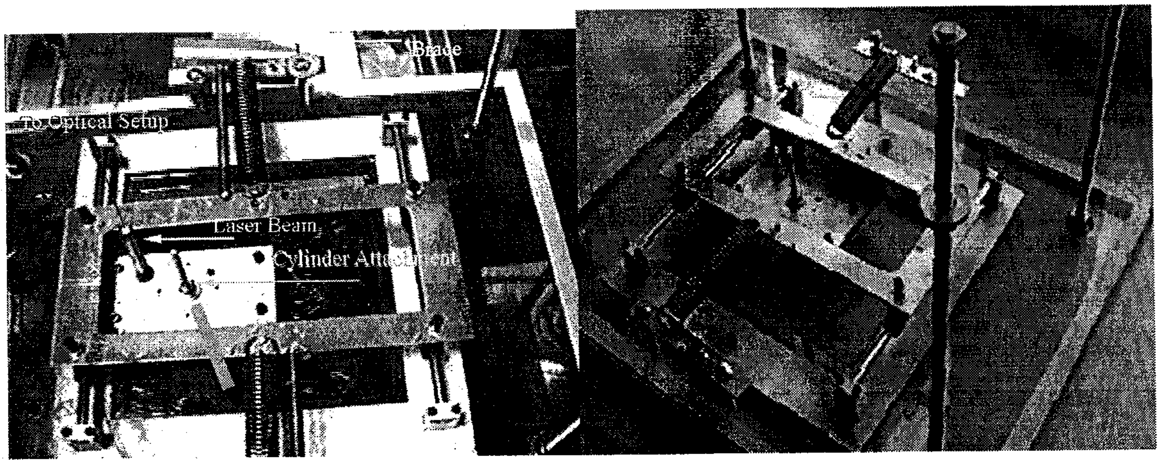

Figure 3.5 The traverse, the tunnel mounting, and the Plexiglas platform

The spring brackets were separately supported using tape *Wr*apped blocks of wood to fill the gap between them and the walls of the tunnel. This avoided any transfer of energy from the spring to the outside platform. Figure 3.5 shows the top and the side view of the tunnel mounting.

3.6. Springs

A variety of springs with different values of elastic stiffness from 0.3 to 50 lb/in were used. The springs were between 3.5 to 5.5 inches long and from 0.25 to 1.0 inch in diameter. Special attention was paid to ensure the maximum deflection for each to be within factory recommended linear range; however, small non-linearities were expected. A free decay vibration trace of the system was later used to study the nonlinearity of the springs along with other structural parameters such as friction.

3.7. Structural Damping and Non-Linearity

The damping parameter was minimized at all times to increase the possibility of vortex-induced vibration. No artificial damping was added in this study. The damping due to the springs proved to be non-linear to various degrees. The values reported with each case are based on linear theory. Section 6.10 describes a detailed account of the least-square fit techniques used to model an ordinary differential equation in a typical case.

3.8. Optical Setup

An optical instrument was designed to map oscillation amplitudes of up to 150 mm to an area of 8 mm on the position detector. Optimal conditions would have provided a bifocal system where images would be linearly proportional in size to the objects, that is, $A'B' = \alpha \times AB$. In addition, thin lenses would have also been desirable to avoid spherical aberration. This; however, would have called for a distance of about 2 yards between the two lenses rendering an optical setup on top of the water tunnel impossible. The problem was largely resolved by using thick lenses that would cancel the spherical aberration of one another and also by manipulating the distance between the two lenses such that the mapping would be as linear as possible in the predicted range of vibrations. In the first series of experiments with $m^*<10$, the oscillation amplitudes encountered were the largest and the optimal calibration curve naturally more non-linear (see Appendix A.2). This calibration served to map the location of the traverse to a voltage recorded from the optical position detector and hence included possible nonlinear effects due to the position detector. The small quadratic coefficients ($O(10^{-5})$) in the third order polynomials fitted to the calibration points showed an odd functional behavior as expected (A.2).

3.9. Accelerometers

Two low frequency Kistler accelerometers were used to record the acceleration of the traverse in x or y directions. The accelerometer outputs were 0.495 volts/g according to the factory calibration. These signals were needed to confirm values predicted from the force deduction technique (see chapter 6) and to ensure smooth cylinder motion. Any discrepancy between the displacement and the acceleration traces would reveal possible problems between the traverse and the cylinder such as cylinder bending; however, no such problems were encountered. The accelerometers were *Wr*apped in plastic covers and bound to the vertical surfaces of the traverse aligned in the x and y directions.

3.10. Hot-film and *LDA*

An *LDA* system upstream of the traverse was used to record U_∞ and a hot-film anemometer downstream to measure wake frequencies. With increasing flow speeds above 80cm/sec and growing oscillation amplitudes, U_∞ fluctuated (see Figure 3.6). An average value and a deviation were recorded for every tunnel speed.

3.11. Data Acquisition

A 12 bit MacAudios sampling card was used along with Superscope, a data acquisition software for Macintosh computers. The sampling card was capable of 128 kHz sampling through 12 separate channels. Sampling frequencies for this study were either 1 or 2 kHz. This range would allow an optimum resolution for the 12 bit signals, suitable file sizes and a sampling rate much larger than the oscillation frequencies predicted ([1-10 Hz]) for filtering purposes. Sampling intervals of 20 to 40 seconds were equivalent to a few hundred non-dimensional times (tU_∞/D) for each value of U_∞.

3.12. Experimental Procedure

The optical setup and the position detector were calibrated as one system before and after every set of experiments. Details of this procedure can be found in the Appendix A.2. The experiments were conducted in two subsequent *R* and *S* series. The *R* series concentrated on low mass ratio structures with $m^*<10$ and involved larger cylinder diameters and oscillation amplitudes. The *S* series was aimed at high mass ratios and involved smaller displacements and stronger springs. The latter required a different optical mapping and a larger more robust spring setup. As every case involved specific values of mass ratio, damping and Reynolds number, each was referred to by a letter followed by a number, where the letter describes the run series and the number refers to the specific case.

Case	m^*	$\zeta\times100$	m [kg]	k [lb/in]	f_n [Hz]	D [in]	$Re\ [10^3]$
R3	2	7.3	1.6	1.04	1.8	2.1	13-40

Prior to each case, the following procedure was followed: The platform, the laser beam and the traverse were checked for the horizontal/vertical alignment. The bearings were tested for friction and wetness. The accelerometers were checked for possible wetness. The traverse was positioned to move exactly along *x* and/or *y* according to the tunnel walls. The position of the optical setup and the position detector were tested for laser beam alignment.

The system parameters: mass, natural frequency and damping were recorded before or after each case. The mass of the structure was measured within one gram of accuracy. The cylinder was then replaced by a dense weight of equal mass and a free decay oscillation of the structure was recorded. The natural frequency of the trace and a first order approximation to the structural damping using linear theory was deduced. A higher approximation was later attempted using non-linear O.D.E. fits to every trace (section 6.10 for details). This first approximation was used to predict tunnel speeds allowing vortex-induced vibration.

The tunnel speed was kept below 120 cm/sec to ensure optimum steady flow field and great effort was made to obtain as many points as possible within the *VIV* window of U_∞. This, however, proved to be a challenging problem, for with increasing values of the mass ratio m^*, the tunnel speed ranges for *VIV* seemed to dwindle. In certain cases *VIV* would only occur at very specific values of U_∞ +/- 1cm/sec or less. This was particularly confounded by fluctuations in U_∞ and hence called for increased investigative effort.

A total number of 11 cases are presented in two series. The free stream velocity in every case was estimated using U~1 and ζ<<1 criterion, and a short investigative test was performed to find the range of possible free stream velocities U_∞ that would result in *VIV*. The main case would follow afterwards from the slowest tunnel speeds with small increments in order to obtain as many points as possible within the velocity range, given the accuracy of speeds obtainable in the tunnel. The system was given manual jolts outside resonant regions. This would explore the possibility of an oscillation mode requiring initial displacement and at the same time a record of structural decay at speeds just below the *VIV* range. Such decay traces may later be used to describe a mechanical model for the structure-in-shedding-fluid system. At speeds close to *VIV*, this would result in a few steady oscillations of small magnitude.

A period of about five to ten minutes was devoted to every data point to allow the tunnel to stabilize. The signals from the position detectors, the accelerometer, the hot-film anemometer and the *LDA* were samples simultaneously for 20 to 40 seconds with 952.8 or 2000 Hz sampling rates into the computer. The tunnel RPM, flow speed, approximate oscillation amplitude via a vernier caliper in the laser path, and the frequency through timing and counting 30 oscillations, and a brief description of the flow condition and the wake frequency according to the frequency analyzer was recorded by hand for redundancy.

3.13. Data Analysis

The process of data analysis was sensitive due to the quasi-periodic nature of the signals. Most cases showed evidence of non-linearity and time-dependent frequencies. This was mainly due to lack of a perfect synchronization between the shedding and the oscillation. Large interval and average sectional *FFT* routines proved to be useful for the steady traces and not so helpful for others. A simplified technique provided a more accurate time-averaged frequency by counting a large number of peaks (usually 30) and dividing the number by the time elapsed. This simple technique in some cases could detect a small steady growth in frequency with *U* that simple *FFT* could not. The other benefit of a manual frequency analysis was a focus on areas where a relatively steady oscillation was in fact occurring. Intermittency in such cases would severely affect mean amplitude and frequency. A blind *FFT* routine, on the other hand, would have the advantage of extracting information at small oscillation amplitudes that could fail to be included. This also would provide a more universal way to communicate the results with other researchers in the field.

The data was reduced in two manners, one using an *FFT* over the entire signal and another using the manual procedure above. To explore extra elements such as intermittency, noise, and time-dependent frequencies and amplitudes, selected points were analyzed using Empirical Mode Decomposition (*EMD*), a more sophisticated version of the manual peak counting procedure. *EMD* employs a sifting technique and along with the Hilbert transforms can produce time-dependent quasi-periodic modes within a given signal (see section 2.8).

The non-dimensional amplitude *A/D* and frequency, f/f_n, were plotted vs. *U* according to Feng and Parkinson [1968]. The data was also recast in the new k_{eff}^* format (see chapter 2) where *A/D* and $f^*=fD/U$ were plotted against $-k_{eff}^*$. The $-k_{eff}^*$ parameter increases with increasing *U*.

3.14. Discussion of Experimental Errors

Experimental error came from three possible sources. 1) Inherent inaccuracy due to variations in U_∞ during *VIV* caused by tunnel breathing and/or large oscillations affecting the *LDA* reading. 2) Inaccuracies in assigning frequency and amplitude values to a given trace due to quasi-periodicity or intermittency. 3) Error in amplitude values due to optical calibration or unsteady oscillations.

1) Figure 3.6 shows the standard deviation in recorded U_∞ as a function of U_∞ for case *R2* covering a wide range of velocities and amplitudes. The oscillation amplitude reached a high value of A=1.45 inches. This problem is usually due to tunnel breathing and confounded in this case by cylinder oscillations affecting the *LDA* reading.

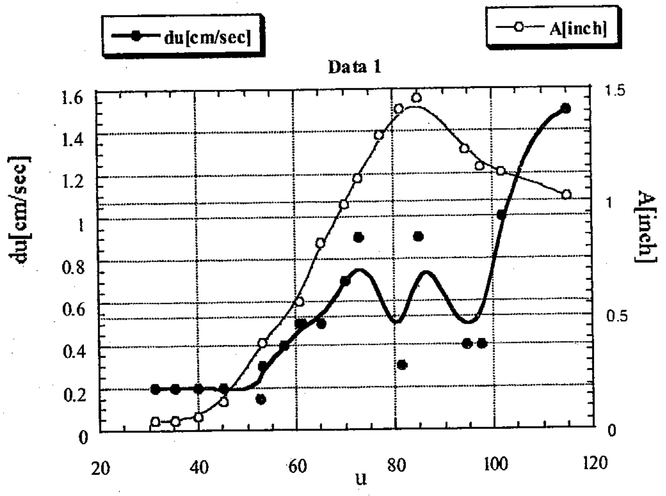

Figure 3.6 Tunnel speed variations and amplitudes vs. tunnel speed in case *R2*

In Figure 3.6, the large error around U_∞=80 cm/sec is due to the large oscillation amplitudes achieved and the larger deviation around U_∞=115 cm/sec is due to tunnel flow instability at such velocity. The *Reynolds* number at this point was about 6×10^5. Such tunnel variations are unavoidable and call for small amplitude-dependent error bars in U values reported. The variations in U_∞ in this case translate into small values in non-dimensional U ($dU<0.01$). The error bars hence are smaller than the size of the points used in reduced graphs and much less important than the variations in A/D and f/f_n values.

2) The second class of errors involves problems in assigning an average frequency to a given quasi-periodic trace. Detailed accounts of time-dependent frequencies in typical cases have been dealt with extensively and are referred to in section 4.11.

3) The optical calibration is discussed in detail in the Appendix A.2. The main issue was to safely capture the non-linearity in the optical mapping in the calibration. This non-linearity was important in cases that involved large diameter cylinders (*R3* and *R2* with D=1.5 inches) and only substantial at points with largest oscillation amplitude A/D.

CHAPTER 4

Experimental Results: One-Dimensional Oscillation

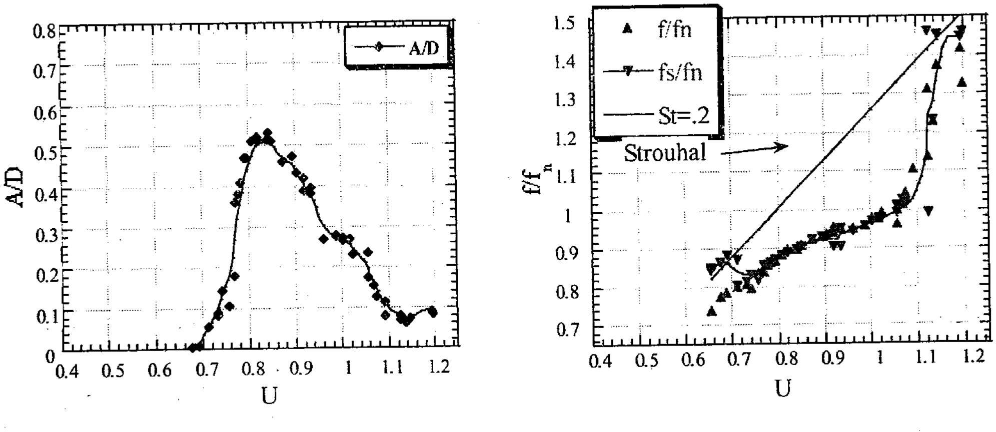

$m^*=9$

4. Experimental Results: One-Dimensional Oscillation

4.1. Introduction

The preliminary two-dimensional oscillation experiments with water-filled Plexiglas tubes showed a steady growth of oscillation and shedding frequencies with U but no signs of lock-in (Runs *O1* and *O2* in sections 5.5 and 5.6). A comparison of the experimental conditions to those of Feng's [1968] would most likely attribute the lack of lock-in to the small values of mass ratio and damping ($m^* = 1.7$, $\zeta = 0.004$) or the two-dimensionality of the oscillations in the new experiments. The following experiments were designed to achieve a wide range of mass ratios as well as one or two-dimensionality in order to study and isolate the effects of each element. As we shall see in this chapter, many 1D runs were encountered that exhibited no lock-in behavior. It was hence concluded that the number of degrees of freedom (1D vs. 2D motion) is not the reason behind the lock-in mystery and that variations in mass ratio m^*, however, play an important role.

In this chapter, the experimental results for the one-dimensional *VIV* cases are presented with increasing values of the mass ratio, m^*. The damping coefficient ζ is slightly different in different cases, however, the detailed behavior observed is quite different. For every case, a small number of representative displacement traces are presented along with their corresponding Fourier spectra (on log-log or linear scales). Since the non-dimensional time $\tau = \omega_n t$ is used to plot the traces, a period of $2\pi(f_n/f) \sim 2\pi$ corresponds to one complete oscillation. The y-axis range in all $y(\tau)/D$ traces is $-0.8 < A/D < 0.8$. The amplitude for each trace is based on an equivalent sine wave i.e. the root mean square of the signal portion (rms×√2) and the frequency is based on the *FFT* peak. For the traces that contained manual jolts, the frequencies and the amplitudes were computed within their steady segments only. When steady portions are too small, a transient interval was chosen instead for a qualitative presentation. Due to this freedom in selecting the portion of signal for amplitude and frequency analysis, there may be slight variations between values shown on a given trace and the reduced plots in a few cases. In reduced plots of amplitude and frequency, however, every trace was considered manually. The frequencies were obtained using a combination of *FFT* and peak counting and the amplitudes large oscillatory segments as explained above (see chapter 3).

The data sets are non-dimensionalized and reduced in two different ways: primarily, in the classical manner as used by Feng and Parkinson (A/D and f/f_n vs. U) and subsequently, according to the new effective stiffness (A/D and f^* vs. $-k^*_{eff}$) discussed in chapter 2. The latter uses flow parameters U_∞ and D to non-dimensionalize other parameters and is valid at vanishing values of structural parameters. The minus sign in $-k^*_{eff}$ is so that $-k^*_{eff}$ increases with increasing U. Details of these formulations and the data reduction procedure can be found in chapters 2 and 3. Values of A/D and f/f_n vs. U are plotted using the same scales as much as possible. Table 4.1 shows the cases considered and their corresponding structural parameters ordered in increasing values of mass ratio.

Case	m^*	$\zeta\times100$	m [kg]	k [lb/in]	f_n [Hz]	D [in]	*Re [10^3]*
R3	2.1	7.3	1.6	1.04	1.8	2.1	13-40
R6	5.1	3.5	2.07	3.2	2.7	1.5	13-26
R10	8.9	2.7	1.6	7.4	4	1	11.5-19.5
S7	9	2.1	1.6	11.5	5	1	13-24
R5	9	3.7	1.6	4.2	3.3	1	9-13
S6	27.0	2.7	4.9	30	5.8	1	17-24
S1	28.0	0.7	5.03	30	5.7	1	10-25
S5	39.0	2.9	7.13	30	4.7	1	14-21
S2	72.0	2.1	5.06	94	8.8	0.62	11-13.6

Table 4.1 List of cases considered with increasing mass ratio

Figure 4.1 and Figure 4.2 show the large scale and the small scale behavior of a typical large displacement trace, $y(t)/D$, at (case *S1*, U=0.96, $-k^*_{eff}$=0.45). Figure 4.2 also shows a sine wave for comparison. The amplitude of the sine wave is computed using the standard deviation of the original signal multiplied by √2 and the frequency is obtained through peak counting.

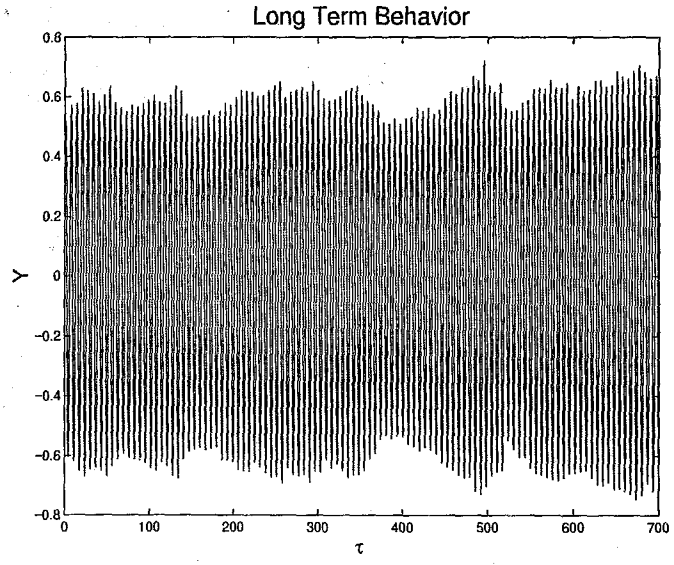

Figure 4.1 Displacement trace *y(t)/D*, Long term behavior, U=0.96, *S1*, m^*=28

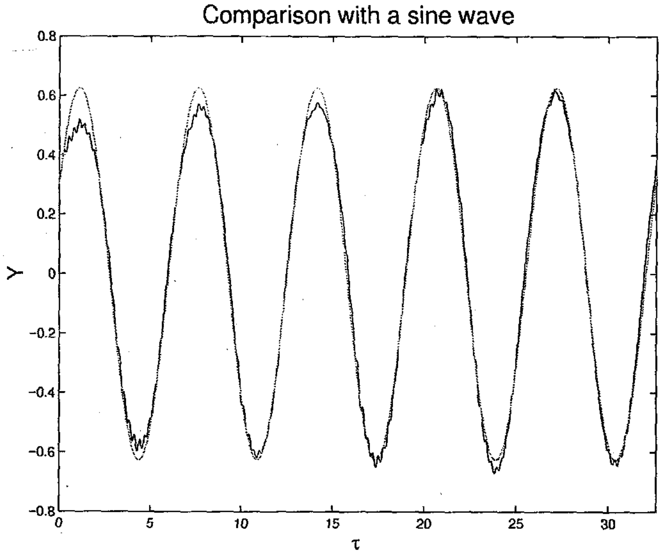

Figure 4.2 *y(t)/D*, Comparison with a pure sine wave, U=0.96, *S1*, m^*=28

4.2. *R3*: One-dimensional Oscillation with a Mass Ratio of 2.1

Case	m^*	$\zeta\times100$	m [kg]	k [lb/in]	f_n [Hz]	D [in]	*Re [10³]*
R3	2.1	7.3	1.6	1.04	1.8	2.1	13-40

R3 was the lowest mass-ratio case studied. Its structural parameters are listed above. This small mass ratio was achieved using a large hollow Mylar tube with a mass of 320 grams. The rest of the mass was due to the part of the traverse moving along *y*. The oscillations occurred over a large range of free stream velocities with $13\times10^3<Re<40\times10^3$.

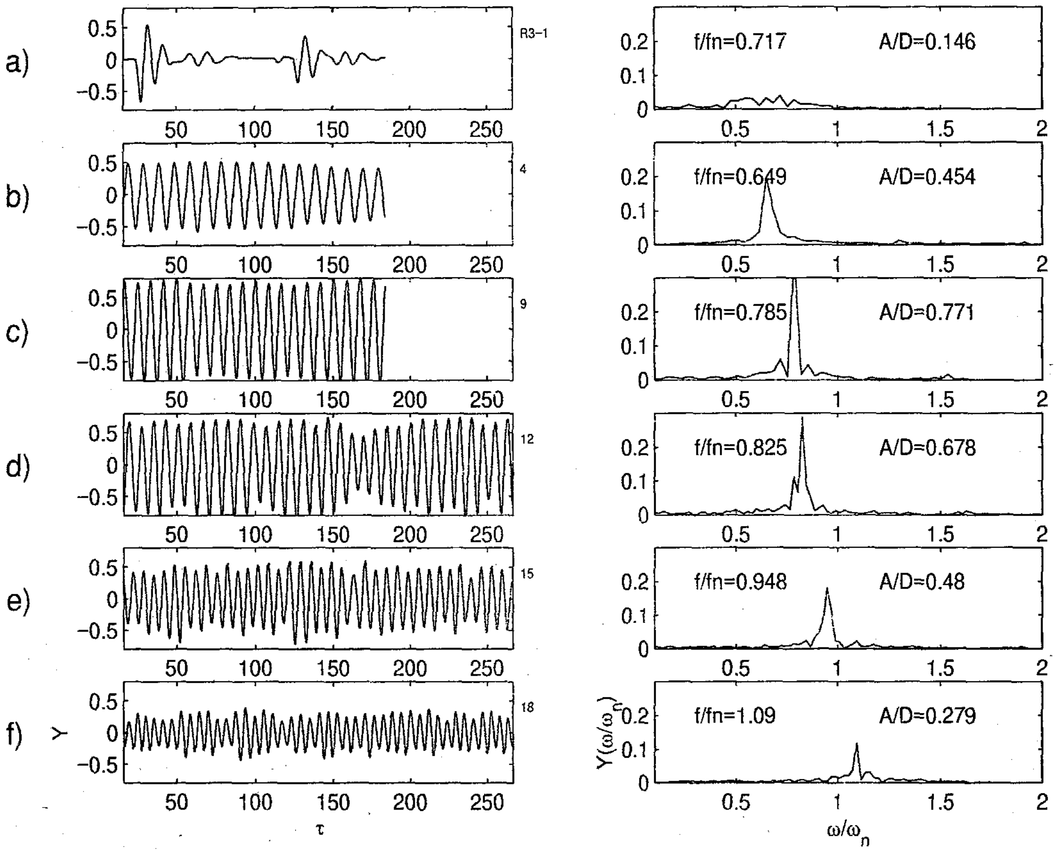

Figure 4.3 Oscillation traces and frequency spectra for case *R3*, m^*=2.1, at a) U=0.41, b) U=0.53, c) U=0.69, d) U=0.84, e) U=0.98, f) U=1.12

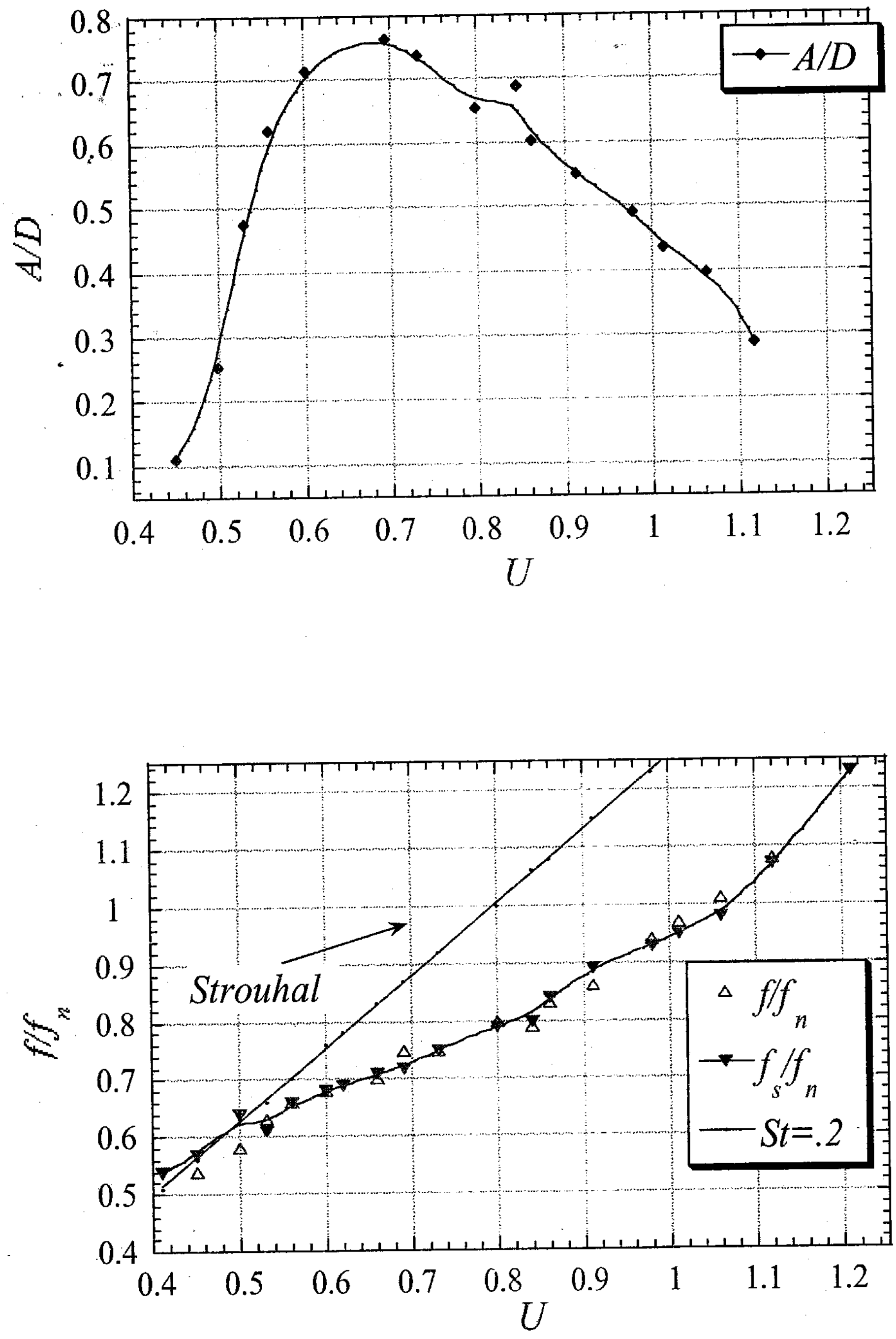

Figure 4.4 Oscillation amplitude and frequency response vs. *U*, *R3*, m^*=2.1

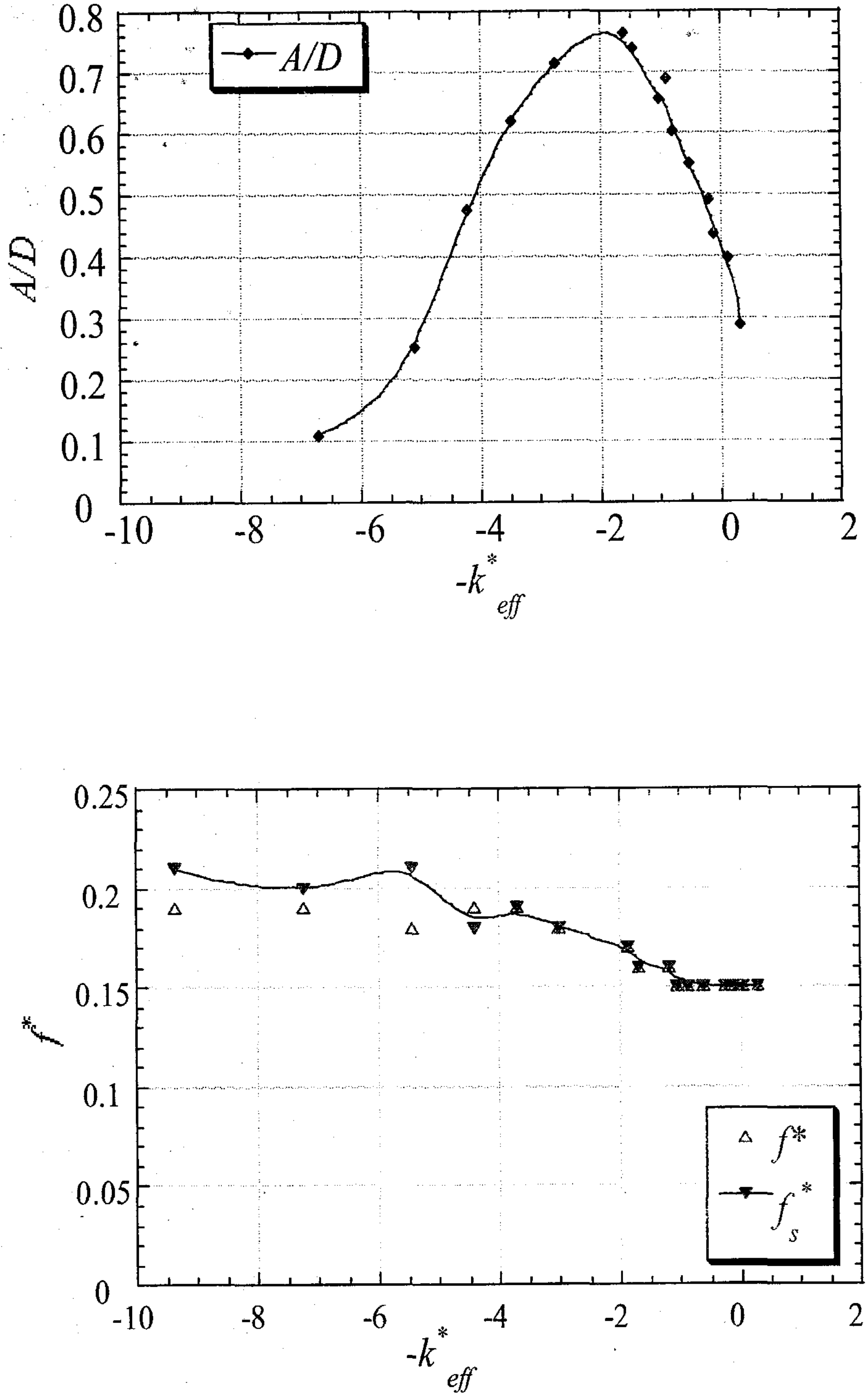

Figure 4.5 Oscillation amplitude and frequency vs. -k^*_{eff}, *R3*, m^*=2.1

Both the oscillation and the shedding frequencies here show a steady increase with the free stream velocity U (Figure 4.3 and Figure 4.4). The amplitude of oscillation reaches a value of 0.77 at U=0.62. This amplitude is close to 0.75, usually predicted for the zero limits of mass and damping. The nominal Strouhal shedding frequency with St=0.21 is shown as a tilted line for reference. Although the frequency response certainly deviates from the nominal shedding, there are no signs of lock-in evident. The general shape of the A/D curve does not indicate any humps as reported by Khalakh & Williamson [1997].

Figure 4.5 shows the reduced values of A/D, f^*, and f_s^* as a function of the new $-k^*_{eff}$ parameter. As discussed in chapter 2, this parameter is the universal parameter for single frequency VIV at given values of damping, b^* and Re. The damping parameter $b^*=2m^*\zeta/U$ and Re, however, do not remain constant in any of the cases presented and in fact, b^* in $R3$ declines with increasing U from 0.68 to 0.24 and Re increases linearly from 13,000 to 40,000.

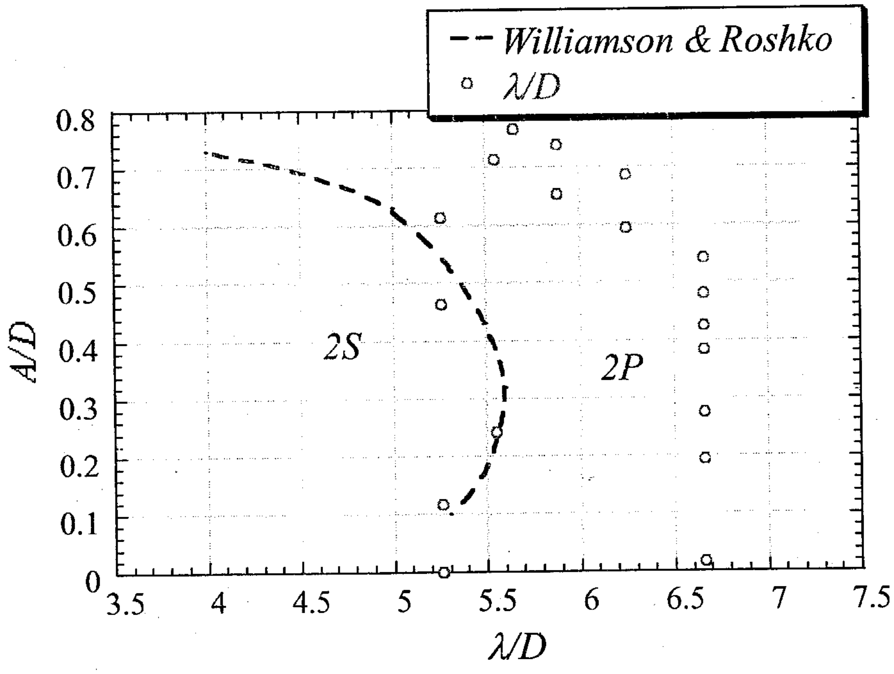

Figure 4.6 *R3*, m^*=2.1, on the Williamson-Roshko plane

Figure 4.6 shows the data points on the Williamson-Roshko plane with the dashed curved line indicating the boundary between *2S* and *2P* shedding regimes. The parameter λ/D is the stream-wise length traveled by the fluid in one complete oscillation and is simply equivalent to $1/f^*$ in the present experiments. Values of λ/D increase with U and are mostly on the *2P* side. No particular "jump" in amplitude and hence the fluid force is observed as this boundary is crossed ($k^*_{eff} \times A/D = C_y$). Figure 2.11 in chapter 2 can be referred to for comparison with results of Brika and Laneville [1994].

4.3. *R6*: Mass Ratio of 5.1

Case	m^*	$\zeta \times 100$	*m* [kg]	*k* [lb/in]	f_n [Hz]	*D* [in]	*Re* [10^3]
R6	5.1	3.5	2.07	3.3	2.7	1.5	13-26

The amplitude for case *R6*, Figure 4.7, grows gradually with increasing U to a maximum of A/D=0.56 at U=0.84. The frequencies show steady growth with U. The shedding and oscillation frequencies are almost indistinguishable at large oscillation amplitudes.

Reduced plots of amplitude and frequency in Figure 4.8 resemble those obtained for *R3* (m^*=2.1) except for the narrower range of U and k^*_{eff} and smaller values of A/D. The general shape of the A/D vs. U curve is smooth for $0.8<U<1.0$. The drop in amplitude at $U>1.0$ is relatively steep. There is no evidence of lock-in.

Figure 4.9 shows the reduced values of A/D, f^*, and f_s^* as a function of $-k^*_{eff}$. Damping, b^*, in *R6* declines with increasing U from 0.68 to 0.44, and *Re* increases linearly from 13,000 to 26,000. Figure 4.10 shows the results on the Williamson-Roshko plane. The λ/D values increase with U and seem mostly to be on the *2P* side.

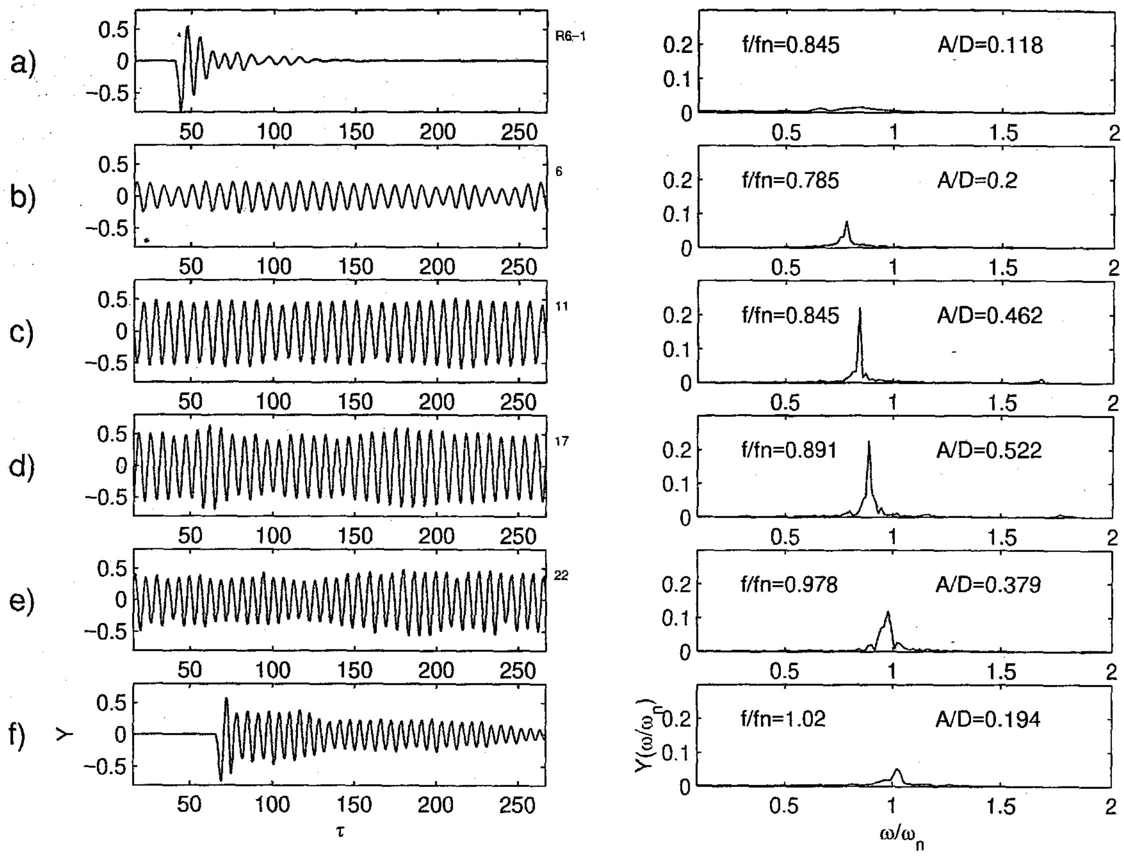

Figure 4.7 Oscillation traces and frequency spectra for *R6*, m^*=5.1 at a) U=0.54, b) U=0.69, c) U=0.78, d) U=0.90, e) U=1.01, f) U=1.06

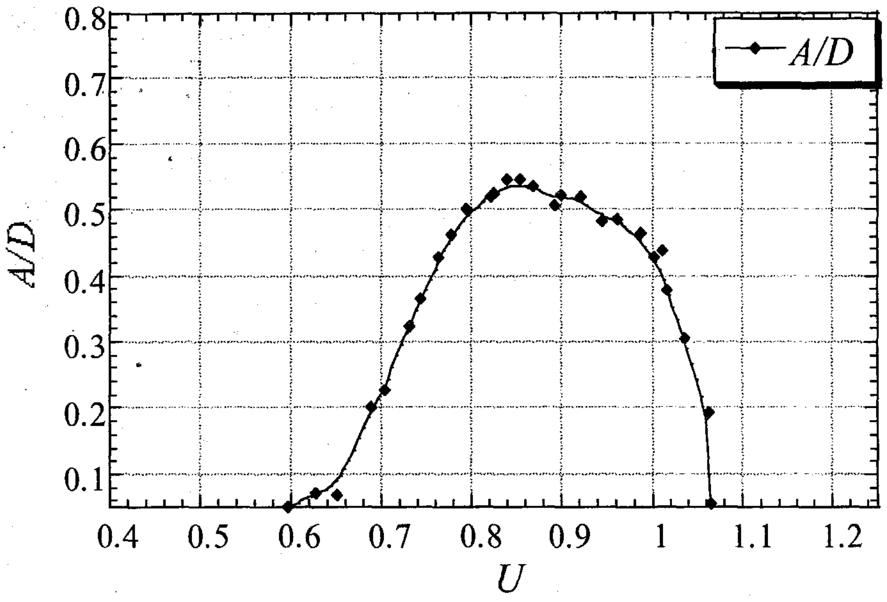

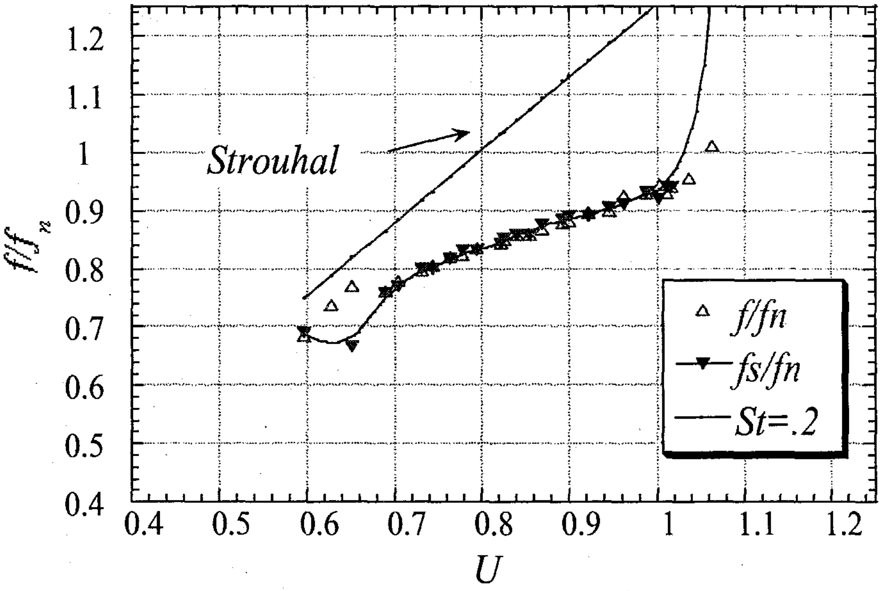

Figure 4.8 Oscillation amplitude and frequencies vs. *U* for *R6*, m^*=5.1

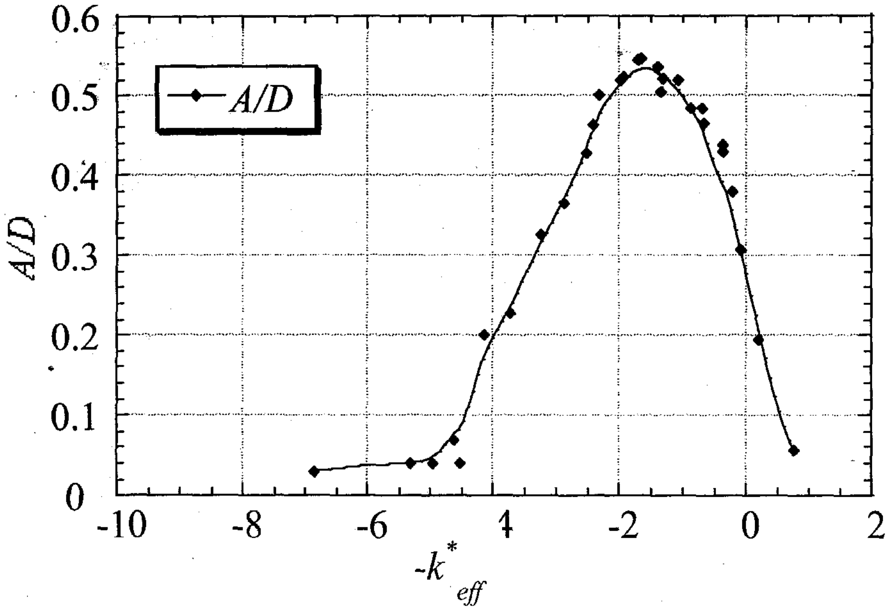

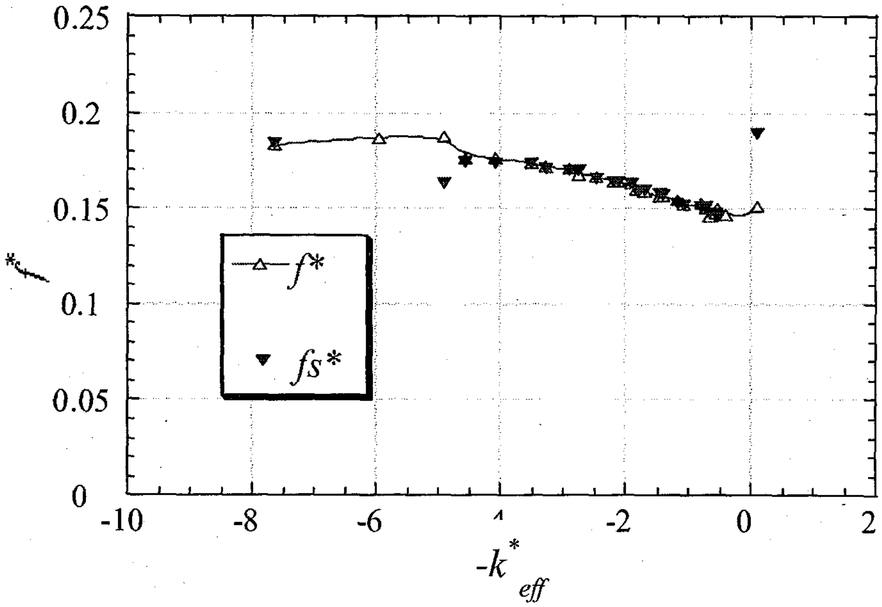

Figure 4.9 Oscillation amplitude and frequency vs. $-k^*_{eff}$ for *R6*, $m^*=5.1$

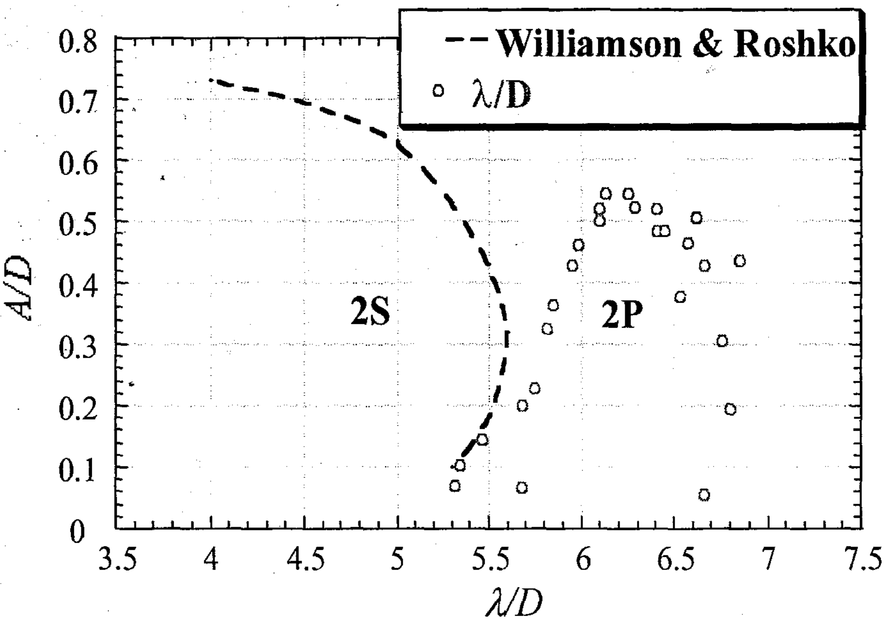

Figure 4.10 *R6*, m^*=5.1, on the Williamson-Roshko plane

4.4. *R10*: Mass Ratio of 8.9

Case	m^*	ζ×100	*m* [kg]	*k* [lb/in]	f_n [Hz]	*D* [in]	*Re* [10^3]
R10	8.9	2.7	1.6	7.4	4	1	11.5-19.5

R10 involved a Reynolds number range of 11,500<*Re*<19,500, overlapping that of *S7*. The damping, ζ=0.027, is very close to ζ=0.021 from *S7* and the *VIV* behavior is similar. The oscillations start slowly at *U*=0.8 and build up to *A/D*=0.46 at *U*=0.99. The peak amplitude is only 0.06 diameters below that of *S7* and with minimal intermittent behavior. *U* varies between *U*=0.72 to *U*=1.23. The amplitudes slowly decrease above *U*=1.0 and finally quickly decay beyond *U*=1.06. The frequency response does not indicate any signs of lock-in and continues to grow with *U* monotonically.

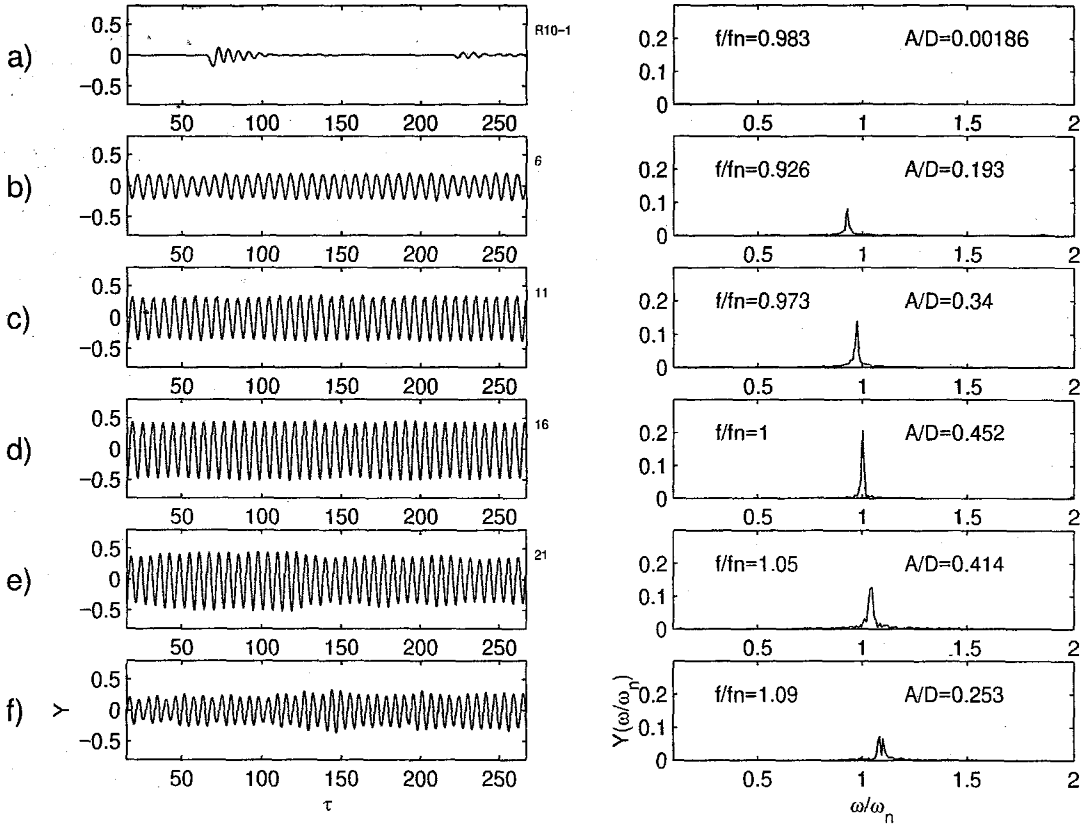

Figure 4.11 Oscillation traces and frequency spectra for *R10*, m^*=8.9 at a) *U*=0.72, b) *U*=0.84, c) *U*=0.88, d) *U*=0.93, e) *U*=1.04, f) *U*=1.09

Figure 4.12 shows a steady increase in shedding and oscillation frequencies. Here f/f_n results are shown using both *FFT* and peak counting to indicate minute differences. The overall shape of the amplitude response shows possible hints of transition around *U*=1.11. Figure 4.13 shows a narrow range of $-k^*_{eff}$ with the possible branching above. The frequency f^* reaches a minimum value of 0.153 at *A/D*=0.26, past the peak amplitude. The damping, b^*, ranges from 0.94 to 0.54 with increasing $-k^*_{eff}$.

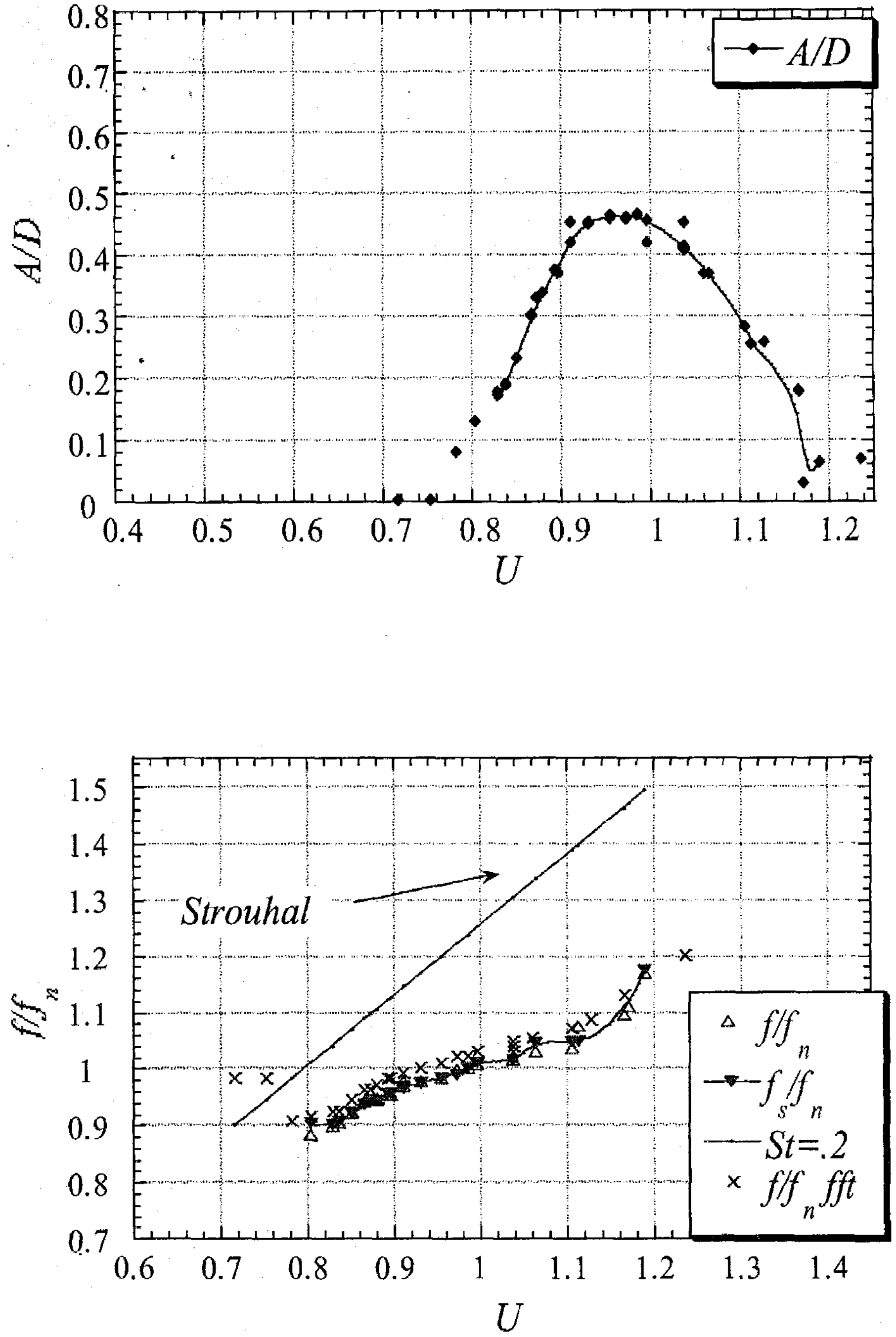

Figure 4.12 Oscillation amplitude and frequency response vs. U for $R10$, m^*=8.9

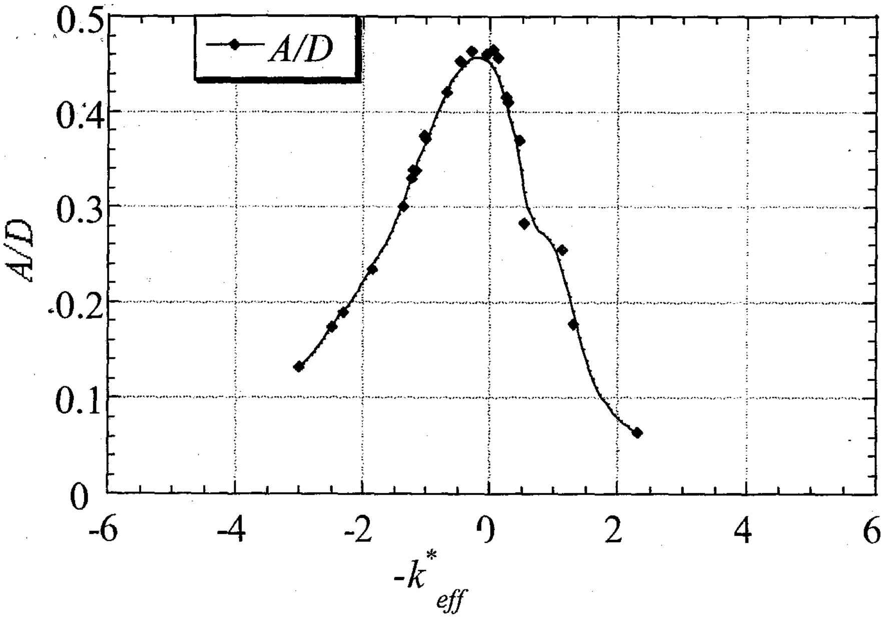

Figure 4.13 Oscillation amplitude and frequency vs. $-k^*_{eff}$ for *R10, m^**=8.9

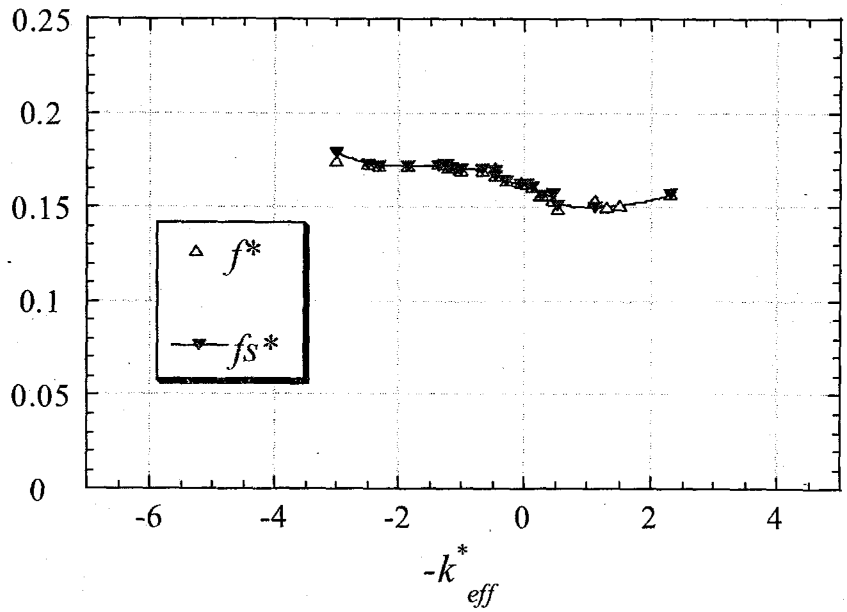

Figure 4.14 Frequency f^* vs. $-k^*_{eff}$, details, *R10, m^**=8.9

4.5. *S7*: Mass Ratio of 9

Case	m^*	$\zeta \times 100$	m [kg]	k [lb/in]	f_n [Hz]	D [in]	*Re [10^3]*
S7	9	2.1	1.6	11.5	5	1	13-24

The steady frequency increase with U in this case is evident in Figure 4.15. For U<0.77, displacements are small with mixed frequency contents, that is f_s and f co-exist or appear at alternate times. At U=0.77, the amplitude suddenly doubles and the oscillations become more steady. The large amplitude of oscillation gives rise to fluctuations in the values of U as detected by the *LDA* system by as much as U'=0.005. The two frequencies f and f_s continue to co-exist, although with minute differences. Figure 4.16 shows the large gap between the two frequencies for U<0.77.

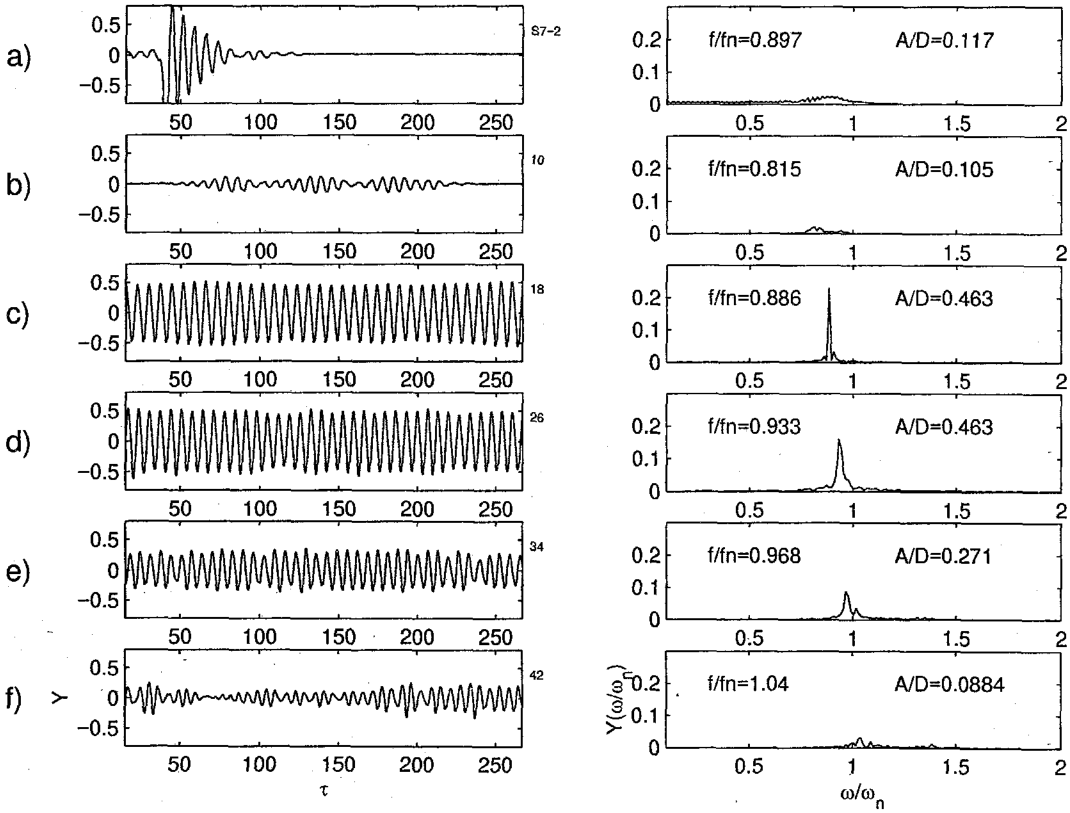

Figure 4.15 Oscillation traces and frequency spectra for *S7*, m^*=9 at a) U=0.65, b) U=0.73, c) U=0.80, d) U=0.89, e) U=1.00, f) U=1.07

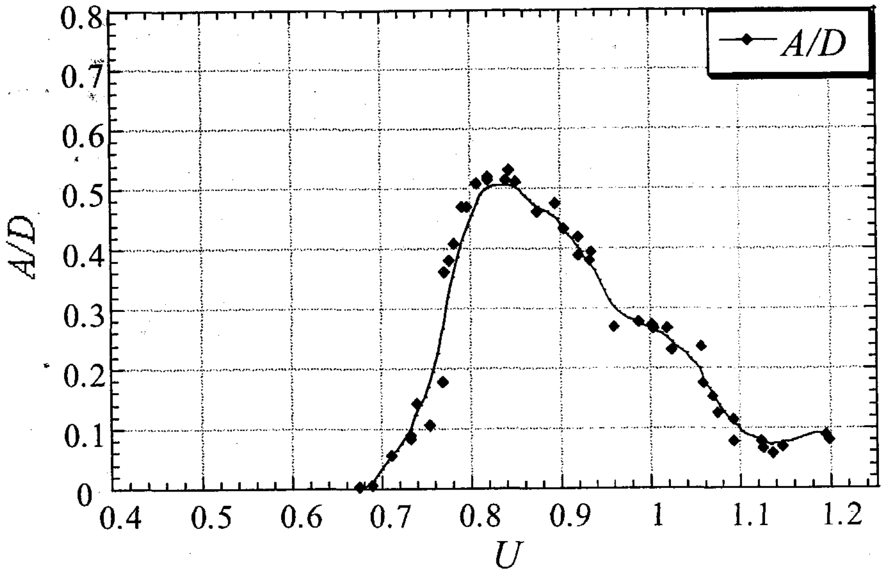

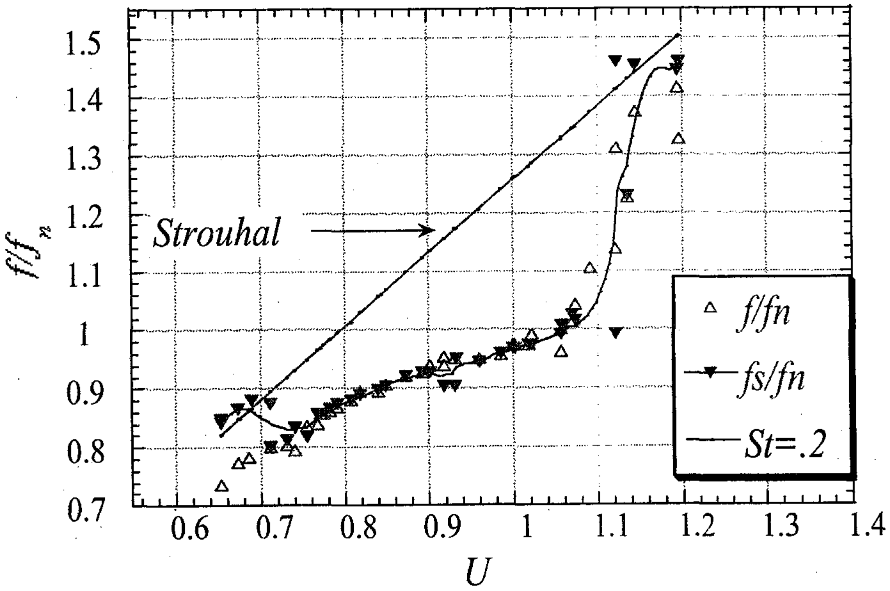

Figure 4.16 Oscillation amplitude and frequency response vs. *U* for *S7*, m^*=9

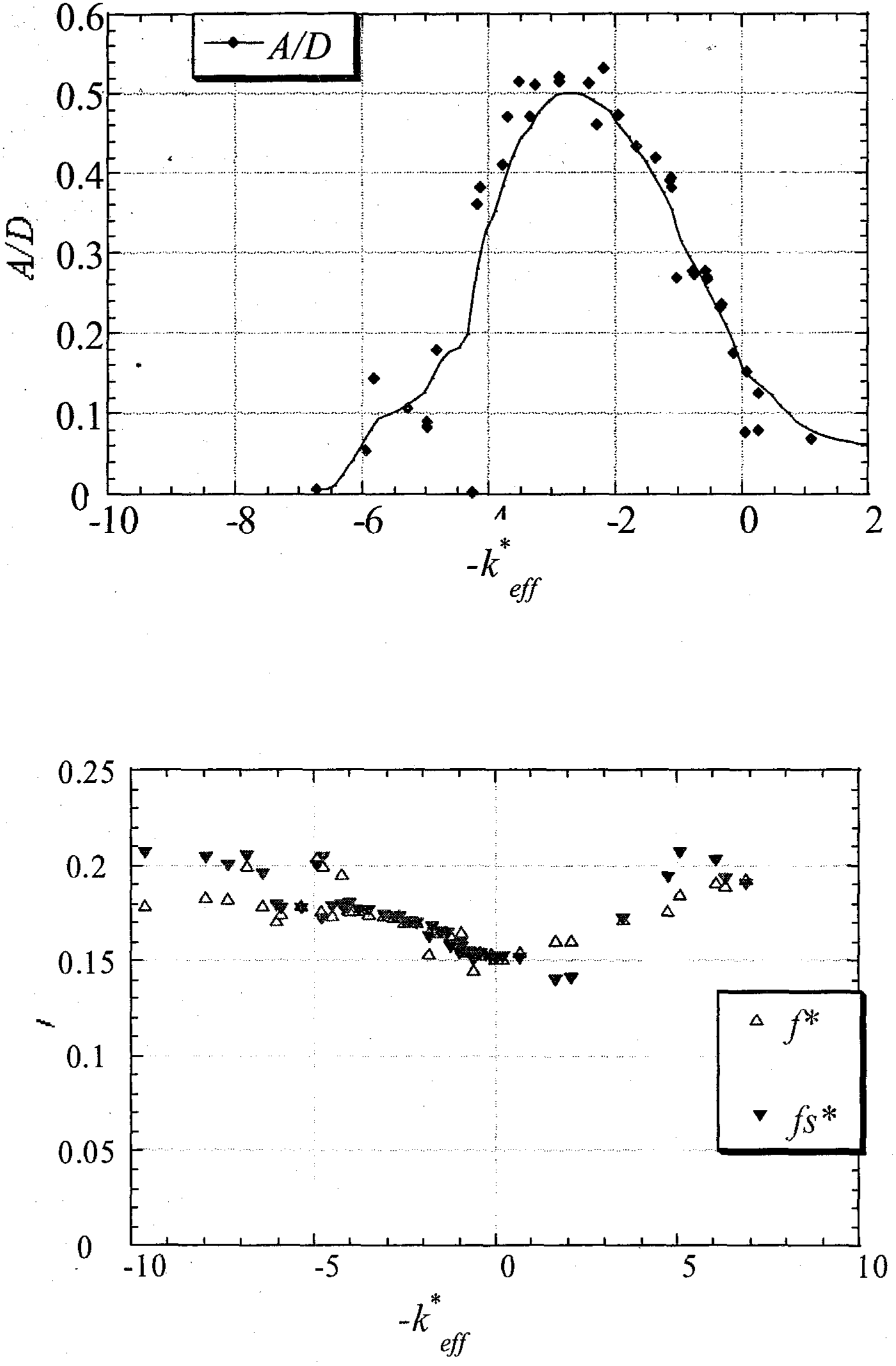

Figure 4.17 Oscillation amplitude and frequency vs. $-k^*_{eff}$, for *S7*, $m^*=9$

Figure 4.16 also shows a hump in the *A/D* curve about $0.96<U<1.05$. The amplitude falls from a value of $A/D=0.39$ to 0.27 and does not change much until another drop at $U=1.06$

from A/D=0.24 to A/D 0.18. The frequency plot of f/f_n does not reflect any particular change at this value. The oscillations become unsteady with a richer frequency content similar to the U<0.77 range.

Figure 4.17 shows the amplitude and the frequency behavior for this case as a function of $-k^*_{eff}$. The damping b^* ranges from 0.68 to 0.36 with increasing U or $-k^*_{eff}$. The frequency f^* is lowered from the usual value of St=0.21 to a minimum value of f^*=0.145 at $-k^*_{eff}$=-0.60 and A/D=0.24 near the hump mentioned above. It is noteworthy that this maximum deviation does not occur at the largest amplitude. A comparison with the Williamson & Roshko plane proves most points to be in the so-called *2P* region.

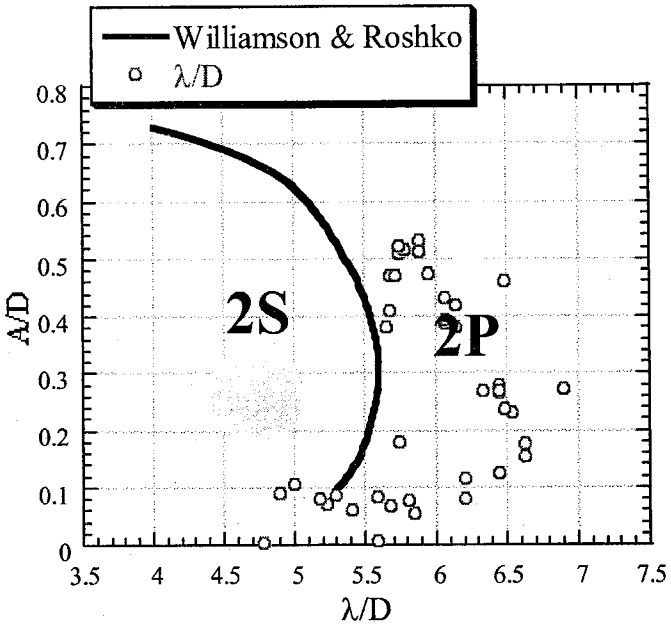

Figure 4.18 ***S7*, m^*=9, on the Williamson-Roshko plane**

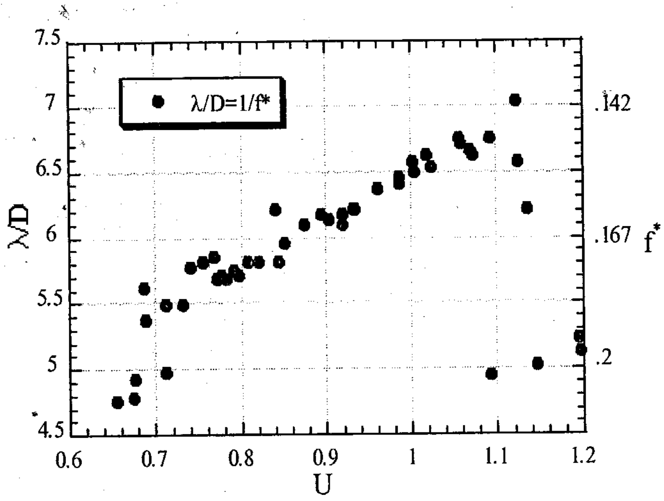

Figure 4.19 The growth in λ/D with increasing U, $S7$, $m^*=9$

4.6. R5: Mass Ratio of 9

Case	m^*	$\zeta\times100$	m [kg]	k [lb/in]	f_n [Hz]	D [in]	Re $[10^3]$
R5	9	3.7	1.6	4.2	3.3	1	9-13

Although this case involved the same mass ratio as the previous case with more damping, it shows a different behavior. The lower natural frequency called for a lower Reynolds number range of $9{,}000<Re<13{,}000$ just below that of *S7*. The oscillations were unsteady and would often decay after many cycles. The substantial difference between *S7* and *R5* is remarkable. The values of A/D and f/f_n in Figure 4.20 are based on the trace segments indicated and the frequency spectrum is in log-log scale to magnify the small power magnitudes and frequency changes.

Due to the unsteady behavior of *R5*, Figure 4.21 reflects values of frequency and amplitude obtained from both the large and small amplitude portions of each trace to represent the existing variation. At very small amplitudes, the nominal Strouhal frequency is detected as expected. The frequency growth seems to be more steady in the *FFT* results.

The large variation in frequency makes k^*_{eff} vary by large amounts and hence plots using this parameter are unintelligible. This is mainly due to the fact that the k^*_{eff} parameter was derived for a single frequency oscillation only. The damping parameter b^* here varies from 0.44 to 0.30. The frequency tends to increase with no signs of lock-in. The unsteady behavior of this case precludes an objective shape study of the amplitude curve. The range of oscillations is more limited here with $0.7<U<1.05$.

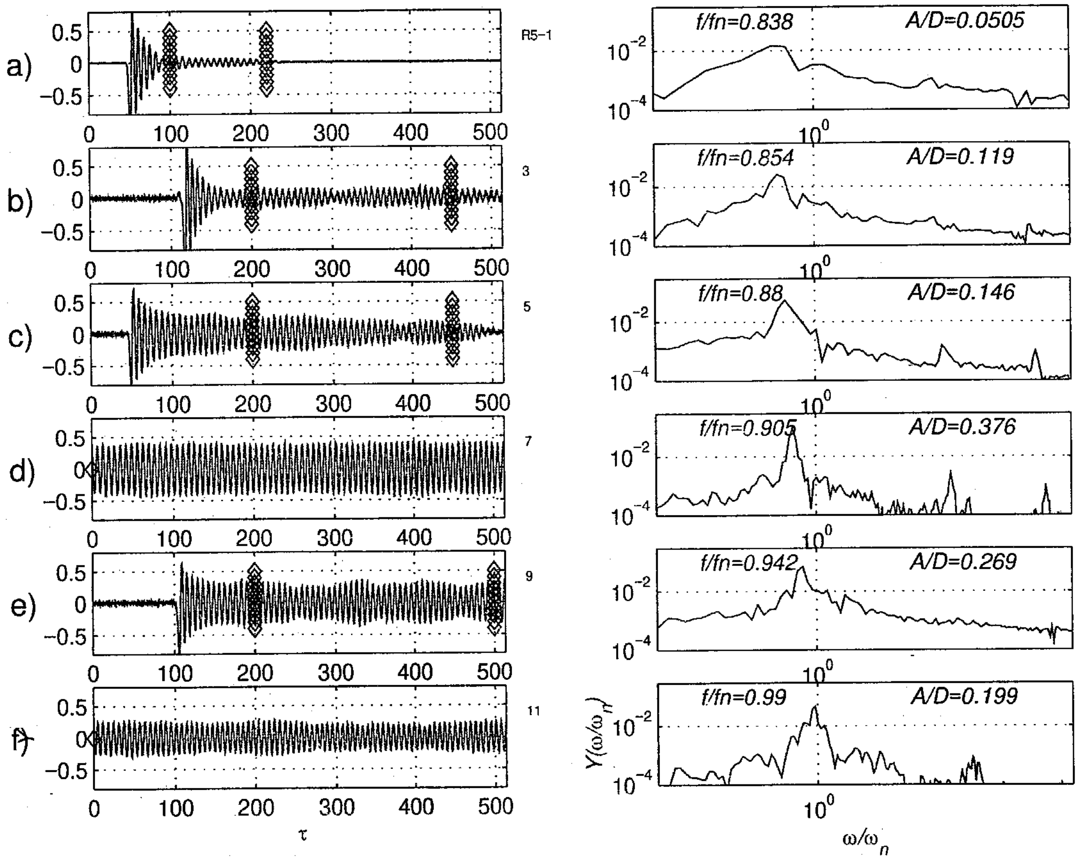

Figure 4.20 Oscillation traces and frequency spectra for *R5*, m^*=9, at a) *U*=0.68, b) *U*=0.73, c) *U*=0.80, d) *U*=0.84, e) *U*=0.91, f) *U*=0.99

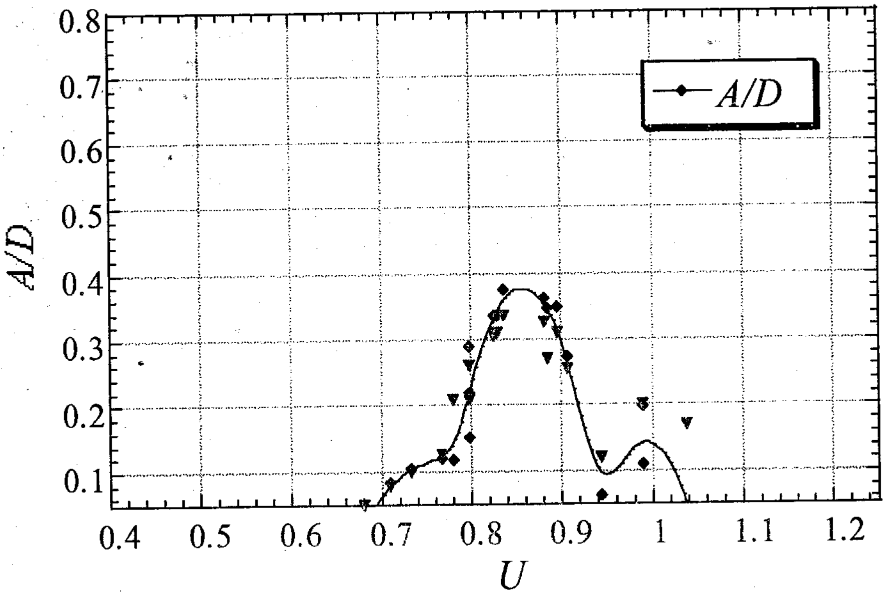

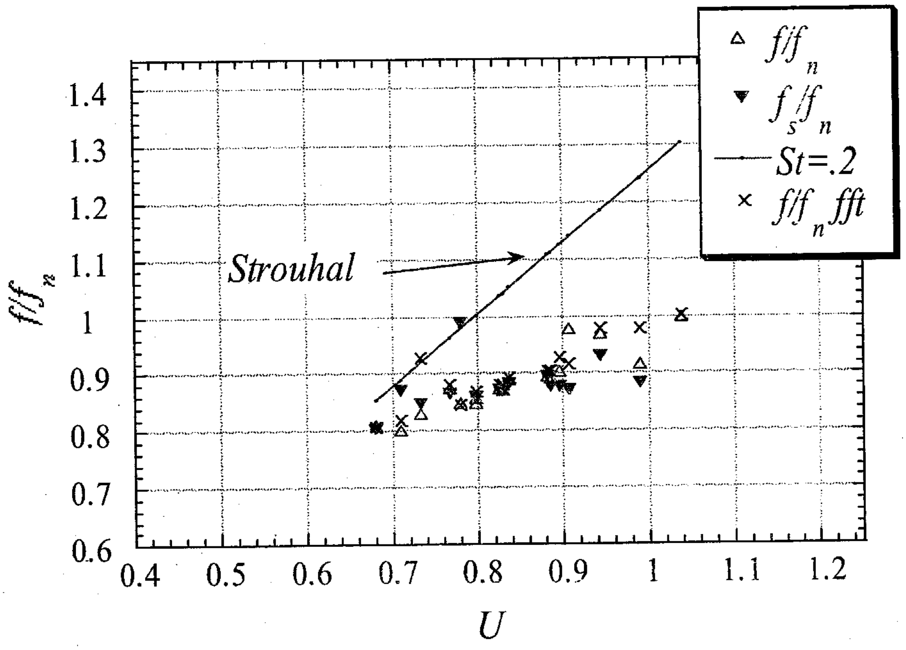

Figure 4.21 Oscillation amplitude and frequency response vs. *U* for *R5*, m^*=9

4.7. ***S1*: Mass Ratio of 28**

Case	m^*	$\zeta\times100$	m [kg]	k [lb/in]	f_n [Hz]	D [in]	*Re [10^3]*
S1	28.0	0.7	5.03	30	5.7	1	10-25

Despite the relatively large mass ratio, *S1* shows a steady growth in amplitude response with small disruption. The usual competition between the shedding and oscillation frequencies is detected at small values of *U* where the amplitudes are small; however, this does not cause visible disruptions in the oscillation as it did in *R5*. The amplitudes grow slowly to a value of A/D=0.11 at U=0.86 and through a sudden leap, a value of A/D=0.57 is reached without any sudden shift in the frequency response. Although this leap falls within the *2P* regime on the Williamson-Roshko plane (Figure 4.28), a sudden wake/phase transition is the most probable cause for the change ($C_y=A^*\ k^*_{eff}$ and k^*_{eff} stable). For $0.88<U<1.02$, the amplitudes decrease slowly with a sudden plunge at U=1.08.

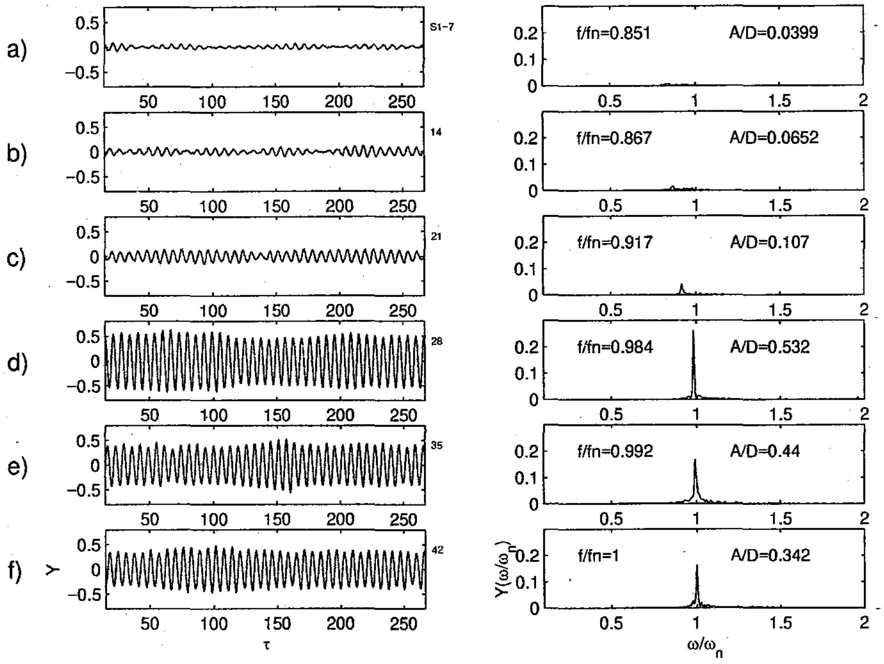

Figure 4.22 Oscillation traces and frequency spectra for *S1*, m^*=28, at a) U=0.72, b) U=0.77, c) U=0.86, d) U=0.96, e) U=1.02, f) U=1.06

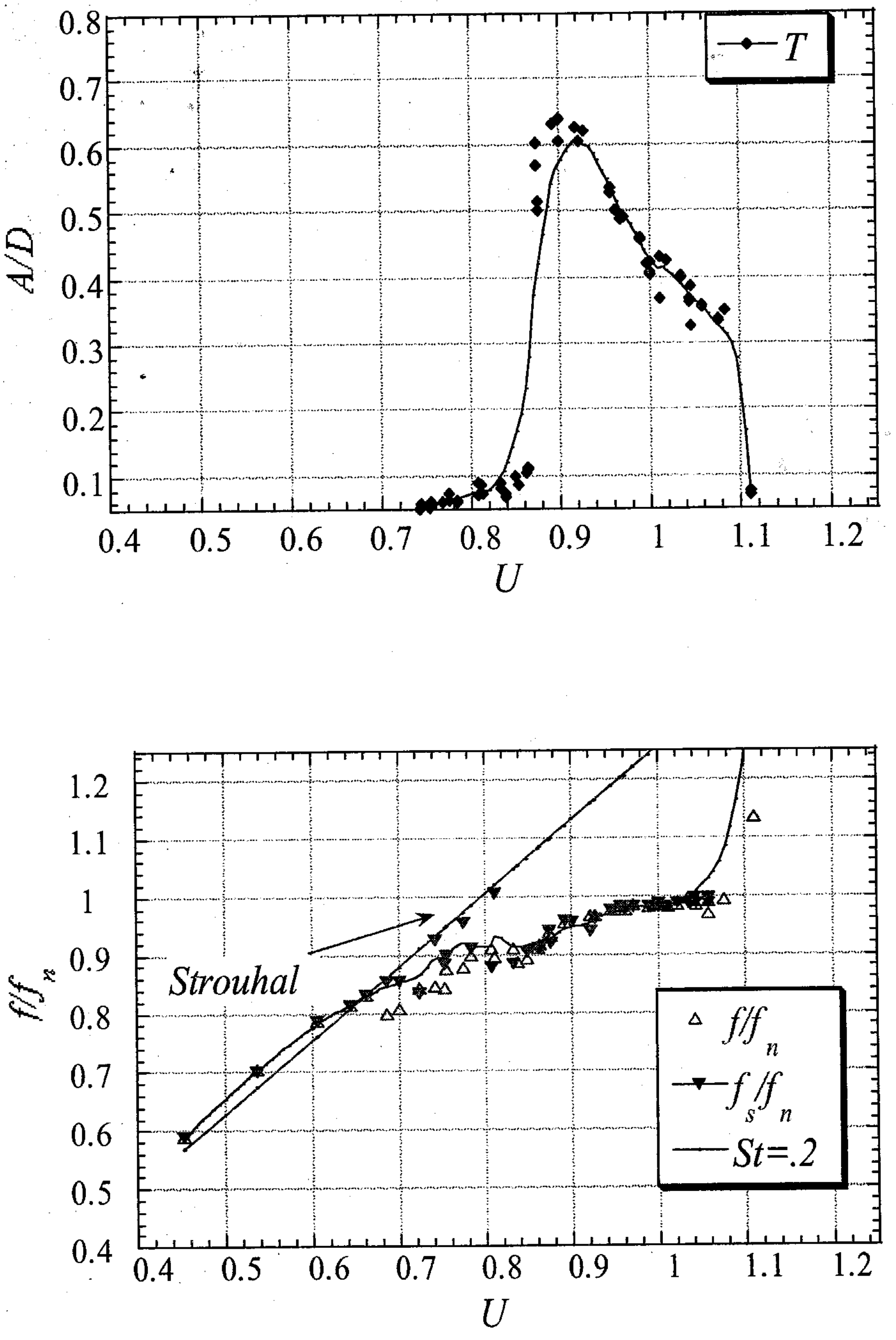

Figure 4.23 Oscillation amplitude and frequency response vs. U for $S1$, $m^*=28$

Figure 4.23 shows what may be considered as a brief tendency towards lock-in for $0.96<U<1.08$. Figure 4.24 shows details of this region and indicates a perhaps slight frequency growth with U.

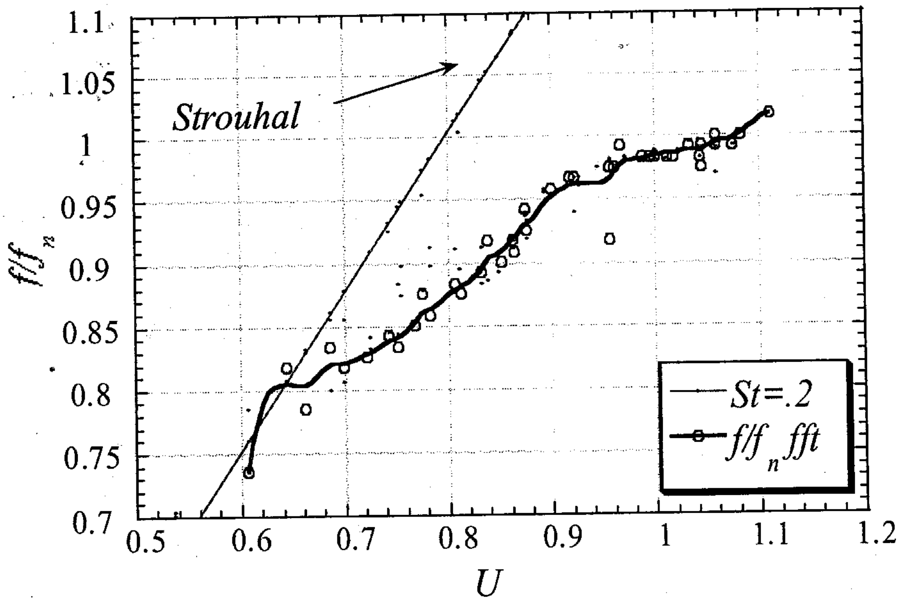

Figure 4.24 Details of frequency f/f_n vs. U, for *S1*, $m^*=28$

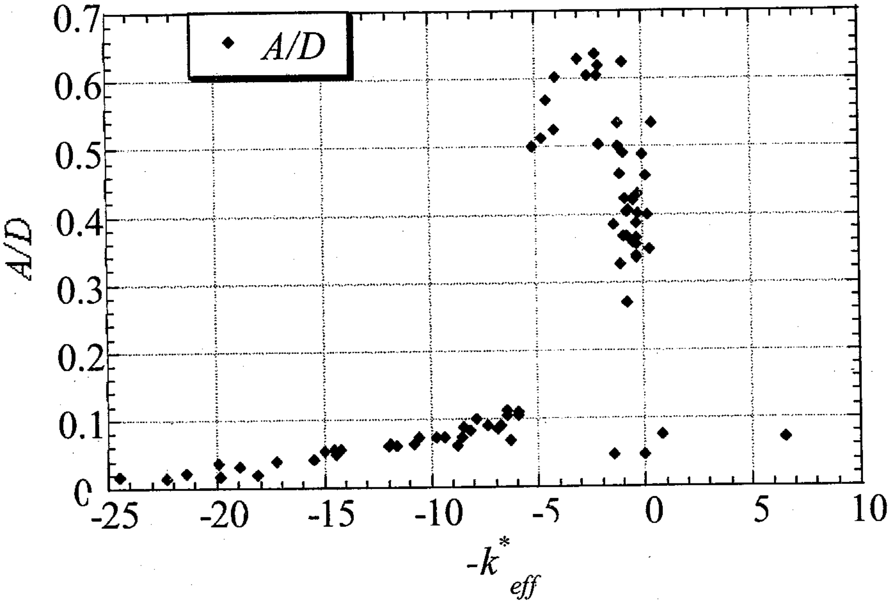

Figure 4.25 Oscillation amplitude vs. $-k^*_{eff}$ for *S1*, $m^*=28$

Figure 4.25 shows the narrow amplitude response as a function of $-k^*_{eff}$. The brief lock-in behavior about U=1.0 is manifested as a sharp decline in f^* in Figure 4.26. Since $k^*_{eff}=k^*-(2\pi f^*)^2m^*$ and $k^*=m^*/U^2$, a decline in f^* results in a slower than expected increase in values of $-k^*_{eff}$ with increasing U as seen in Figure 4.27. The clustering of data points around $-5< -k^*_{eff} <0$ in Figure 4.25 serves to show the importance of k^*_{eff} as a means of predicting *VIV*. It is noteworthy that while k^*_{eff} rests around zero, the damping parameter b^* declines according to $b^*=2m^*\zeta/U$ and affects the phase ϕ between the fluid force and the displacement. This explains the different amplitudes around similar k^*_{eff} values of about zero in Figure 4.25. In other words, while k^*_{eff} is stable, b^* causes a decline in *A/D*. It also clarifies the slow decline in oscillation amplitudes vs. U in the $0.88<U<1.02$ range in Figure 4.23.

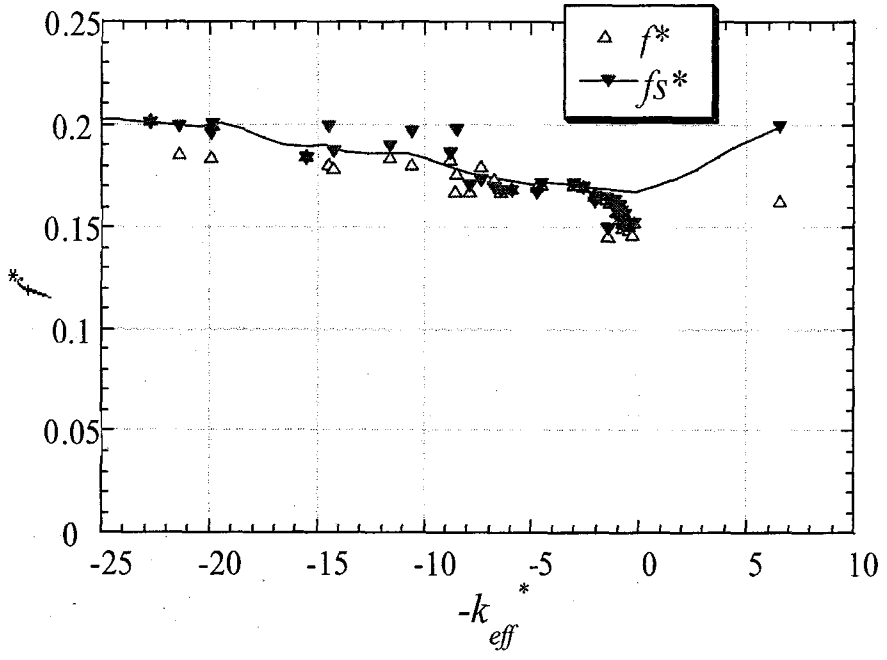

Figure 4.26 Frequency f^* vs. $-k^*_{eff}$ for *S1*, m^*=28

ERROR: VMerror
OFFENDING COMMAND: imagemask

STACK:

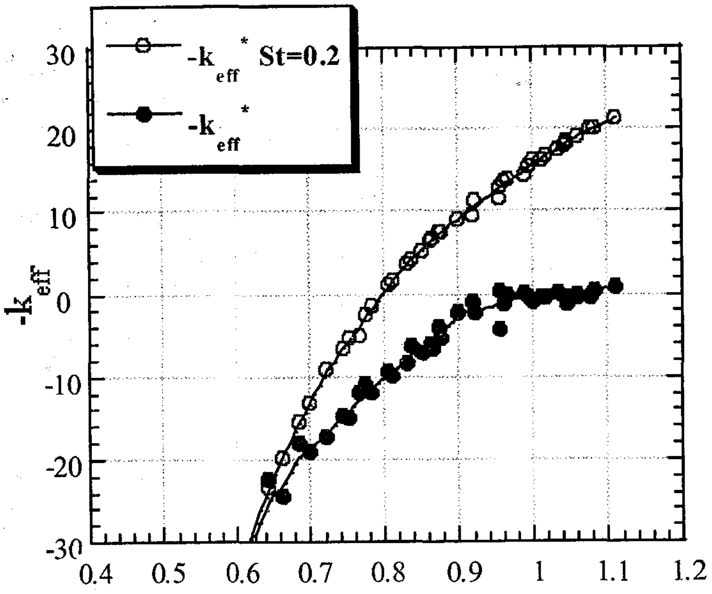

4.8. *S6*: Mass Ratio of 27

The structural parameters for *S6* were as follows:

Case	m^*	$\zeta\times100$	m [kg]	k [lb/in]	f_n [Hz]	D [in]	*Re [10^3]*
S6	27.0	2.7	4.9	30	5.8	1	17-24

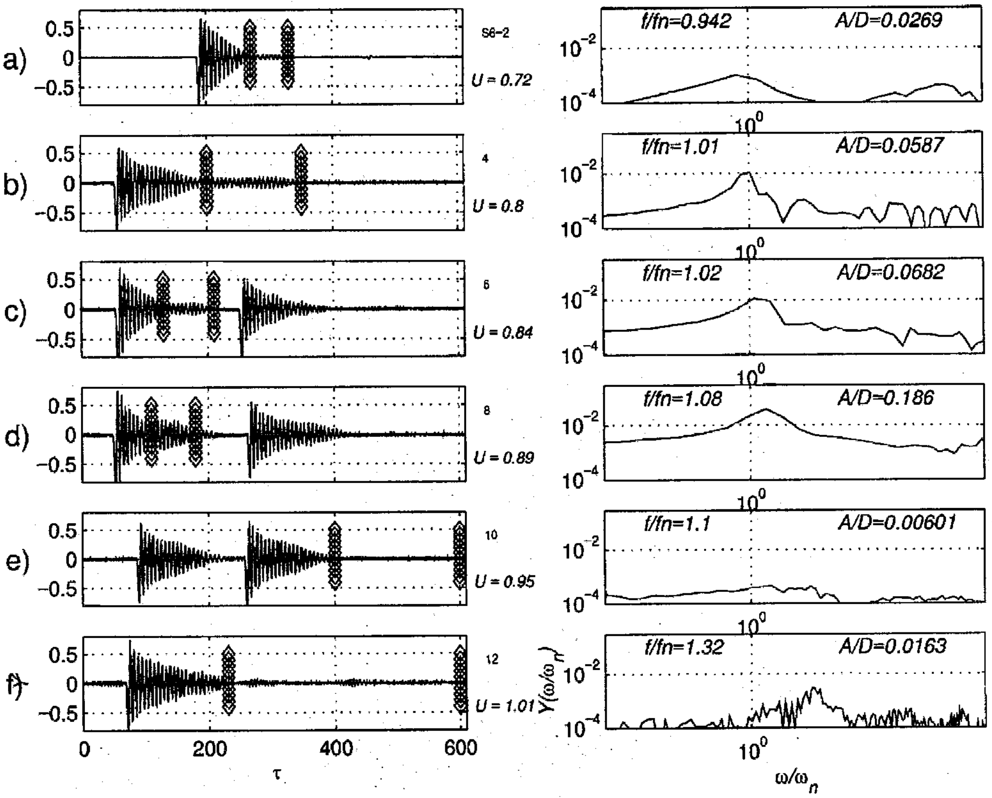

Figure 4.29 Oscillation traces and frequency spectra for *S6*, m^*=27 at a) *U*=0.72, b) *U*=0.80, c) *U*=0.84, d) *U*=0.89, e) *U*=0.95, f) *U*=1.01

Most oscillations were unsteady and only a few continuous traces were detected. The slow time decay of the amplitudes made this case different from most cases studied. *S6* is presented as an example of many cases that do not exhibit *VIV*, despite simple predictions based on damping, mass ratio and frequency matching. It also serves as a counterpart to *S1*, for it exhibits a different behavior despite the close value of the mass ratio parameter.

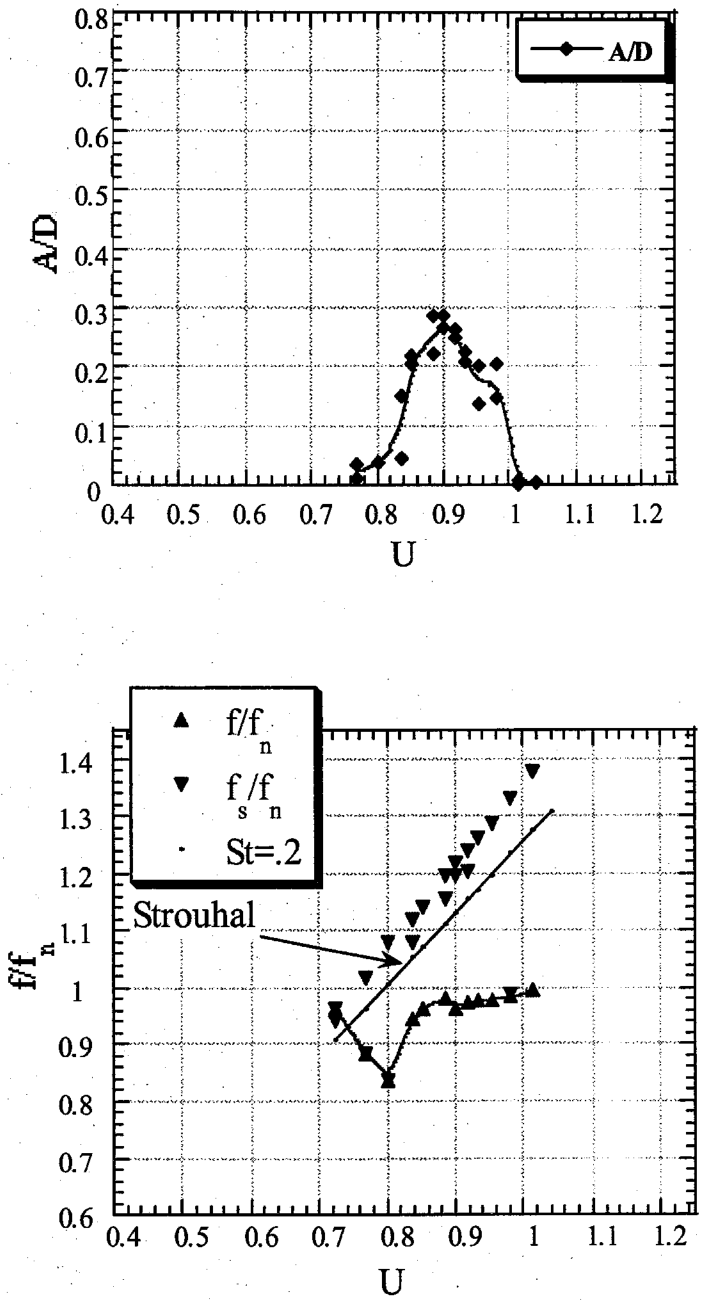

Figure 4.30 Oscillation amplitude and frequency response vs. *U* for *S6*, m^*=27 (*A/D* values are subjective, see Figure 4.29)

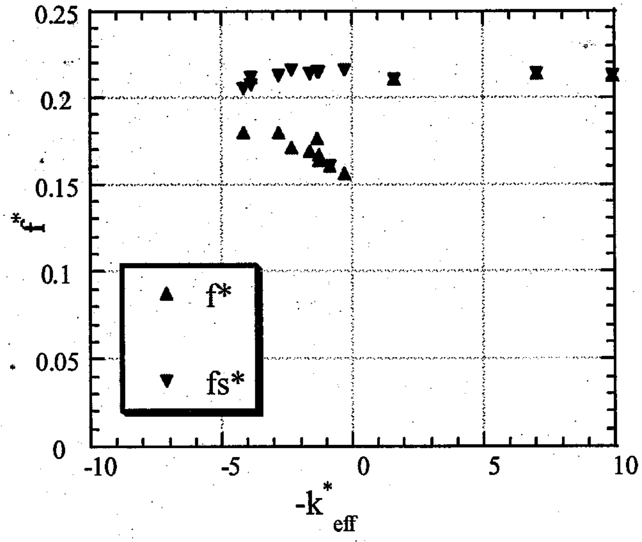

Figure 4.31 Oscillation frequency vs. $-k^*_{eff}$ for *S6*, m^*=27

The fraction of the critical damping ζ is considerably higher than *S1* but not very large compared to some of the other cases studied. This shows the critical role of mass ratio along with damping. The amplitudes in Figure 4.30 were computed based on the oscillatory segments following the jolts and need to be considered subjectively with the actual traces shown in Figure 4.29 in mind. Lack of steady oscillations gives way to the appearance of the nominal Strouhal shedding at some points. The oscillation frequency shows a slow growth with *U*. Damping b^* ranged from 2.0 to 1.36.

4.9. *S5*: Mass Ratio of 39

Case	m^*	ζ×100	*m* [kg]	*k* [lb/in]	f_n [Hz]	*D* [in]	*Re [10^3]*
S5	39.0	2.9	7.13	30	4.7	1	14-21

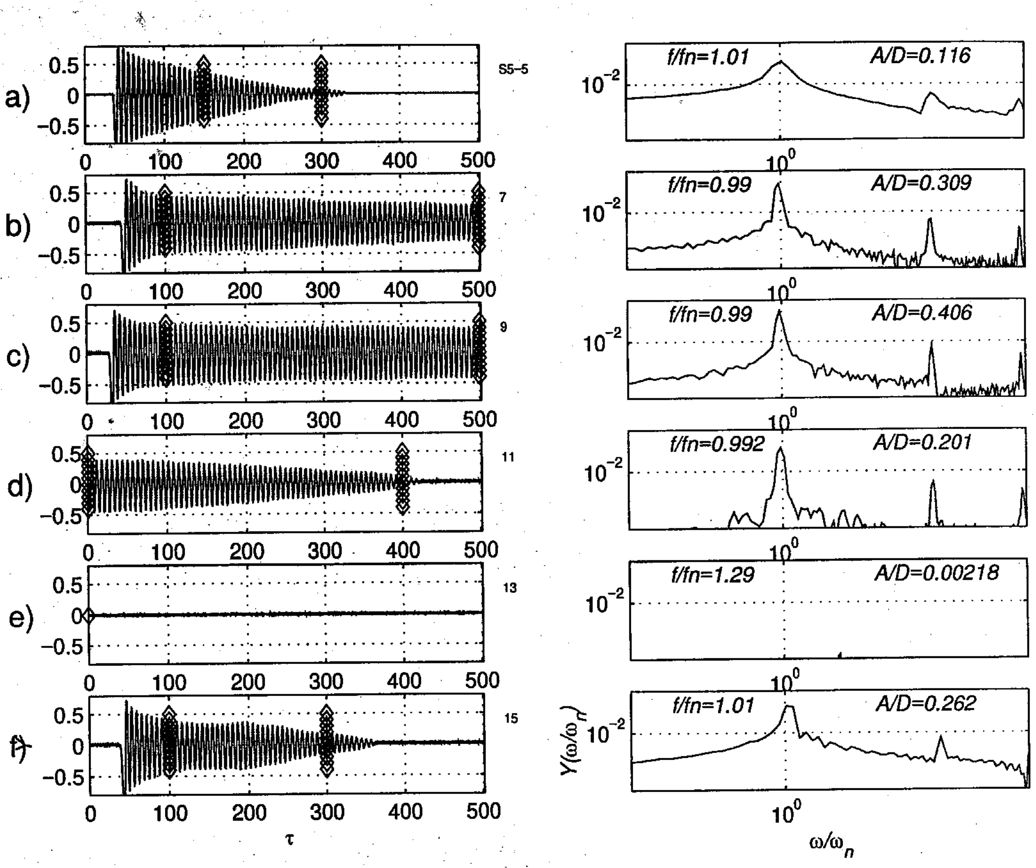

Figure 4.32 Oscillation traces and frequency spectra for *S5*, *m**=39 at a) *U*=0.85, b) *U*=0.90, c) *U*=0.91, d) *U*=0.914, e) *U*=0.95, f) *U*=0.96

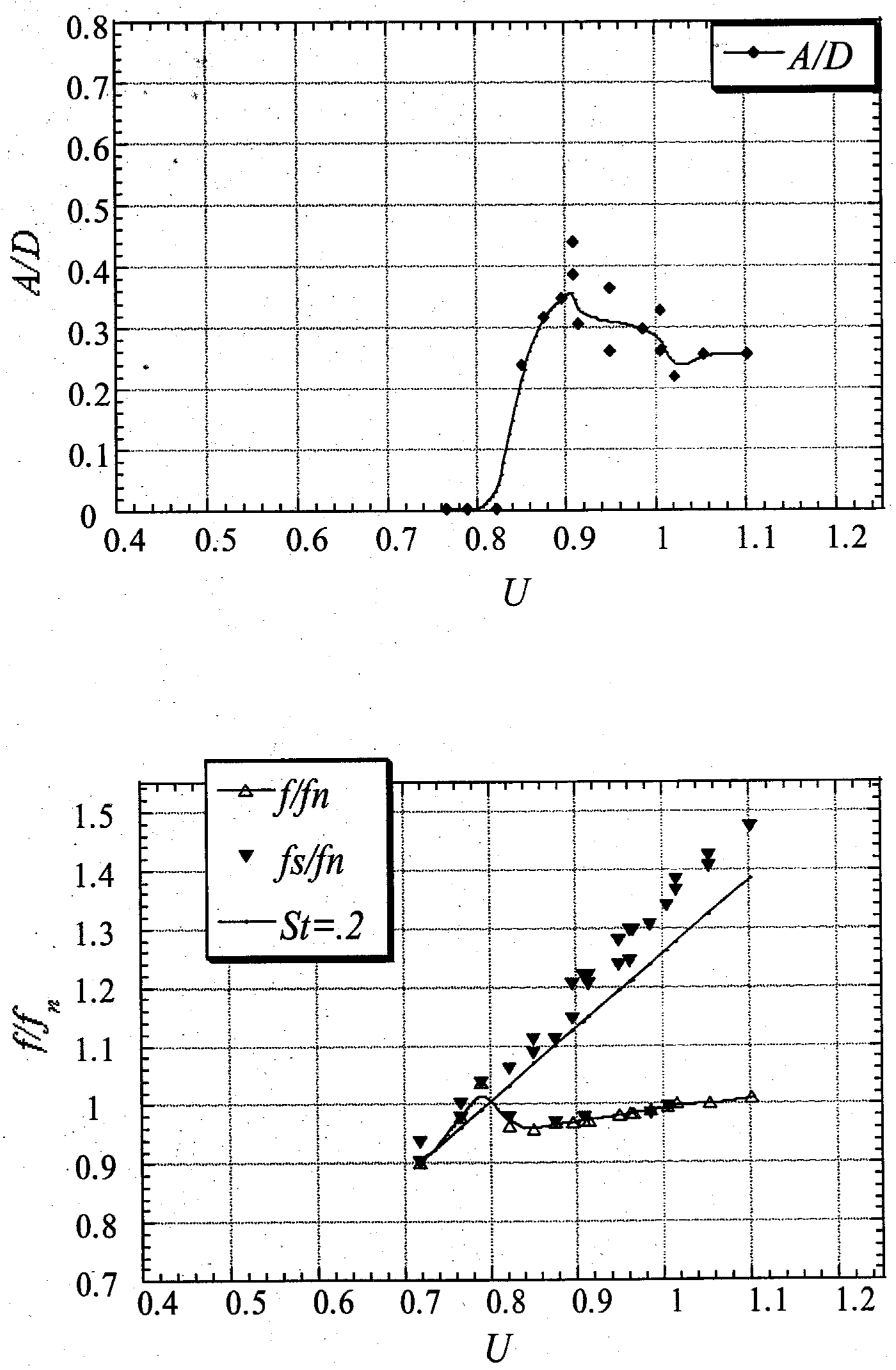

Figure 4.33 Oscillation amplitude and frequency response vs. *U* for *S5*, m^*=39

Despite the large mass ratio and damping, oscillations in *S5* are relatively more stable than *S6* (Figure 4.32). Amplitudes are once again based on the most steady segments within every trace and are occasionally subjective. Figure 4.33 shows the unsteady nature of this case in the form of fluctuating oscillations. Remarkably, steady amplitudes as large as 0.36 are observed. The damping, b^*, ranged from 3.1 to 2.0. The frequency response still shows signs of growth with f/f_n crossing a value of 1.0. Significant response is limited to the $0.8<U<1.1$. Two distinct frequencies are detected throughout this case corresponding to f and f_s.

4.10. *S2*: Mass Ratio of 72

Case	m^*	ζx100	*m* [kg]	*k* [lb/in]	f_n [Hz]	*D* [in]	*Re [10^3]*
S2	72.0	2.1	5.06	94	8.8	0.62	11-13.6

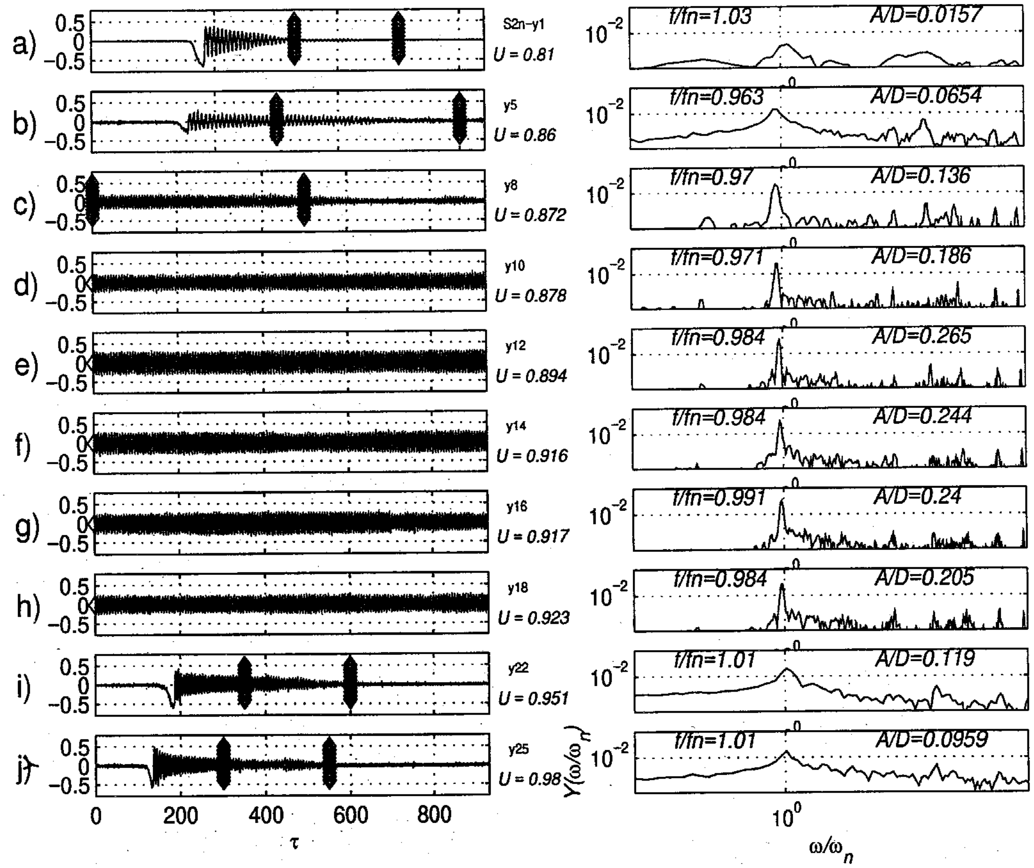

Figure 4.34 Oscillation traces and frequency spectra for *S2*, m^*=72

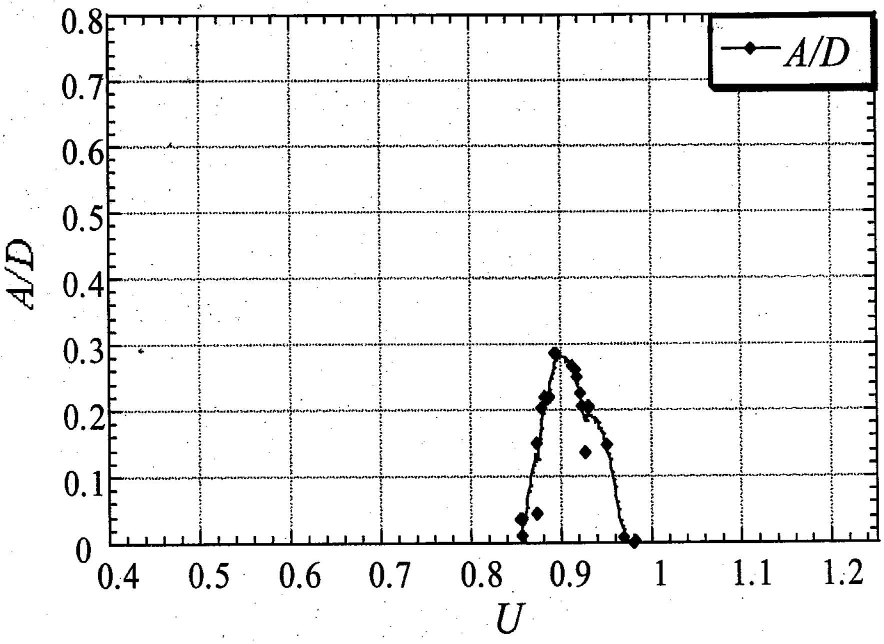

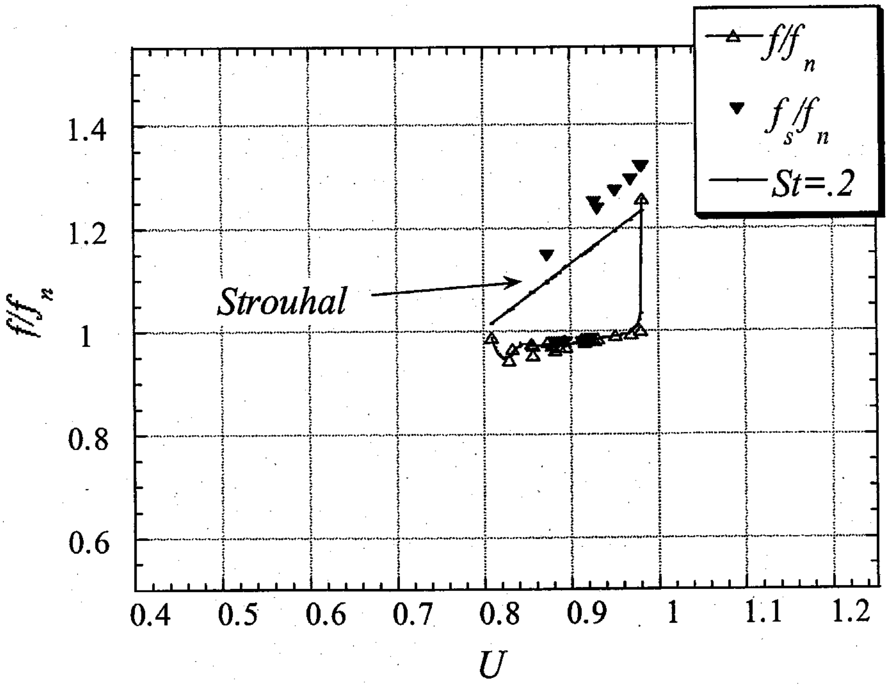

Figure 4.35 Oscillation amplitude and frequency response vs. *U* for *S2*, m^*=72

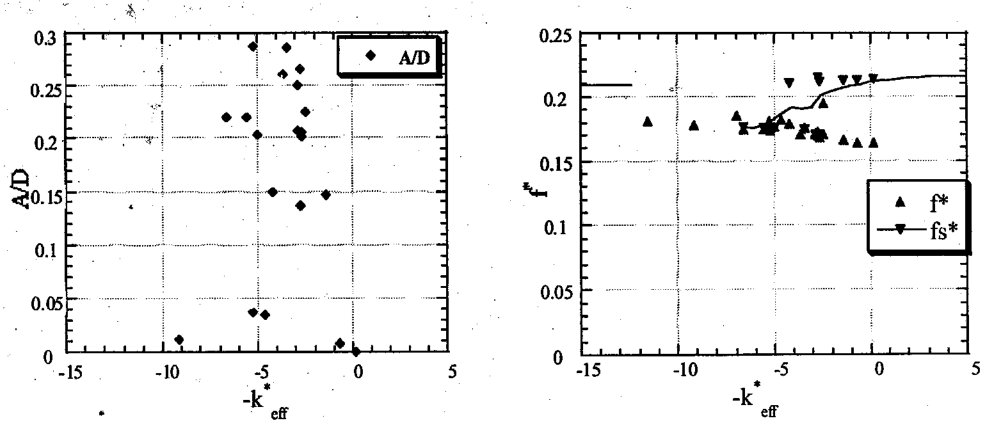

Figure 4.36 Oscillation amplitude and frequency vs. $-k^*_{eff}$ for *S2*, $m^*=72$

S2 shows steady growth in amplitudes within $0.8<U<0.95$. The damping b^* was limited to $4.2>b^*>3.4$. Figure 4.34 shows a slow gradual increase in the frequency. This is the closest behavior to a lock-in within the one-dimensional cases studied in this chapter. The amplitude of oscillation *A/D* and the range of velocities *U* for *VIV* are quite limited as shown in Figure 4.35. The small slope in f/f_n vs. *U* plot translates into a large plunge in f^* values in Figure 4.36 which in return leads to latent growth in values of $-k^*_{eff}$. The attenuation in $-k^*_{eff}$ dimension around zero causes the clustering of points as experienced in *S1*. The changes in amplitude are due to variations of b^* and possibly C_y.

4.11. Detailed Frequency Analysis of a Case Using *EMD*

In this section we consider three points in case *S7*, $m^*=9$ and use Empirical Mode Decomposition (*EMD*, section 2.8) to analyze the frequency content of each trace. The three points involve free stream velocities of $U=0.73$, $U=0.81$, $U=1.06$. For reference, Figure 4.37 contains the corresponding frequency and amplitude data for this case on the same plot. The three points are chosen such that they represent different *VIV* states within a typical run. Figure 4.38 shows the oscillation traces and the frequency spectra for the three points at hand. The first and the third traces contain considerable amounts of instability which usually is an indicator of multiple physical phenomena. The *FFT* peaks for the last two traces are quite sharp while the first trace shows indications of multiple frequencies.

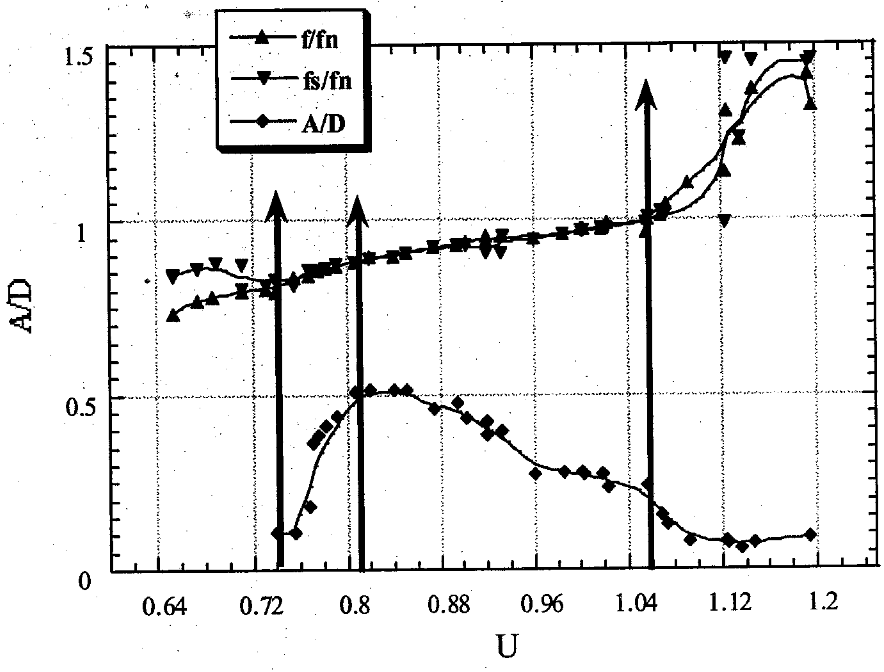

Figure 4.37 Frequency and amplitude response for case *S7*, $m^*=9$ and the three points under study

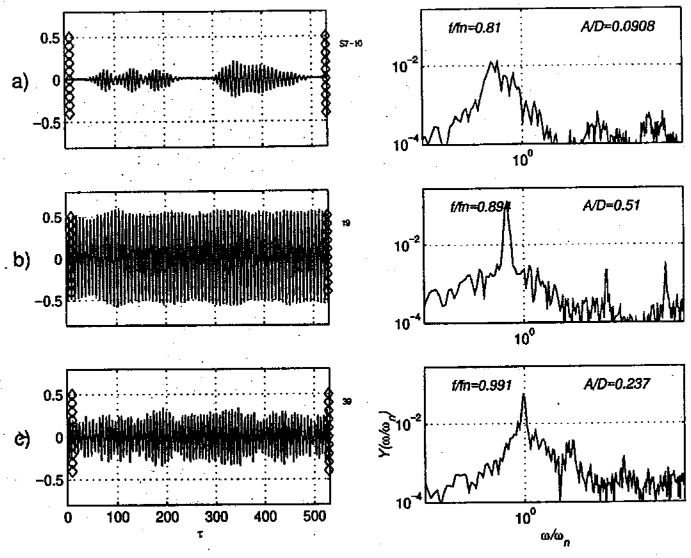

Figure 4.38 Oscillation trace and spectrum at, *U*=0.73, *U*=0.81, *U*=1.06, case *S7*

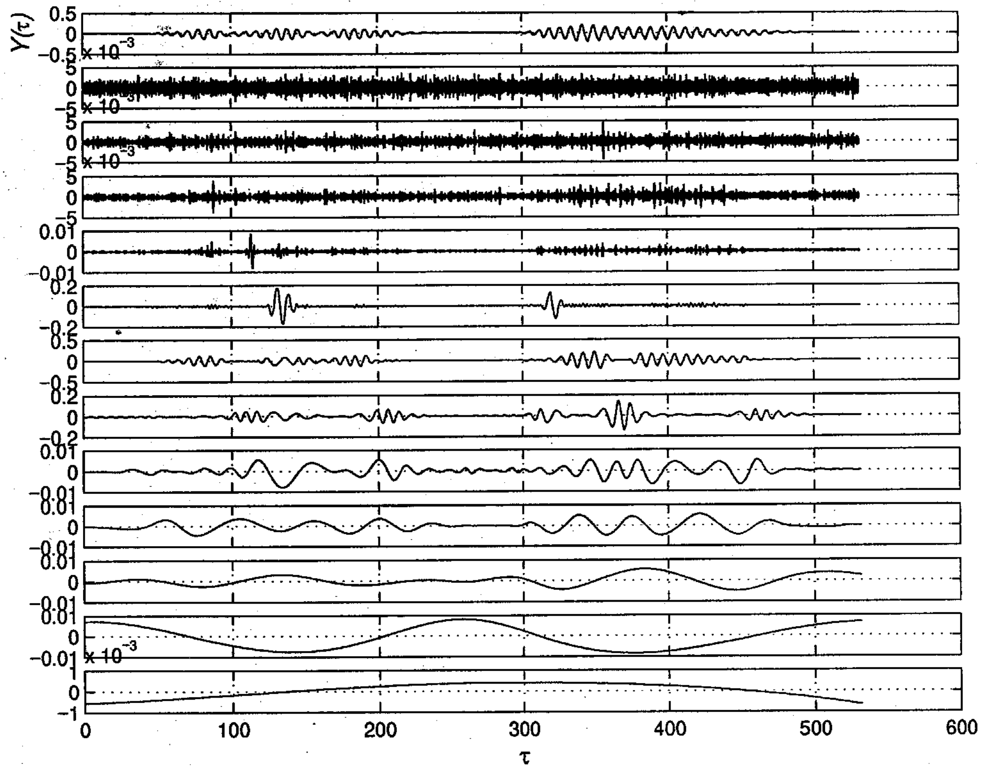

Figure 4.39 The oscillation trace *y(τ)/D* and the *EMD* components at U=0.73

Figure 4.39 shows the oscillation trace *y(τ)/D* on the first row and the *EMD* extracted components of the signal on the following rows (the intrinsic or empirical modes). Each mode here contains a different physical time scale. The first three components seem to be simply noise. Noting the small *y* scale for most components, we may focus our attention on rows 5 to 10 and specifically, rows 6, 7, and 8, where the main signal components reside. Figure 4.40 shows a close-up view of the fourth to tenth modes (rows 5 to 11). Once again noting the amplitude scales, we may consider the modes 5 to 7 to represent the main phenomena. The fourth mode seems to be noise with possibly turbulent intermittency. Modes 8 to 10 seem to be small subharmonic components either due to the fluid state or a simple structural response. The 5th mode seems to contain some profound intermittency that may be attributed to a sudden change in vortex shedding pattern from the body. Since the oscillation frequency and the shedding are known to be different for this trace, it is plausible that vortices tend to shed at different points within the oscillation path, occasionally causing shifts in shedding pattern. Modes 6 and 7 are the main physical phenomena and may be related to the shedding and structural motions. The effects of the two modes seem to be staggered such that one mode gives rise to the other and vise versa. It seems as if the shedding and oscillation, although not synchronized, act in a flywheel manner to attain an oscillation first but counteract later causing the oscillation to decay.

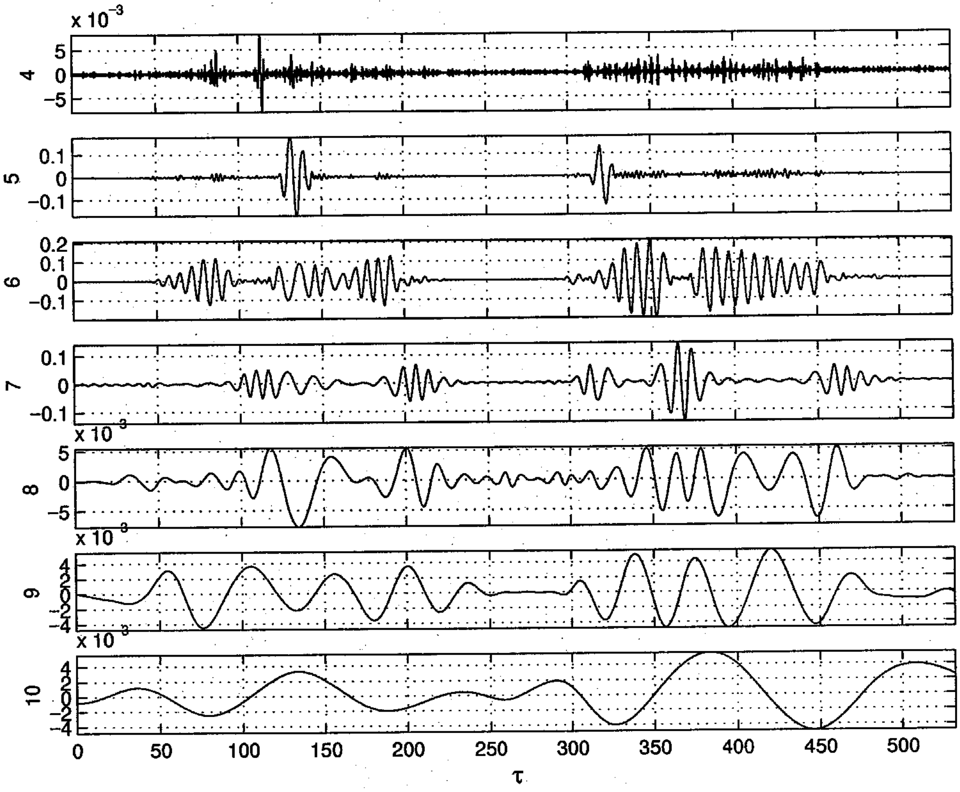

Figure 4.40 Detailed view of the *EMD* components at U=0.73, case *S7*

Figure 4.40 shows a close up view of the *EMD* components for the point with *U*=0.81. The first row depicts the original trace *y(τ)/D* and the following rows show the third to ninth modes extracted. Modes 1 and 2 and 10 to 12 are not shown due to their physical similarity to corresponding modes in the previous point studied. Although this trace involves a very stable *VIV* oscillation, the overall nature of the modes is surprisingly similar. Modes 3 and 4 seem to be small scales phenomena related to noise or turbulence while the main *VIV* phenomenon seems to be present in modes 5 to 7. Mode 5 shows intermittent jolts corresponding to points within the main signal where amplitude and frequency changes are visible. Mode 6 contains most the signal energy and surprisingly presents pronounced intermittent behavior. Modes 7 to 9 seem to be subharmonic effects with small magnitudes.

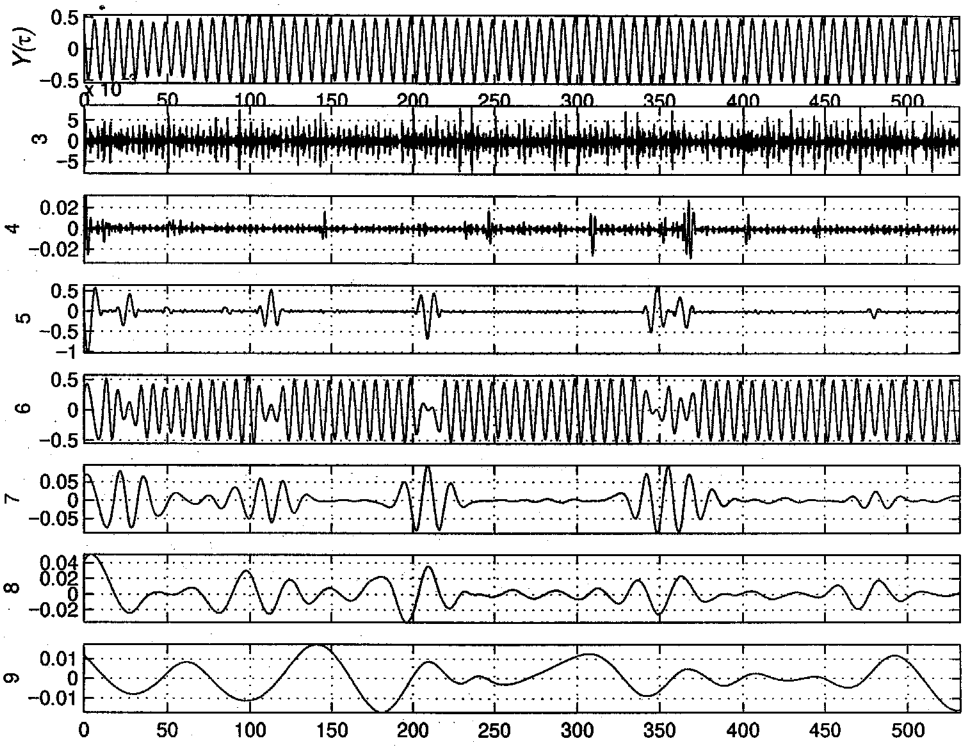

Figure 4.41 Detailed view of the oscillation trace *y(τ)/D* and the *EMD* components at U=0.81, case *S7*

The next point studied involves a free stream velocity of *U*=1.06 and a small local peak in the amplitude response curve in Figure 4.37. Figure 4.42 shows a detailed view of the oscillation trace which present a considerable amount of amplitude and frequency variation. Figure 4.43 shows all modes extracted through *EMD*. Once again, the three first modes involve low magnitude, high frequency content most probably related to noise.

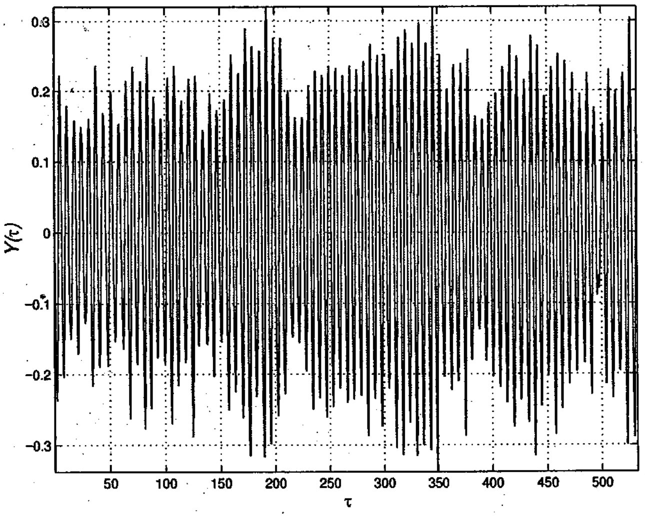

Figure 4.42 Oscillation trace at U=1.06, case $S7$

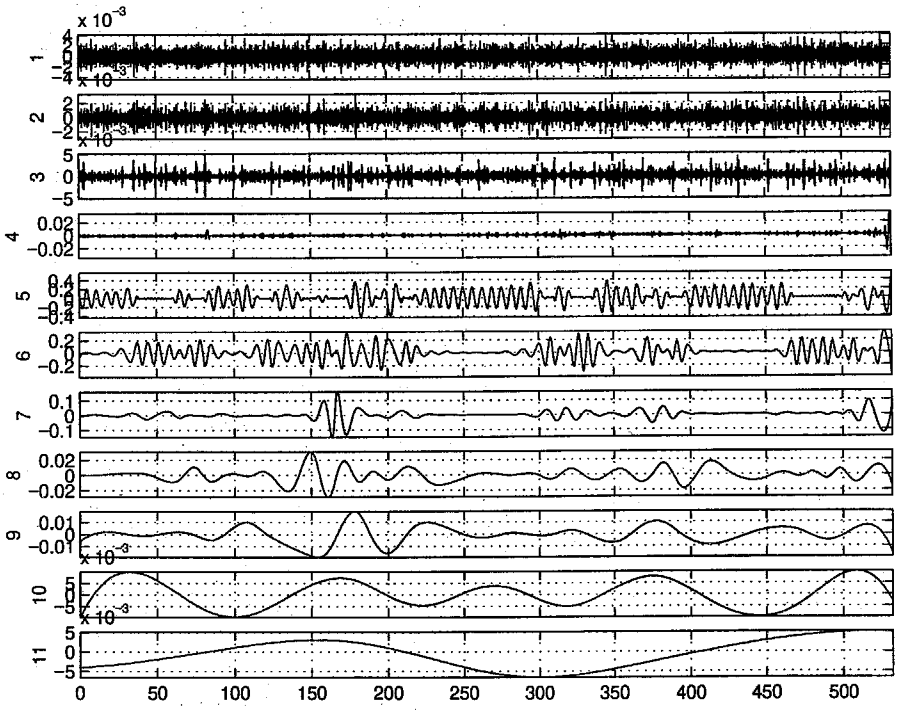

Figure 4.43 *EMD* components at U=0.81, case *S7*, *U*=1.06

Figure 4.44 shows a detailed view of the 4th to 9th *EMD* modes. Modes 5 to 7 seem to represent the main *VIV* behavior. The overall *VIV* oscillation seems to be broken into two main phenomena with intermittent jolts about a hundred cycles apart. The amplitudes in modes 5 and 6 seem to be more uniform throughout each trace as compared to the original signal. Once again the shedding and the structural forces seem to be involved in a flywheel manner to add to or nullify each other's effect.

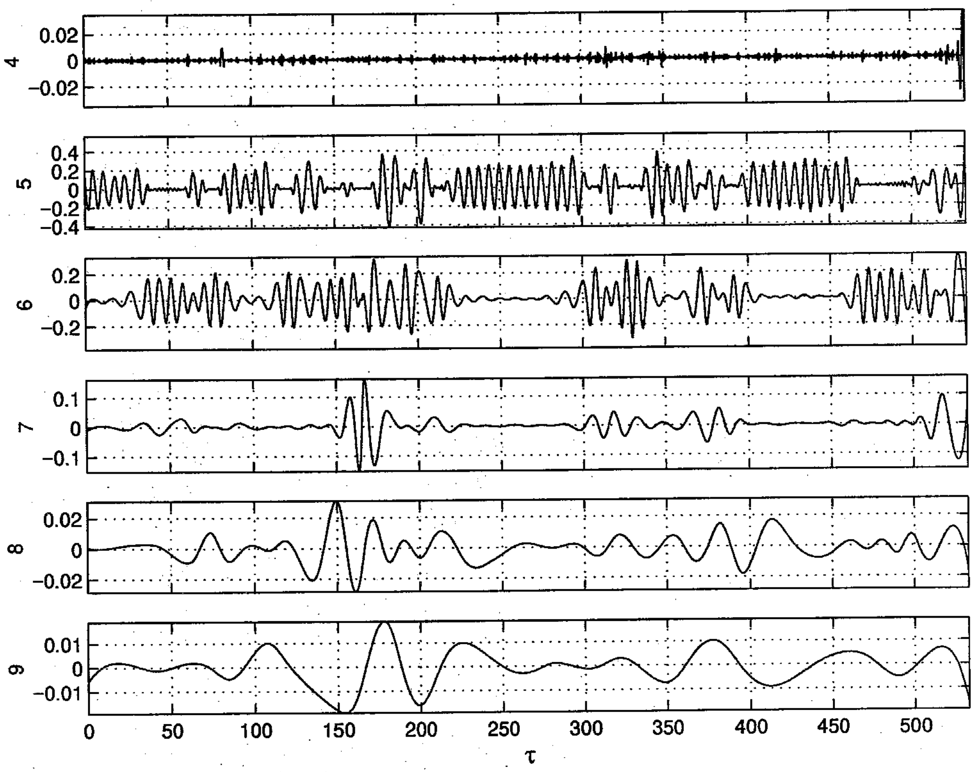

Figure 4.44 Detailed view of the oscillation trace $y(\tau)/D$ and the *EMD* components at U=1.06, case *S7*

4.12. Conclusions

4.12.1. Non-lock-in Behavior

A new *VIV* mode dominates most cases studied that does not involve a lock-in behavior. Vortex-induced lock-in is simply absent in most cases studied. There are no signs of lock-in in three experiments involving a mass ratio of 9 (*S7*, *R5*, and *R10*) or less (*R3* and *R6*). The case *S1* with m^* =28 shows a small region with slow frequency growth with U and *S6* with m^* =27, contains a slow growth at all times. Overall, the frequency response, f/f_n vs. U, seems to flatten and approach the limit of lock-in with increasing values of mass ratio m^*. The above observation does not preclude the existence of lock-in at low mass ratios but rather confirms a *VIV* mode that does not involve lock-in. As will be seen in chapter 5, lock-in can indeed be present at very small mass ratios.

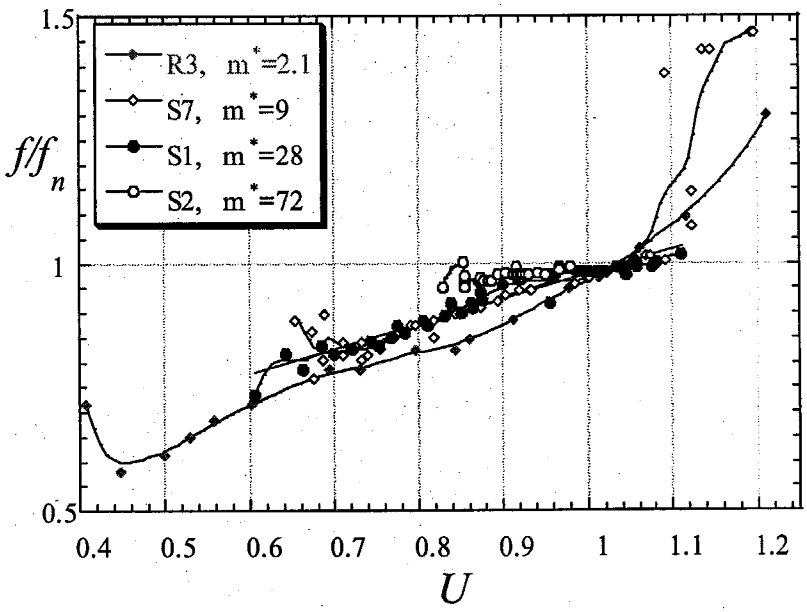

Figure 4.45 Frequency response with increasing mass ratios m^*=2.1, 9.0, 28, 72

Figure 4.45 shows the frequency response for four cases with mass ratios between 2.1 and 72. Although all cases reflect similar degrees of deviation from the Strouhal frequency (St=0.21), the detail behavior is quite different. Once the oscillation amplitude is diminished, the Strouhal frequency reappears as expected. It is worth noting that the frequency growth always deviates to values below the Strouhal frequency and not above. This in general extends the period for the growth of each vortex shed.

4.12.2. Amplitude Response

Figure 4.46 shows the oscillation amplitudes for the same four cases discussed above. The amplitude *A/D* and the velocity range in *U* for *VIV* diminish with increasing values of mass ratio m^*. In a few cases studied, larger values of mass ratio attained larger, steadier amplitudes. Case *S1*, m^* =28, is such exception in that it displays a larger maximum amplitude than *R5* and *S7*, m^* =9, despite the larger mass ratio. The lower value of the damping parameter ζ and the flatter lock-in-like frequency in *S1* explain this behavior.

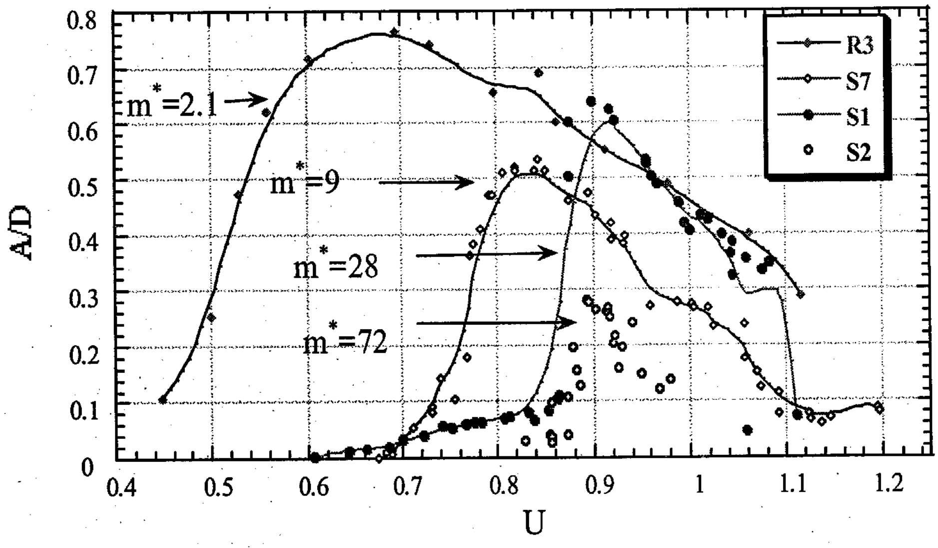

Figure 4.46 Amplitude response with increasing mass ratios m^*=2.1, 9.0, 28, 72

The amplitude response curves, *A/D* vs. *U*, have different overall shapes. These shapes vary from round and smooth at small values of m^* <6 to double-peaks with humps at medium values of $5<m^*<30$ as reported by Khalakh and Williamson [1997] (m^*=2) and finally to intermittent behavior at large values of $m^* > 30$. Damping and possibly different shedding modes may be important.

4.12.3. Effective Stiffness k^*_{eff}, Comparison with Shiels' Results

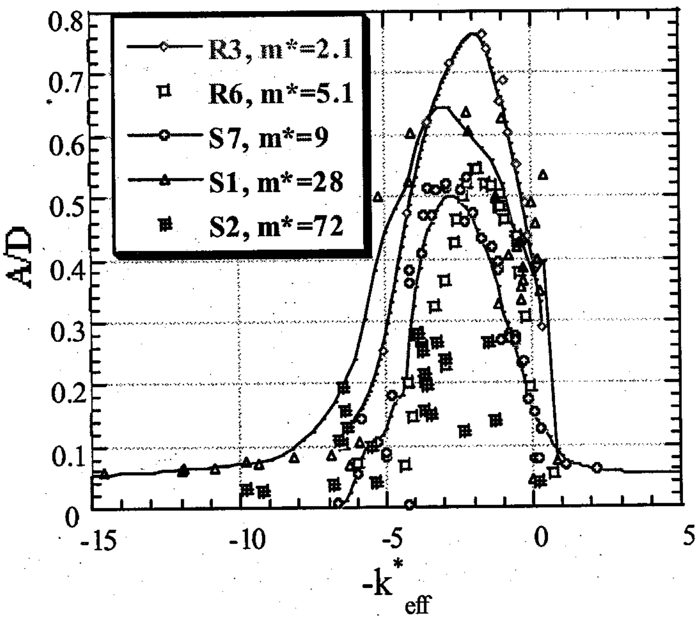

Figure 4.47 Plots of amplitude vs. effective stiffness

Figure 4.47 shows the amplitude response, *A/D,* for a few cases involving a large mass ratio range of $2.1 < m^* < 72$ vs. the effective stiffness. As mentioned in section 2.9, effective stiffness, $k^*_{eff} = -m^* \omega^{*2} + k^* = (m^*/U^2)(1-(f/f_n)^2)$, was proven by Gharib et al. [1997] to be the singular controlling parameter in *VIV* for zero values of damping b^* at $Re=100$. In that range, the amplitude response *A/D* was shown to be simply $A/D = C_y/k^*_{eff}$ regardless of individual values of k and m^*. Although damping in the experimental cases is non-zero, the data clusters in the $-8 < -k^*_{eff} < 0$ range. The maximum amplitude variation in Figure 4.47 is mainly due to differences in damping and the lift coefficient C_y.

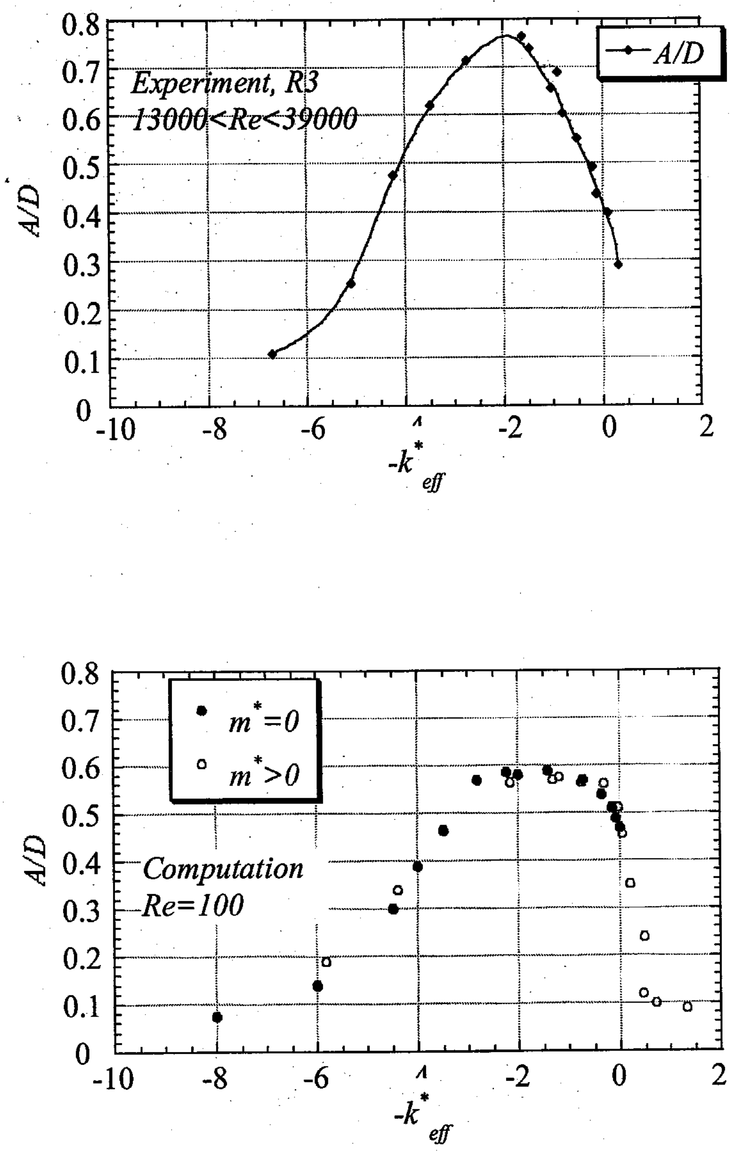

Figure 4.48 Comparison of case *R3* (left) with numerical results of Shiels [1998]

According to the effective stiffness formulation, $C_y = A/D \times k^*_{eff} = A/D \times (m^*/U^2)(1-(f/f_n)^2)$, large oscillation amplitudes in this chapter are due to small mass ratio. Without lock-in ($f/f_n \sim 1$), *VIV* oscillations detected in case S_1 (m^*=28) would require an large lift coefficients greater than 10. The effective stiffness also explains the large amplitudes detected in Feng's experiment [1968] with a large mass ratio of m^*=389. The amplitudes in Feng's experiment seem very large compared to the diminishing trend observed in this chapter with increasing mass ratio. The explanation is that a lock-in behavior with $f/f_n \sim 1$ as observed in Feng's experiment is the only manner effective stiffness parameter can be minimized. The product of a large term ($m^*=389$) and a very small term ($(1-(f/f_n)^2) \sim 0$) renders similar k^*_{eff} values as observed in this chapter. In fact plotting Feng's data on A/D vs. k^*_{eff} can render similar plots as in Figure 4.47.

Figure 4.48 shows the low m^* case *R3* as compared to the computational results of Shiels. The two curves contain similar overall shape despite the large differences in the *Reynolds* number and damping b^*.

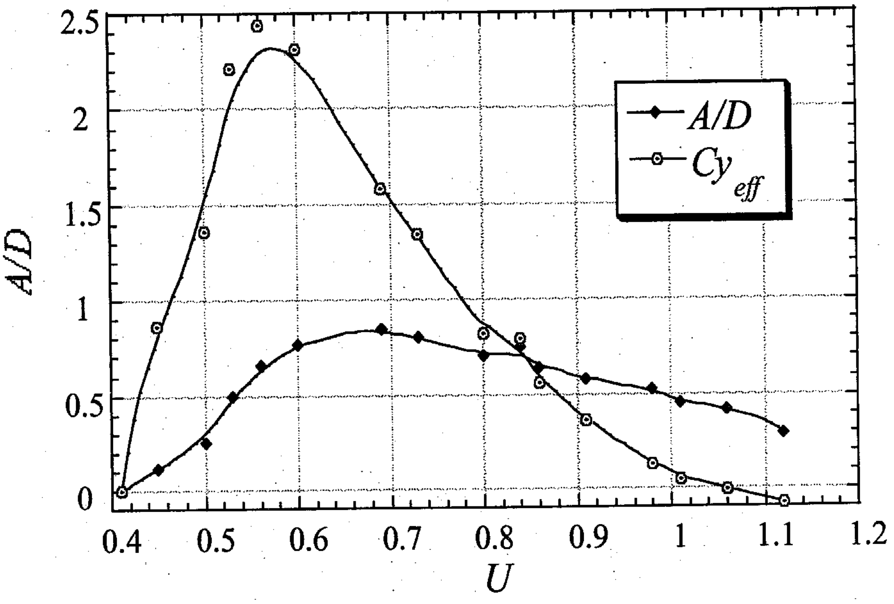

Figure 4.49 Amplitude and single frequency lift estimate according to

$C_{yeff}= A/D\times k^*_{eff}$ for *R3*, $m^*=2.1$

Figure 4.49 shows the amplitude response along with a single frequency estimate to the lift coefficient. It simply uses $C_{yeff}= A/D\times k^*_{eff}$ neglecting the complete frequency content of the trace and the structural damping. The large lift coefficients ($C_y>2$) are remarkable. The values increase when damping and the full frequency content of each trace is included. A higher order technique will be discussed in chapter 6.

4.12.4. Comparison with Feng's Results

In aeroelastic studies such as Feng's [1968] (Figure 4.50) where the mass ratios exceed 200 (m^*=389 in Feng's case), the classical lock-in is the only cause of large *VIV* amplitudes. The wide range of the oscillation regime with respect to U and the large amplitudes achieved in Feng's experiment are quite remarkable in comparison to the present results. According to the effective stiffness theory (section 2.9, $A/D=C_y/k^*_{eff}$), the only cause for such large amplitudes at nominal values of the lift coefficient, C_y, is very small values of k^*_{eff} throughout the free stream velocity range U. Since by definition $k^*_{eff}= -m^*\omega^{*2}+k^* =(m^*/U^2)(1-(f/f_n)^2)$, to minimize k^*_{eff}, f/f_n needs to be very close to 1 as is the case in Feng's experiment. Such lock-in behavior has been absent in most *VIV* experiments studied in this chapter. We may conclude that *VIV* is not necessarily synonymous with lock-in; however, the odds of simple *VIV* due to sheer magnitude of the fluid forces is higher than *VIV* with a lock-in at such small mass ratios. The existence of nominal values of damping has little effect on the final conclusion in this argument. In chapter 5 (section 5.3), a partial lock-in at m^*=8.9 will be discussed.

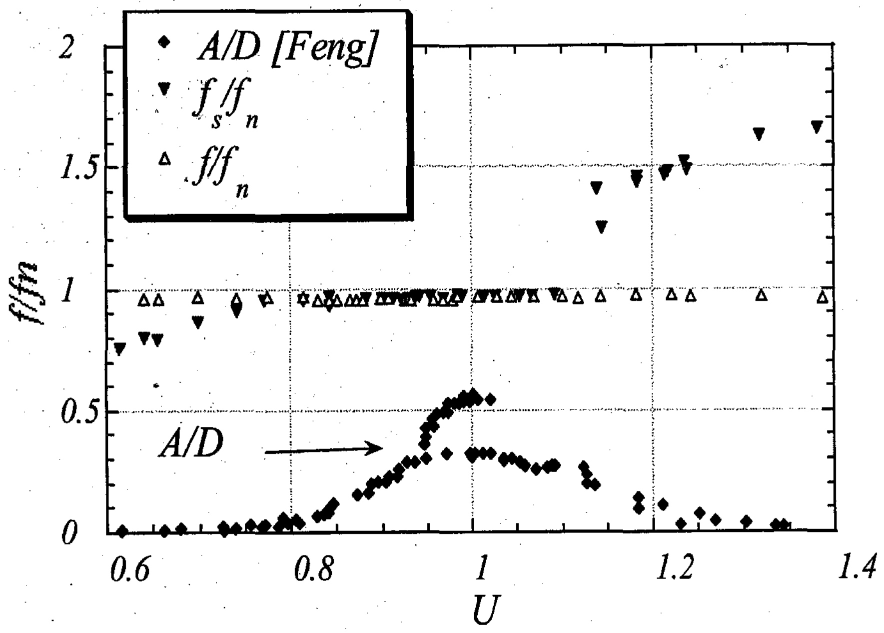

Figure 4.50 Frequency and amplitude response in Feng's classical experiment

4.12.5. New *VIV* Mode

The new *VIV* mode is depicted on the left hand side of Figure 4.51 via a series of amplitude response curves ($2.1<m^*<72$) that exhibit diminishing oscillation amplitude with increasing mass ratio m^*. This new mode represents oscillations due to large fluid force compared to the system structural parameters. These cases do not exhibit strict lock-in in the classical fashion and do not seem to reach the relatively pronounced amplitudes in Feng's high mass ratio case. Although damping plays an important role, lock-in is the primary reason behind the large amplitudes recorded in Feng's case.

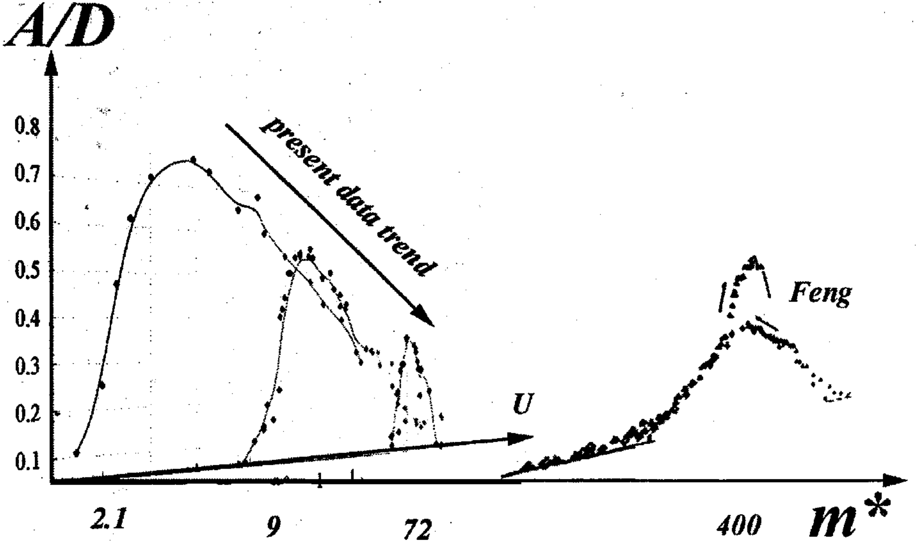

Figure 4.51 New *VIV* mode for $2.1<m^*<72$ with diminishing amplitudes with increasing mass ratio in contrast to Feng's large mass ratio experiment (right)

4.12.6. An Explanation of the Non-lock-in Behavior

A simple explanation of the non-lock-in phenomenon can be given in terms of the dominance of the non-dimensional fluid-structural forces present. The two large structural forces, the inertial and the elastic, tend to nullify as the natural frequency is approached. The magnitude of the damping force is usually quite small and that of the fluid force is inversely proportional to the mass ratio m^*.

$$\ddot{Y}+\zeta\dot{Y}+Y=\frac{1}{2m^*}C_yU^2$$

In aeroelastic applications with typical values of m^* above 200, the fluid and the damping forces are relatively small and the large structural terms dominate the flow and the vortex shedding process, that is the structural motion is a forcing term to the "fluid system," similar to forced oscillation experiments. In hydroelastic applications, on the other hand, the smaller values of m^* give rise to a large fluid term forcing the structural system as in classical forced structure problem. The higher fluid forcing frequency gives rise to a higher structural frequency response.

4.12.7. Comparison with the Williamson-Roshko Plane

To properly obtain shedding modes, the vorticity field for every free stream velocity is needed. The purpose of this study was to map the *VIV* parameter domain so that select crucial points could be chosen for vorticity field mapping using *DPIV*. Superimposing the amplitude and the frequency results upon the Williamson-Roshko plane, however at this stage, places almost all free oscillation data presented here on the so-called *2P* region. It is worth noting that the W-R plane corresponds to forced oscillation experiments and may not be applicable for the free quasi-periodic oscillations at hand. The main point here is that unlike the detailed study of Brika and Laneville [1994], our points do not necessarily follow any *2P-2S* boundaries. In fact a variety of behavior is observed for different mass ratios, mostly on the higher wavelength side of the map which corresponds to lowered values of f^* ($\lambda/D=1/f^*$). Figure 2.11 in chapter 2 can be referred to for comparison with Brika and Laneville.

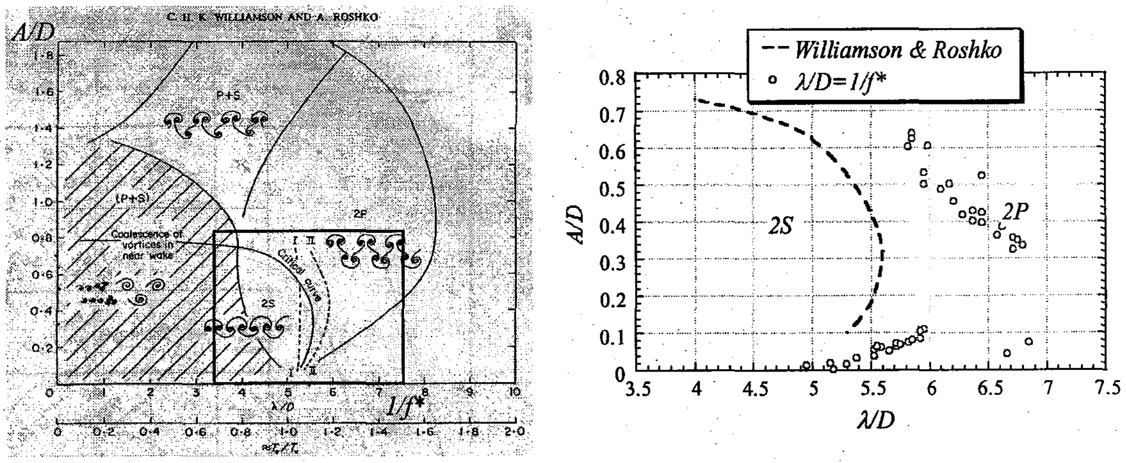

Figure 4.52 *S1*, m^*=28 and the Williamson-Roshko plane

4.12.8. Non-dimensionalizing the Parameters Using f_{Amax} Instead of f_n

As seen in Figure 4.45 and Figure 4.46, the frequency and amplitude curves are not centered about a unique value of *U* with the higher mass ratio cases centered around larger values of *U*. To treat this problem, the natural frequency measured in fluid is used by some researchers to non-dimensionalize the experimental parameters. This technique works to some extent since the natural frequency of light systems in vacuum is usually quite larger than that in water and that of large massive systems relatively close in water or vacuum.

Figure 4.53 shows the oscillation and shedding frequencies vs. the free stream velocity U_{Amax} for a few cases with m^*<40, where all parameters are non-dimensionalized using f_{Amax}, the oscillation frequency of the system at the maximum oscillation amplitude attained within every case. This simple technique tends to remarkably align the frequency curves along both axes and simplify a slope comparison. The frequency values for this range of mass ratios seem to cluster within a narrow band displaying a growth in frequencies with no lock-in but with a similar deviation from the Strouhal nominal frequency.

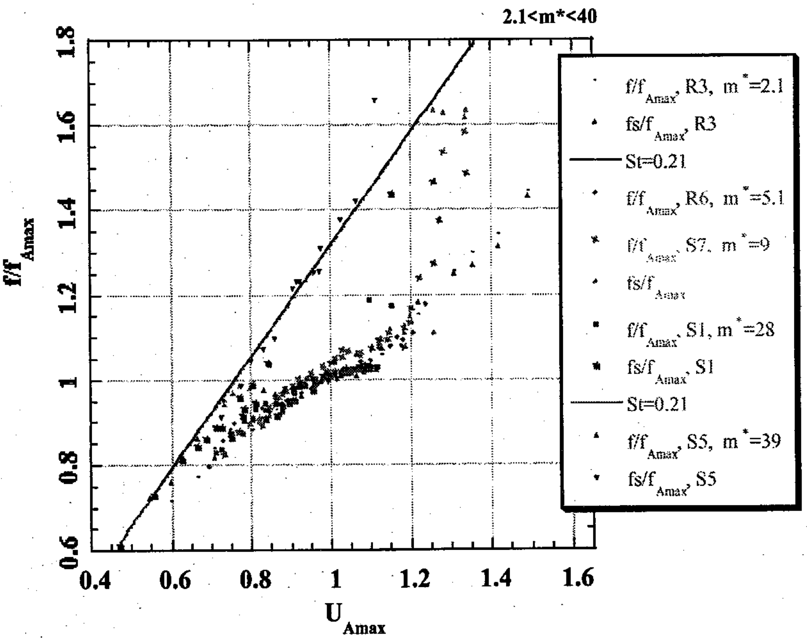

Figure 4.53 Oscillation and Shedding frequencies with m^*<40

Figure 4.54 shows a detailed view of the frequency data vs. U_{Amax} with 2.1<m^*<72. Linear fits are used for points with 0.8< U_{Amax}<1.1. The lines become darker and thicker with increasing m^*. According to this view, most cases with m^*<30 have similar frequency slopes and the large mass ratio cases involve slower frequency growths.

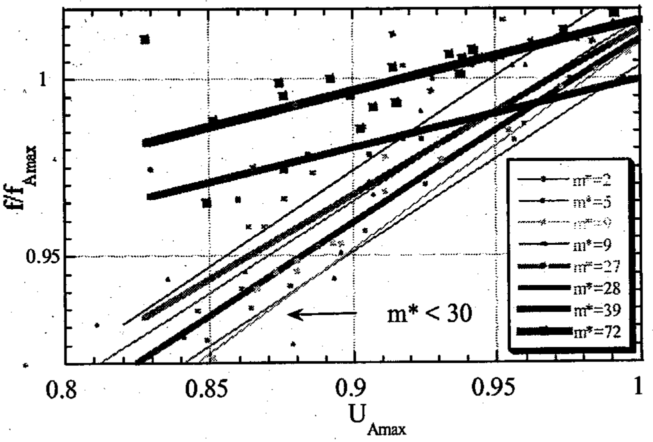

Figure 4.54 Detailed view of the frequency data for cases with $2.1<m^*<72$

4.12.9. Quasi-periodicity and Synchronization

Most cases exhibit multiple frequencies with the shedding frequency f_s and the oscillation frequency f co-existing in the oscillation traces. At free stream velocities, where the shedding and the natural frequency do not coincide, there is usually a large gap between the shedding and the oscillation frequency. The competition between the f and f_s to dominate the oscillation causes much unsteadiness. The two frequencies, however, merge and steady oscillations of considerable amplitude are established once the shedding frequency is within a critical distance from the structural frequency. Results from Empirical mode decomposition reveal that the two frequencies continue to co-exist within most nominally steady traces. They seem to act in a flywheel effect, perpetuating the oscillations in steady regions or nullifying each other in unsteady cases. This effect proves a fundamental difference between the forced single frequency experiments and free elastic cases such as the one at hand. Min addition, most fluid models fail to capture this behavior.

CHAPTER 5

Two-Dimensional Oscillations

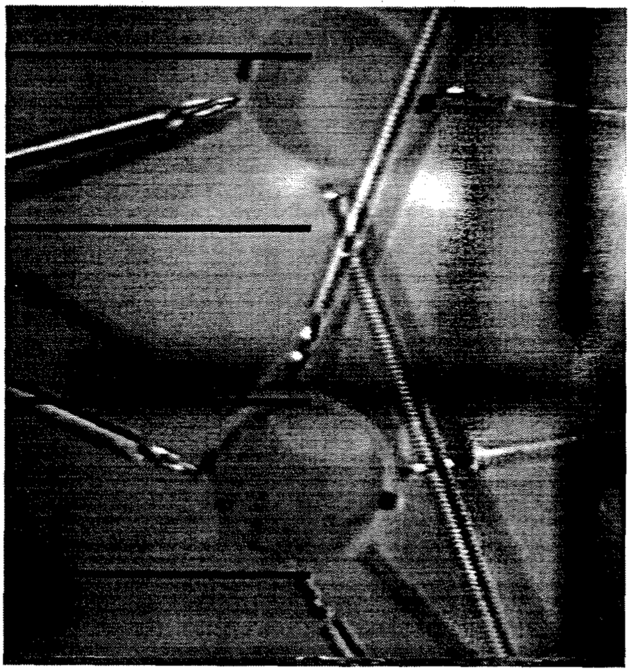

5. Two-Dimensional Oscillations

5.1. Introduction

This chapter describes four experiments involving two-dimensional vortex-induced vibration. Two-dimensional oscillation refers to figure eights motion of the cylinders in the x and y directions. Although the cases studied here show a different behavior from the most one-dimensional cases presented in chapter 4, they serve to reconfirm the absence of lock-in within a much different experimental setting. Two-dimensional oscillations are also important for their common occurrence in nature.

The first two cases presented, *R1* and *R2*, use the same apparatus as discussed in chapters 3 and 4. They involved mass ratios of 2.1 and 8.9 similar to the one-dimensional cases *R3* and *R10/S7* and are noteworthy for their divergent behavior. The last two cases, *O1* and *O2*, were part of the preliminary experiments and used a simpler free spring system along x and y. They are significant for their extremely low values of mass ratio and damping, resulting in a much wider range of oscillations and steady frequency growths U with amplitudes above 1.0.

5.2. *R2*, Two-Dimensional Oscillation, m^*=2.1

R2 involved equal values of elastic stiffness k_x and k_y but different masses m_x and m_y in the x and y direction.

Case	m^*_y	m_y	k_y	f_{ny}	ζ_y	m^*_x	m_x	k_x	f_{nx}	ζ_x	D	$Re[10^3]$
R2	2.1	1.62	2.4	2.47	.034	1.18	1.01	2.4	2.96	0.08	2.1	16-61

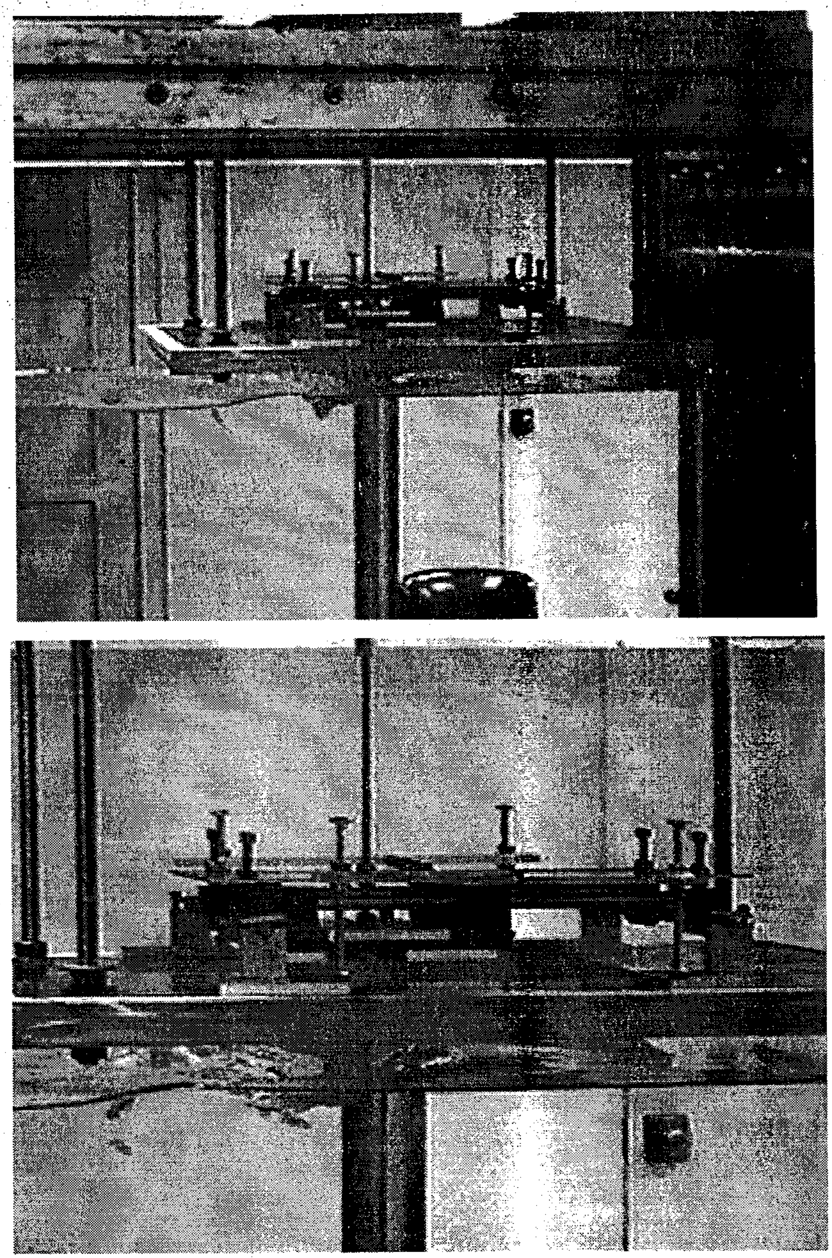

Figure 5.1 Two-dimensional oscillation of *R2*, m^*=2.1. Water surface lowered for display

Equal values of stiffness created a radial restoring force linearly proportional to the radial distance r from the equilibrium position.

$$\vec{F}_r = -k_r \vec{r}$$

This structural restoring force is similar to that of a clamped/free cantilever structure in cross flow without the three-dimensionality caused by bending. There are, however, 3D flow effects due to non-uniform displacements along the span. Figure 5.2 shows the oscillation traces along the y axis. The oscillations along x exhibit a similar behavior.

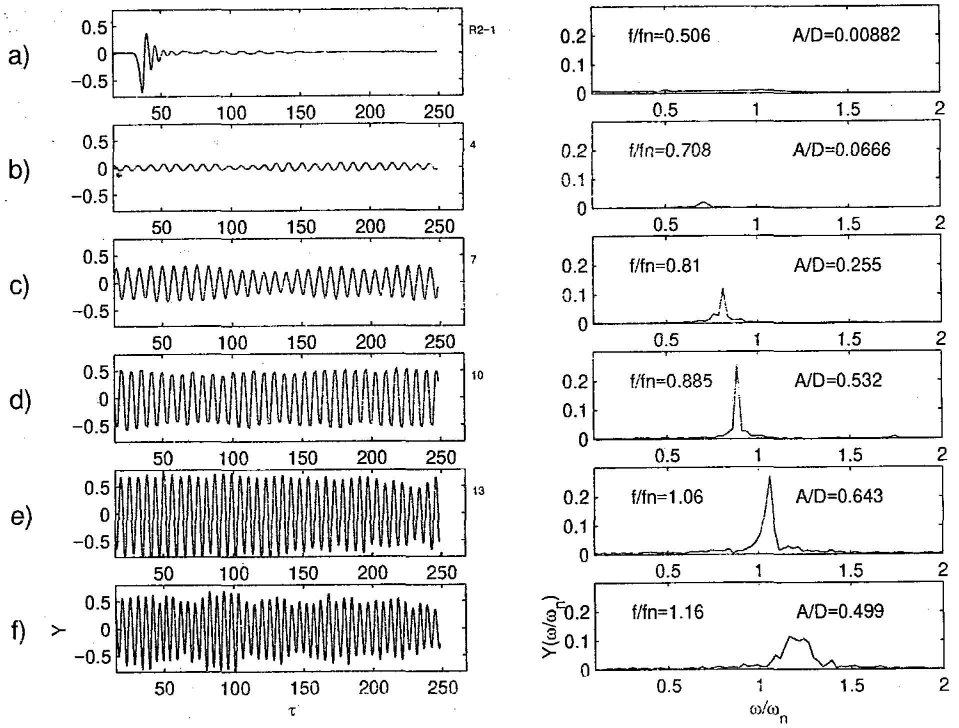

Figure 5.2 Oscillation traces and frequency spectra for case *R2*, m^*=2.1, at a) U=0.37, b) U=0.54, c) U=0.73, d) U=0.87, e) U=0.97, f) U=1.21

The small mass ratio in this case is comparable to that of *R3* studied in chapter 4. The maximum amplitude of oscillation, however, is less than that of *R3* despite the smaller value of damping. The frequencies f_s and f are very close and increase with increasing U, similar to *R3* with no signs of lock-in except for a few wobbles (Figure 5.3). A maximum amplitude of A/D=0.69 is reached at U=1.01 and a maximum deviation form nominal shedding at U=1.16 and A/D=0.53 with f^*=0.147. The amplitude A/D in this case refers to displacements in y. Although there are two distinct natural frequencies in x and y, a double peak in amplitude response was not observed. The maximum tunnel speed was u=115 cm/sec which corresponds to U=1.36. This was the upper limit for the

LDA system. The large fluid forces on the cylinder and the higher levels of turbulence in the flow prohibited faster runs.

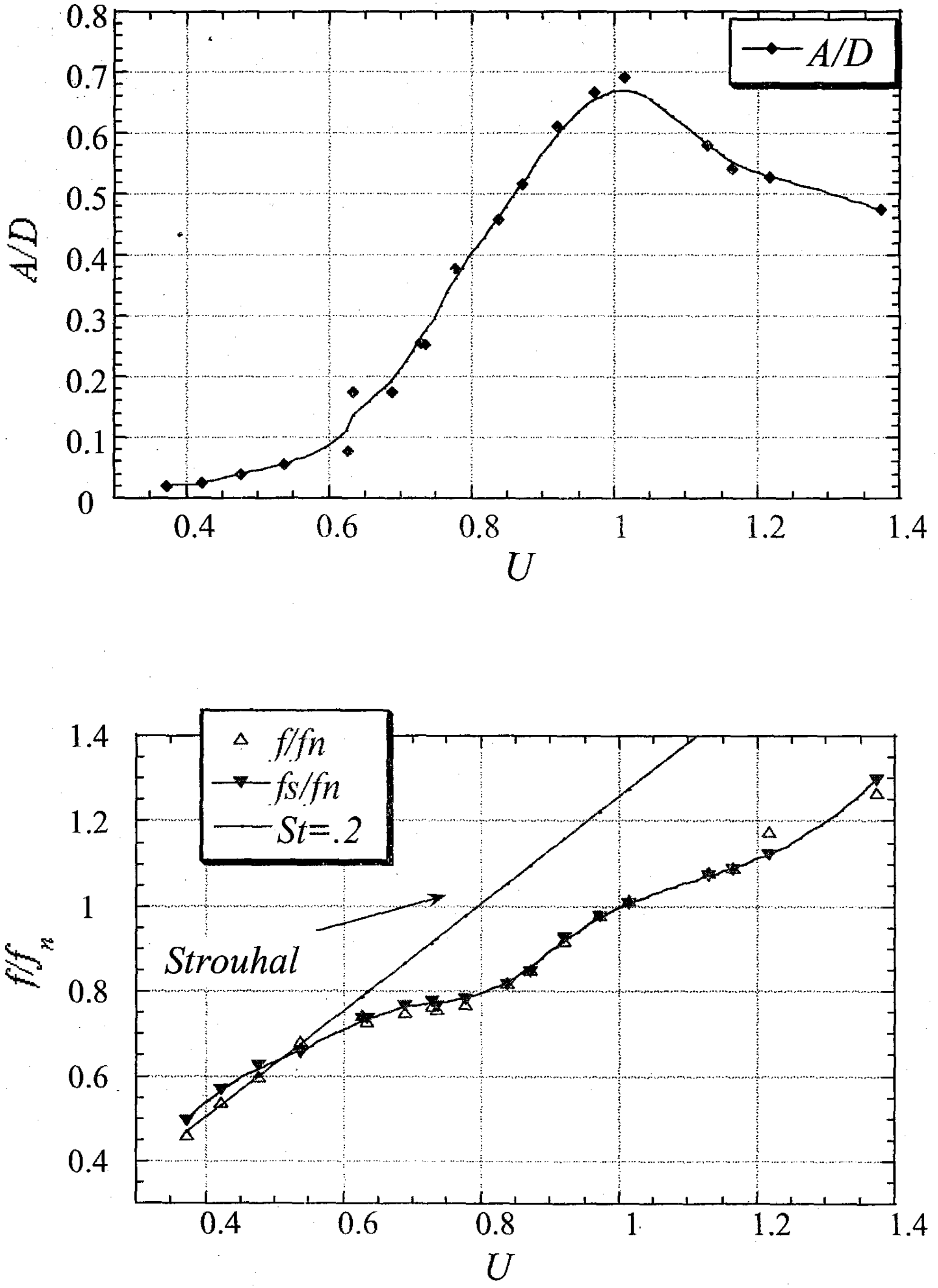

Figure 5.3 Oscillation amplitude and frequency vs. *U*, *R2*, m^*=2.1

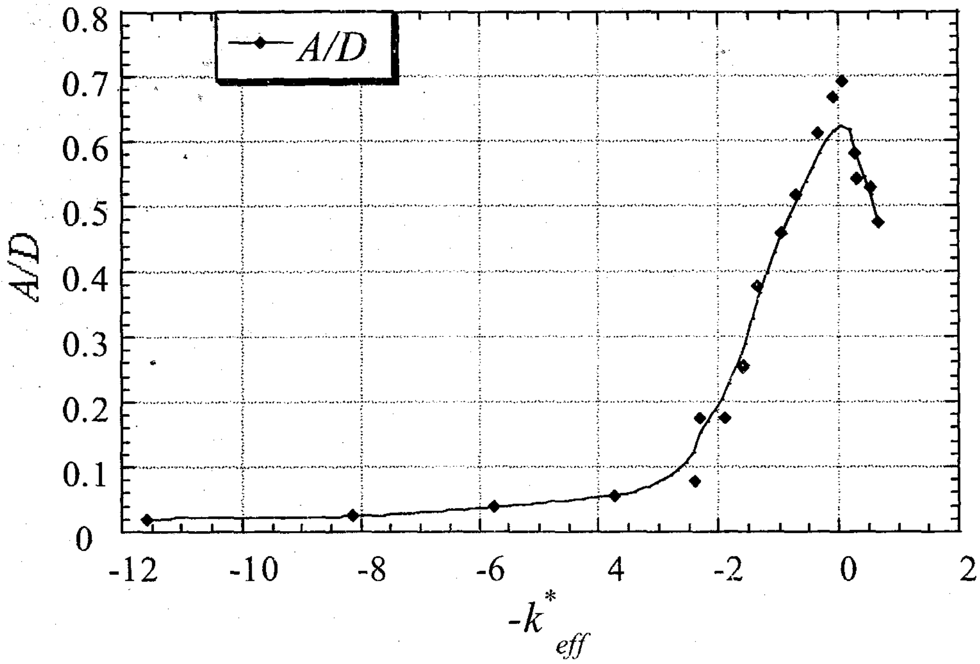

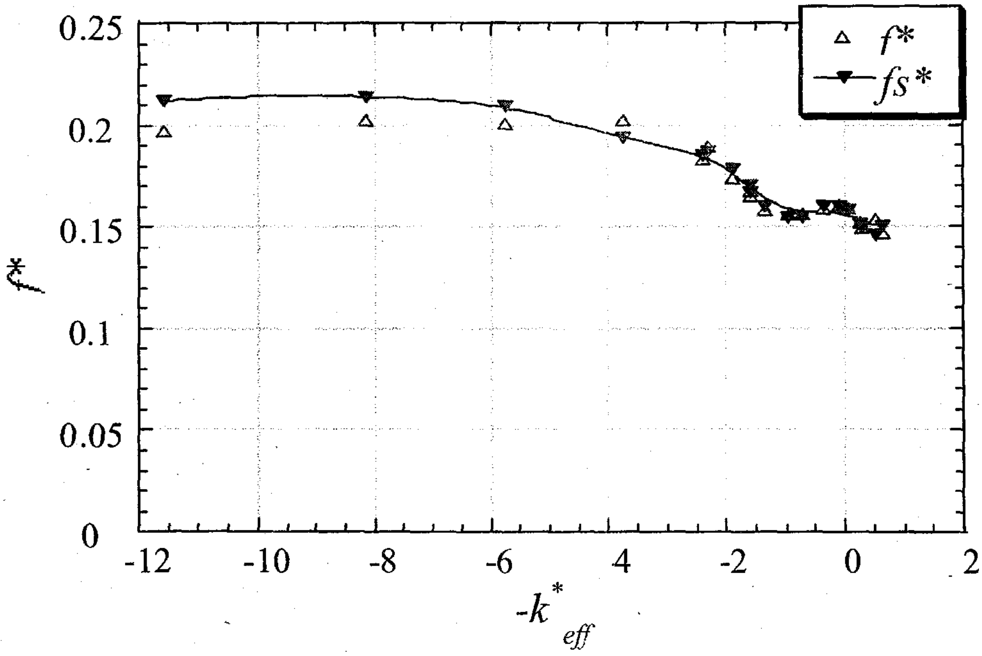

Figure 5.4 Oscillation amplitude and frequency vs. $-k^*_{eff}$ for $R2$, $m^*=2.1$

Figure 5.4 shows the narrow band of $-2<k^*_{eff}<2$ for resonant oscillations. Although the concept of effective stiffness was derived for one-dimensional oscillation, it can be useful in two-dimensional cases as well. This is mainly because the *x* and *y* traces are correlated in frequency. Figure 5.5 shows the *x(t)/D* and *y(t)/D* oscillation traces and the figure eight pattern at *U*=0.97. The *x(t)* trace seems to possess a non-stationary short time average. Although amplitudes reach a maximum value of *A/D*=0.8, the least square time averages value is *A/D*=0.67.

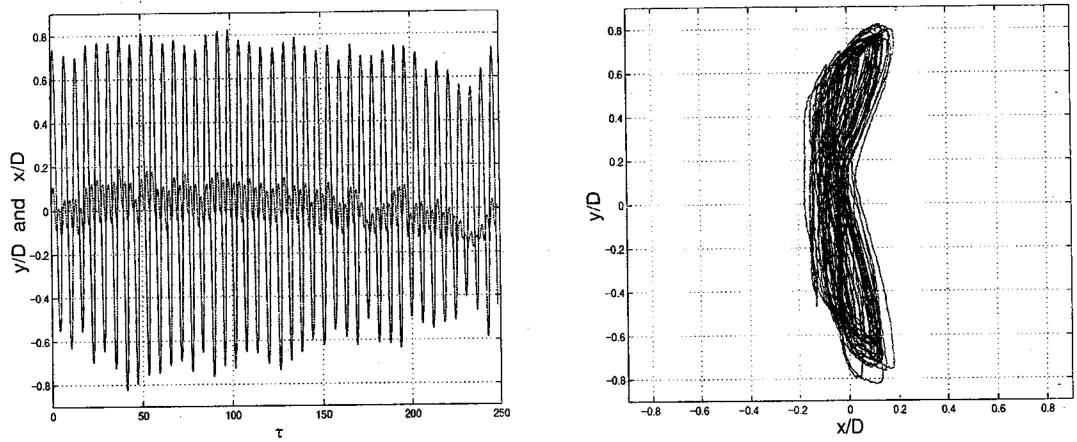

Figure 5.5 The *x(t)/D* and *y(t)/D* traces and the figure eight oscillation for *R2*, m^*=2.1, at *U*=0.97, flow is from left to right

5.3. *R1*, Two-Dimensional Oscillation, m^*=8.9

Case	m^*_y	m_y	k_y	f_{ny}	ζ_y	m^*_x	m_x	k_x	f_{nx}	ζ_x	D	*Re[10^3]*
R1	9.0	1.6	7.4	4.5	.032	5.57	.99	4.6	4.15	0.073	1	12-20

R1 involved a mass ratio of 8.9, similar to the mass ratios of *S7*, *R5* and *R10* studied before. The ratio of the elastic stiffness in *x* and *y*, k_x and k_y, was set equal to the ratio of the masses in those directions to achieve equal natural frequencies for each direction, $k_x/k_y = m_x/m_y$. This was mainly to achieve a system with one dominant natural frequency and to avoid a double resonant peak. The natural frequencies in *x* and *y* differed slightly in air due to their corresponding values of damping, but were very close in water (3.97Hz in *x*, 4.07Hz in *y*).

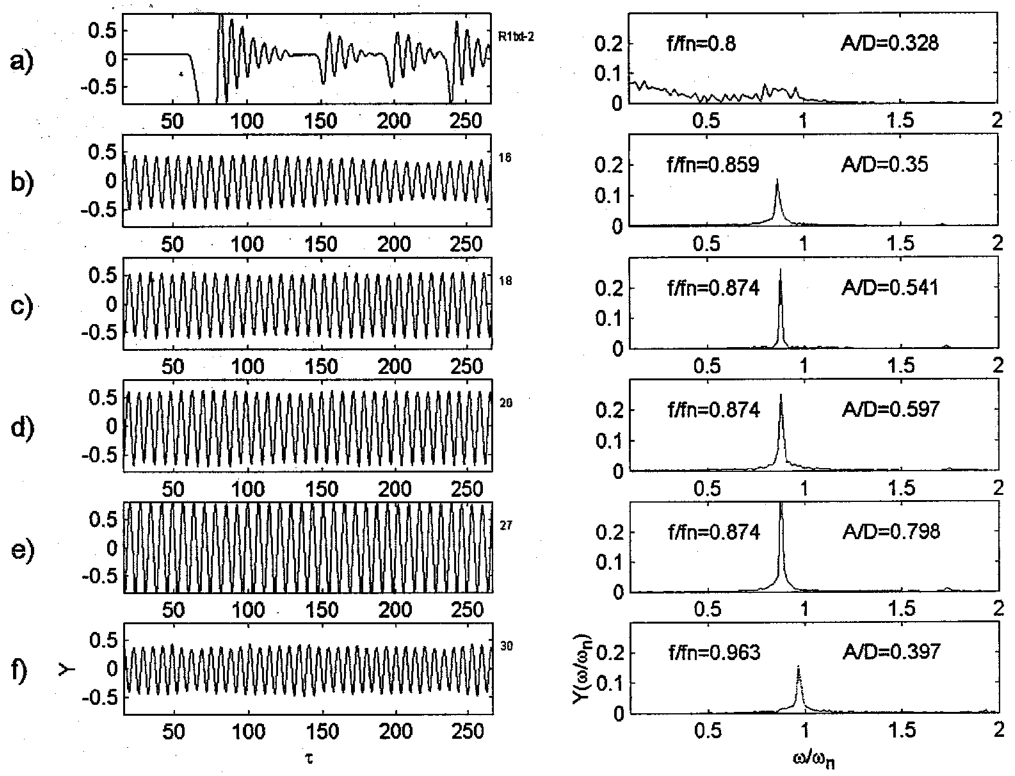

Figure 5.6 Oscillation traces and frequency spectra for case *R1*, m^*=8.9, at a) *U*=0.61, b) *U*=0.808, c) *U*=0.83, d) *U*=0.877, e) *U*=0.94, f) *U*=1.00

The amplitude response in this case is similar to that observed in *S7* with a larger maximum peak of *A/D*=0.88 at *U*=0.97; however, the frequency response is quite different from all cases studied up to the present in that it indicates a double partial lock-in. The frequency seems to lock to a value of *f*=3.87 Hz at 0.82<*U*<0.93 and with slight growth to *f*=4.3 Hz at 0.98<*U*<1.04. The temporary lock-in at 0.82<*U*<0.93 coincides with the continuous increase in amplitudes. The peak amplitude at *U*=0.97 appears to be unstable and achieved through the slow progression in the free stream velocities. Large amplitudes of oscillation are a common characteristic of two-dimensional oscillations as will be seen in cases *O1* and *O2*.

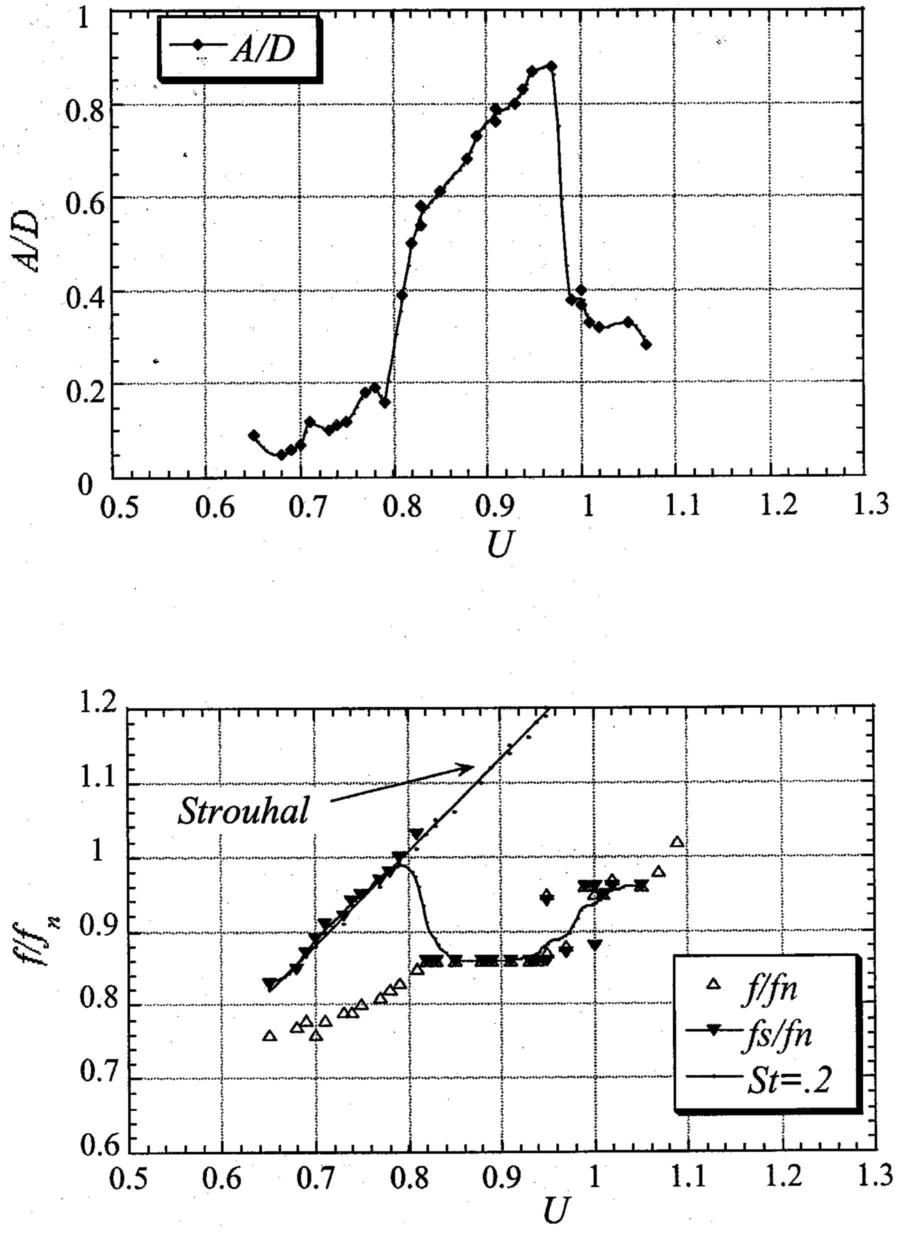

Figure 5.7 Oscillation amplitude and frequency response vs. U for $R1$, m^*=8.9

Without any vorticity field information, it is difficult to assess possible modes of shedding. Studying transient frequencies using *EMD* may reveal possible effects not captured here. Figure 5.8 displays the above behavior as a function of the effective stiffness k^*_{eff}. The partial lock-in is present as a large deviation from St=0.21 around

$-4<-k^*_{eff}<-2$. Similar to run *S1* in section 4.7, lock-in attenuates k^*_{eff} and clusters the data. This results in a smooth curve similar to most none-lock-in cases studied.

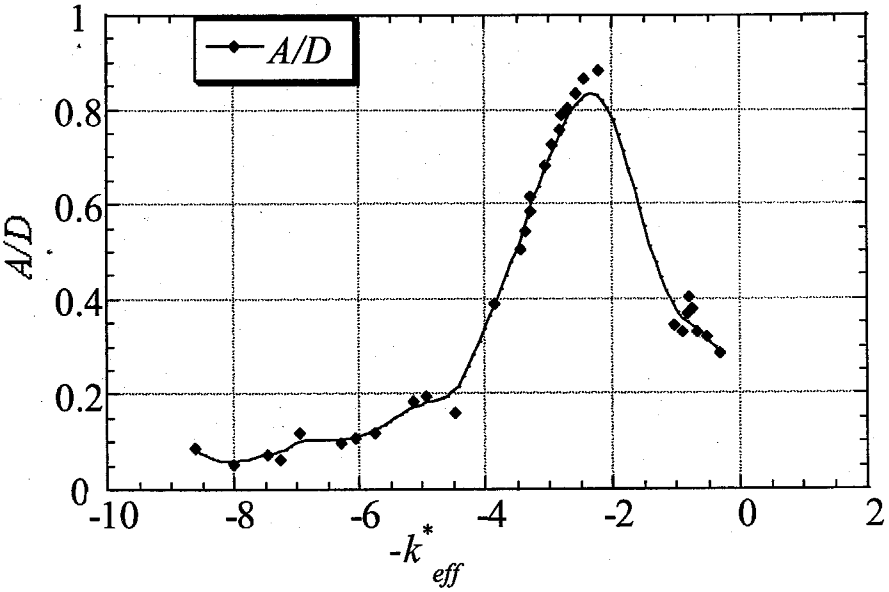

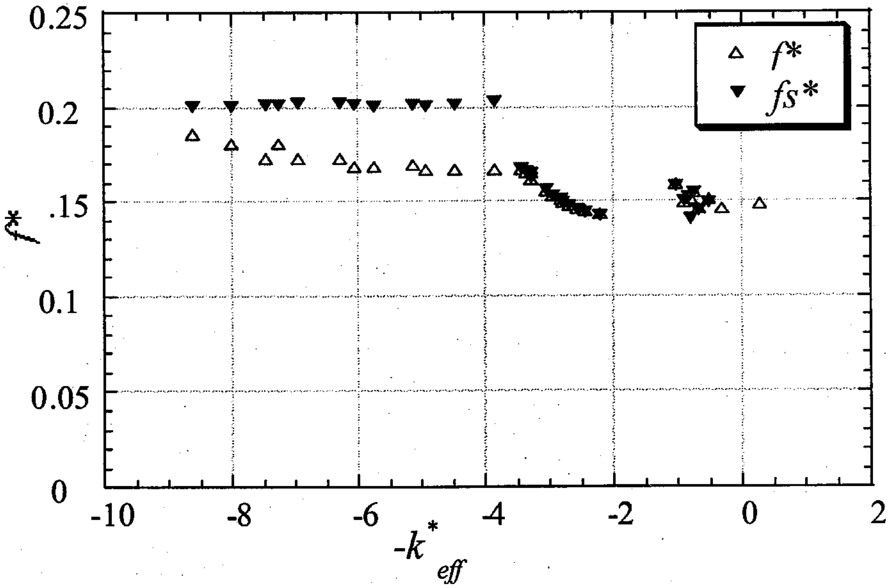

Figure 5.8 Oscillation amplitude and frequency vs. $-k^*_{eff}$ for *R1*, m^*=8.9

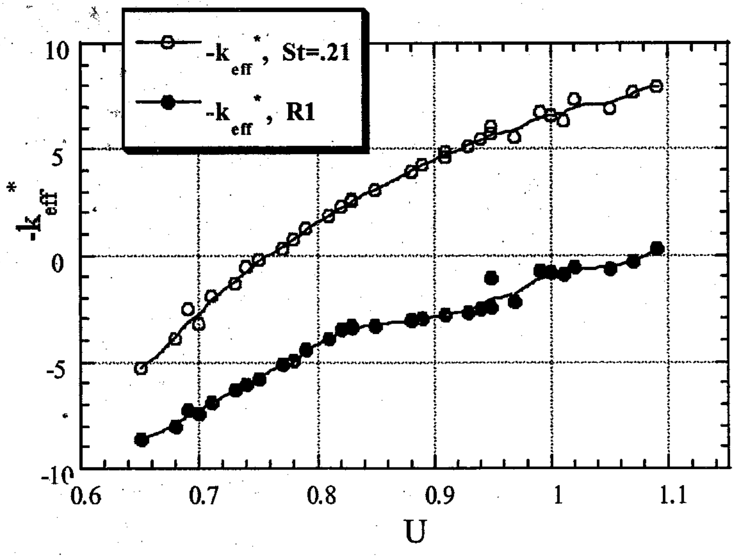

Figure 5.9 $-k^*_{eff}$ **vs.** U**, hollow circles assume nominal shedding with** $f^*=0.21$

Figure 5.9 shows how k^*_{eff} is modified due to the partial lock-in. Hollow circles assume frequency f^* held constant at 0.21 and the dark circles indicate how $-k^*_{eff}$ actually behaves with increasing U. The effective stiffness, k^*_{eff}, tends towards zero, $k^*_{eff}=0$, minimum which in return maximizes the possible amplitudes achieved.

5.4. Experimental Setup for *O1* and *O2* Tests

The principal goal of these experiments was to study vortex-induced vibration at very small values of mass ratio and damping. The unprecedented absence of lock-in in these cases led to further studies of this phenomenon at various values of mass ratio and damping with a goal to isolate the effects of degrees of freedom and the structural parameters.

The preliminary cases, *O1* and *O2,* used a simple free spring system along x and y as shown in Figure 5.11. The spring system and the Plexiglas frame holding the setup were within the tunnel boundary layer. The Plexiglas tubes were 22 inches long and were used with open ends 0.2 inch from the tunnel walls well within the wall boundary layer. The two-dimensional displacement traces were recorded using a Hi-8 camera and later analyzed frame by frame. The amplitudes are based on most frequent values deduced from video frames and the frequencies based on counting a large number of oscillations. The wake frequencies were probed using a hot-film anemometer located downstream of the cylinder within one of the shear layers and analyzed using an analog frequency analyzer. The *O1* experiment was conducted in the Student Tunnel and *O2* in the Noah tunnel at GALCIT. The Plexiglas tubes were filled with water to avoid buoyancy effects. The natural frequency in this setup depended on the tension in springs as well as the elastic stiffness of the springs used. The mechanical system, however, was non-linear due to large angles and extensions of the springs. During the tests, the equilibrium position of the cylinder shifted downstream depending on the average drag.

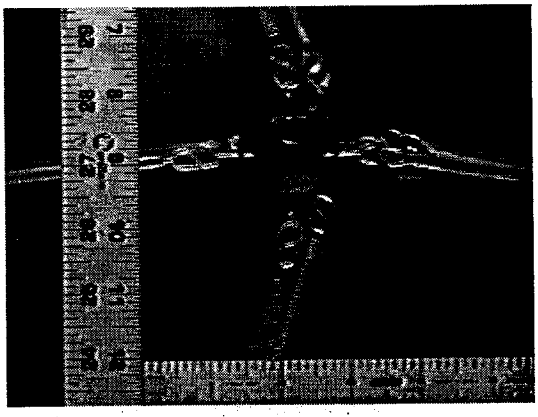

Figure 5.10 Detailed view of the cylinder setup

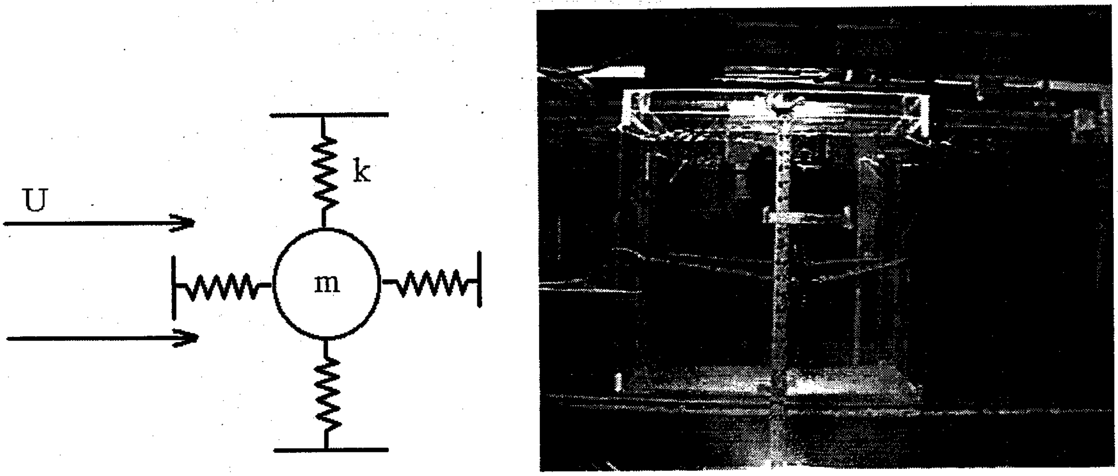

Figure 5.11 The experimental setup for cases *O1* and *O2*

5.5. *O1*, Two-Dimensional Free Oscillation, m^*=1.7

The frequency response in *O1* is very similar to the nominal shedding frequency of St=0.21. There is no evidence of lock-in and the low values of damping and the large amplitudes achieved are noteworthy. The data points in Figure 5.13 were not taken consecutively but rather with large velocity intervals in between. This experiment served as the first evidence of non-lock-in behavior with the possibility of oscillation amplitudes larger than a diameter (Figure 5.12).

Case	m^*	k_y	f_{ny}	ζ_y	k_x	f_{nx}	ζ_x	*D*	*Re*[10^3]
O1	1.73	2.6	2.1	.004	2.1	1.8	.003	1.25	7-14.6

The amplitude response (Figure 5.13) spreads over a wide range of free stream velocities, $0.35<U<1.2$. The frequency, unlike most cases studied, shows a nearly linear growth with U with small deviations from f^*=0.19.

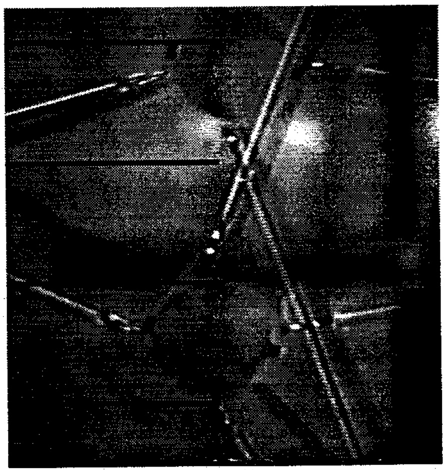

Figure 5.12 Oscillation amplitude above 1.0, t=0 and t=T/2 superimposed, U=1.28

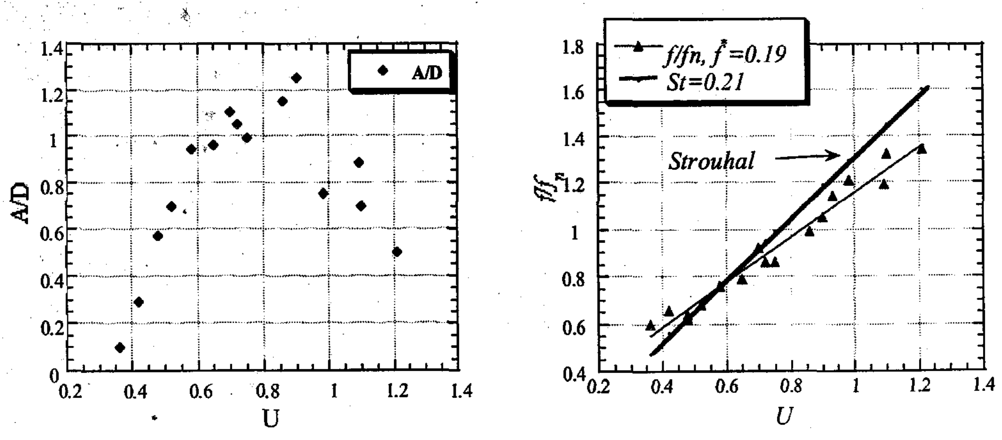

Figure 5.13 Oscillation amplitude and frequency response vs. *U* for *O1*, m^*=1.7

5.6. *O2*, Two-Dimensional Free Oscillation, m^*=1.7

The structural parameters were slightly different from the previous case as follows:

Case	m^*	k	f_{ny}	ζ_y	k_x	f_{nx}	ζ_x	D	Re[10^3]
O2	1.7	2.6	3.0	.004	2.6	3.0	.004	1 7/16	3-20

This case exhibits no lock-in behavior in y; however, it does exhibit a small range near U=0.15 where the stream-wise oscillations (along x) seem to lock to a frequency of f/f_n=1.15. The natural frequencies f_n= f_{nx}= f_{ny}=3.0 are measured in air as usual and U varies within the range 0.14<U<0.8. As seen in Figure 5.14, the system attains an amplitude of A/D=1 at U=0.5 and becomes unstable above U=0.65 as discussed later (see Figure 5.17). It is worth noting that using the natural frequency of the system in water (f_{nH2O}=1.3) to non-dimensionalize the parameters would place the velocity range to 0.31<U<1.8 with A/D=1 attained at U=1.11.

Figure 5.15 shows the steady frequency response with the brief inline lock-in around U=0.15 (oscillation frequency along y, f_y=f_x/2 is shown). The shedding frequency in this interval stays constant about f/f_s=0.25 while the oscillation frequency reflects a value of

f/f_n=0.5. Inline oscillation about U=1/4 and cross-stream oscillation about U=1/2 for a similar experimental setup have already been observed by King and Prosser [1972] and Tamura [1998].

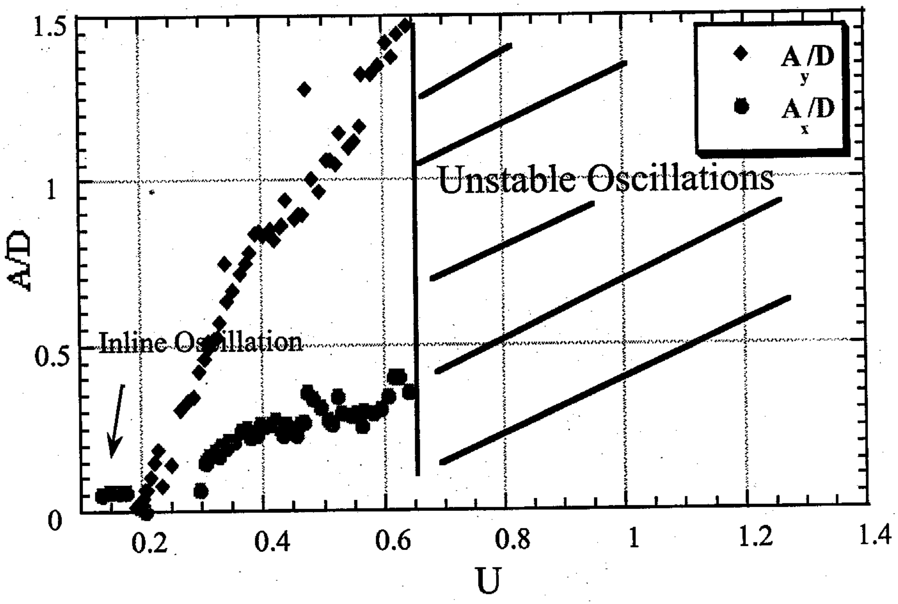

Figure 5.14 Oscillation amplitude vs. *U* for *O2*, m^*=1.7

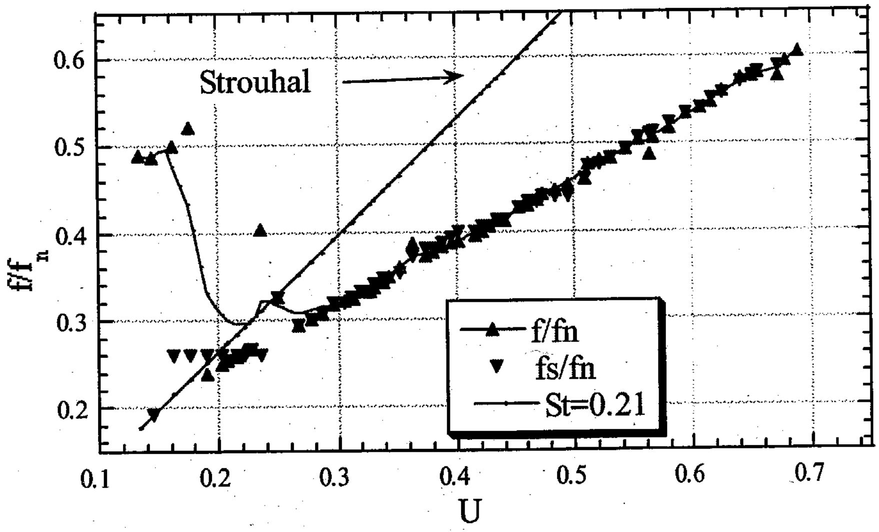

Figure 5.15 Frequency response vs. *U* for *O2*, m^*=1.7

Figure 5.16 shows the cylinder inline oscillation and Figure 5.19 shows the large amplitude figure eight motion of the cylinder at U=0.4. The fast cross-stream movements and the phase between the x and y motion are to be noted. The unstable oscillation depicted in Figure 5.17 involved three degrees of freedom including rotation around the stream-wise direction. The system mechanical energy would at times be transferred from one degree of freedom to another and at other times be present in all three degrees of freedom at the same time. The instability is due to the proximity of the rotational to translational natural frequency and the large range of possible *U*'s for *VIV*. Two modes of oscillation with wide ranges in *U* seem to have merged in this case.

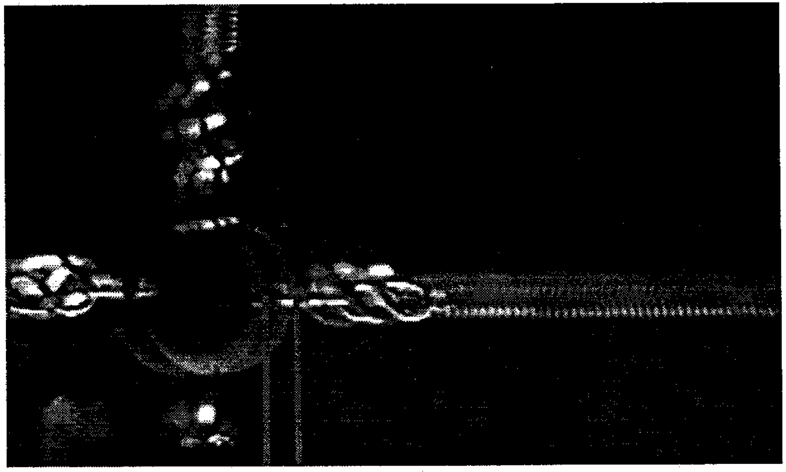

Figure 5.16 In-line oscillation

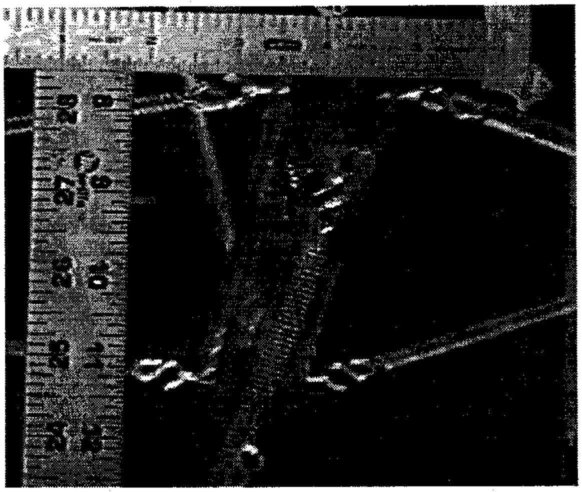

Figure 5.17 *U*nstable oscillations in rotational mode

5.7. Summary of Results

Two-dimensional oscillations involved large amplitudes not encountered in one-dimensional experiments. In the present studies, unprecedented oscillation amplitudes up to *A/D*=1.25 were observed. The common occurrence of figure eight oscillation in nature with such large possible amplitudes makes them a crucial part of *VIV* research.

Some of the results involving inline oscillation may be interpreted differently depending on whether the natural frequency in air or water is used to non-dimensionalize the parameters. Two experiments (cases *O1* and *O2*) involved unprecedented low values of mass ratio and damping. Systems with multiple degrees of freedom can allow multiple overlapping ranges of free stream velocities for *VIV*. Energy transfer between different modes can give rise large oscillation over a large range in *U*.

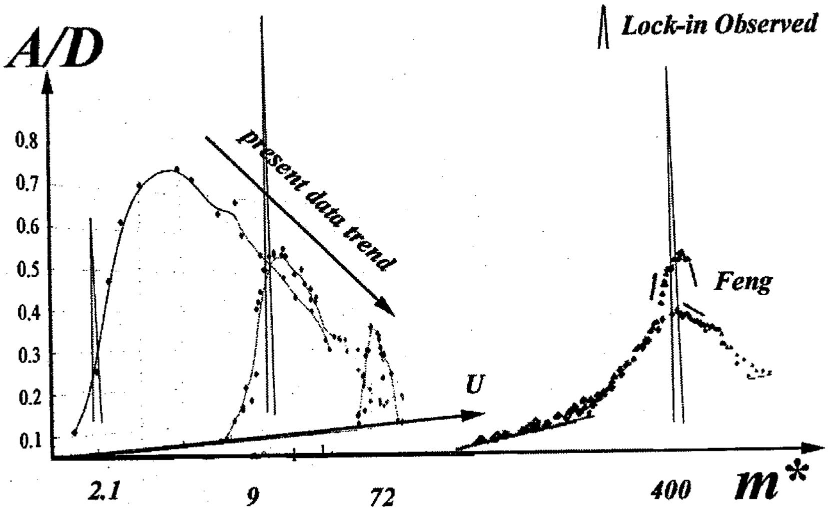

Figure 5.18 Lock-in encountered in very low to high mass ratios

Although most cases studied in this chapter did not exhibit lock-in and frequencies in general grew steadily with *U*, a partial lock-in in *y* (case *R1*) and a minor lock-in in the *x* direction (case *O2*) were observed. The existence of lock-in in these cases is very crucial for it proves that lock-in is not a necessarily a large mass ratio phenomenon. It is plausible that lock-in may occur at any mass ratio, but at small mass ratios, its presence is overshadowed by the new lock-in-free *VIV* mode. As stated in chapter 4, a low value of m^* and a lock-in behavior $(f/f_n{\sim}1)$ are two different manners in which $k^*_{eff}=(m^*/U^2)(1-(f/f_n)^2)$ may be minimized. The word mode is used here to emphasize the different physical process behind the observation; large fluid forces due to large due to fluid density vs. frequency locking.

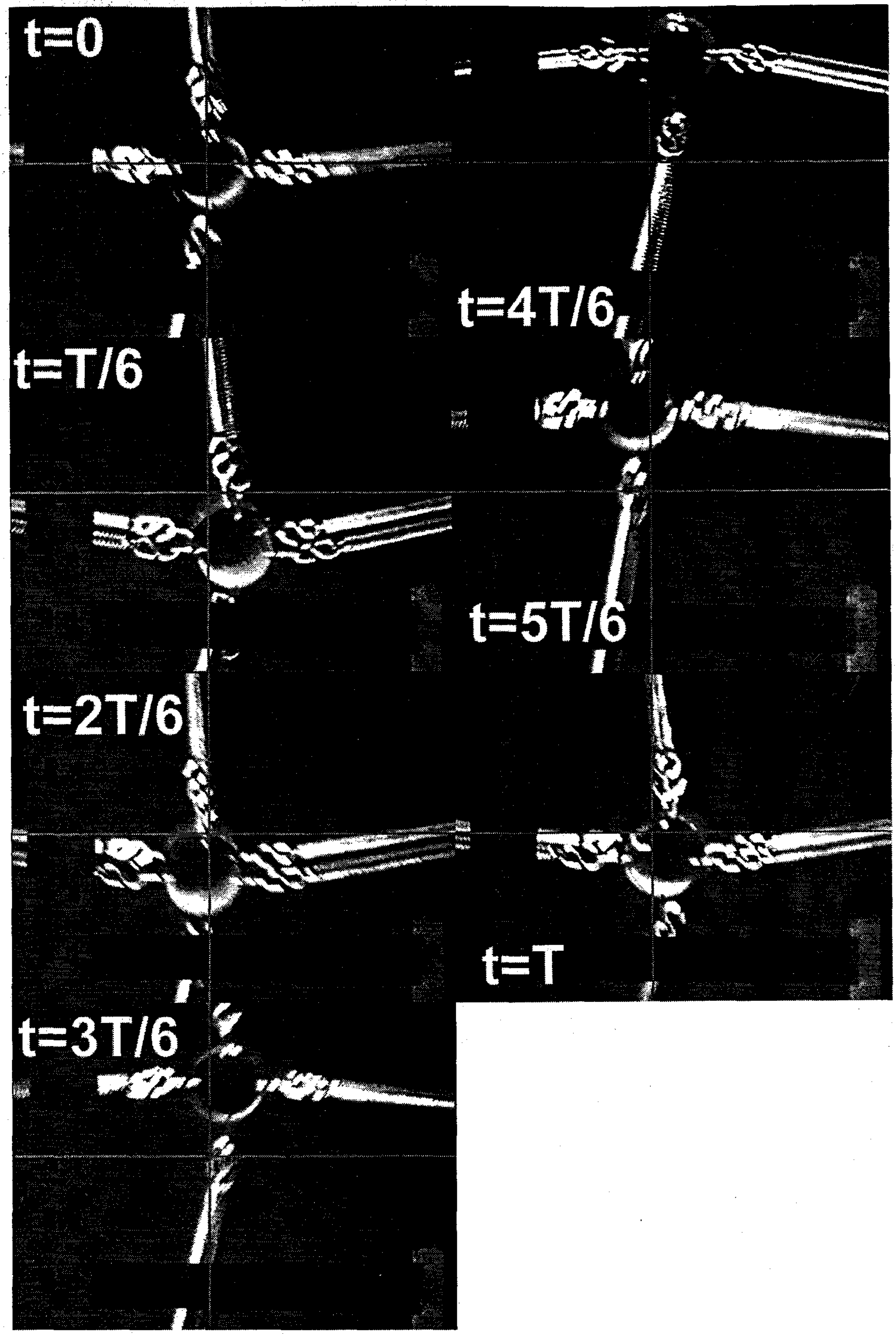

Figure 5.19 Oscillation trace for *O2* at *U*=0.4 and t=0, T/6, 2T/6, 3T/6, 4T/6, 5T/6, T

CHAPTER 6

Force Deduction

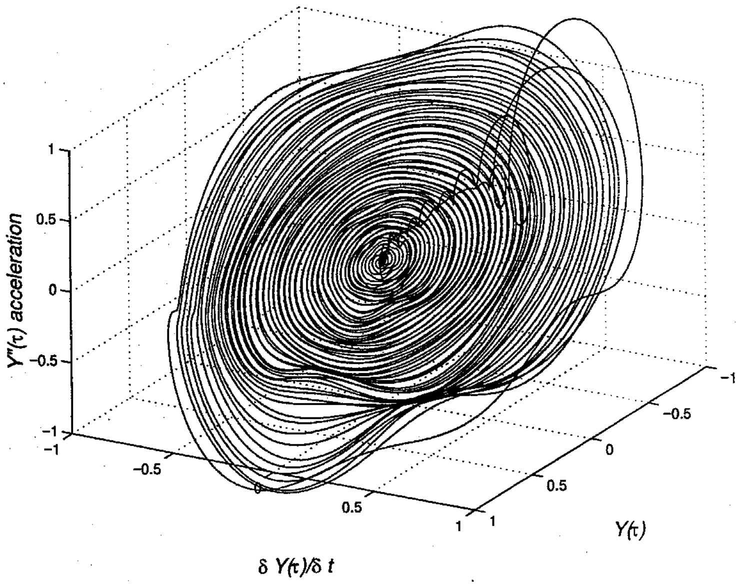

6. Force Deduction Technique

6.1. Introduction

Knowledge of the instantaneous fluid force can be helpful in understanding flow-induced vibration phenomena. The magnitude and the frequency content of the lift force, along with the time-dependent phase ϕ, can be of significant use in understanding some of the unpredictable behavior observed in the previous chapters. In chapters 4 and 5, larger *VIV* amplitudes were found in cases that involved larger values of mass ratio and/or damping. (e.g. cases *R2* in chapter 5 vs. *R3* in chapter 4). One possible explanation for this is a higher value of the lift coefficient $C_y(\tau)$ caused by different fluid-structure conditions. A knowledge of $C_y(\tau)$, especially the lift amplitude and frequency content could present a different view of the fluid state.

This chapter describes an experimental technique for deducing the unsteady fluid forces, $F(\tau)$, on elastically moving structures using their oscillation trace $y(\tau)$, and the free stream velocity U. The method does not involve a force balance or any knowledge of the flow field except for the free stream velocity U and can be applied to a strongly non-linear structure. With minimal extra setup, the method is highly suitable for experiments involving small mass ratios and multiple degrees of freedom as discussed in chapters 4 and 5. It is computationally fast and can be applied when other techniques are impossible.

In the following section, two other techniques for measuring the unsteady force coefficient and their specific limitations will be discussed and subsequently the new technique is introduced along with a few experimental challenges. Fourier transform, Wiener filtering and Empirical Mode Decomposition will be compared in search of an optimal method to obtain the end results.

6.2. Force Balance and Force-Vorticity Techniques

A force balance refers to a cantilever arm with a set of strain gauges, connected to a test model in the flow. The unsteady fluid forces on the test model are directly transmitted to the rigid cantilever cell causing a strain in the strain gauges. The signals from the strain gauges can be calibrated using known forces to deduce the unsteady force on the test model. A force balance can not be used on freely oscillating models unless it moves in rigid body translation with the body (Khalak and Williamson [1997]). Force balances involve considerable mass of a few pounds, not desirable in low mass ratio experiments, and can not be attached to structures with complex degrees of freedom. They also involve tedious calibration procedures.

Force-vorticity technique is a modern technique that involves mapping of the flow field around a body within a control volume via Digital Particle Image Velocimetry, *DPIV*, and employing a set of momentum integral equations to compute the integral fluid force on the body as function of time (Noca [1996]). This method is thorough for it contains time-dependent knowledge of the flow field velocity and vorticity. Two-dimensionality within the flow field greatly simplifies the application of this technique. This is generally the case in forced and free oscillation experiments. This method is quite experimentally involved and computationally laborious.

6.3. Force Deduction Using Oscillation Trace $y(\tau)$

The new force deduction technique involves an accurate modeling of the elastic structure as an ordinary differential equation and employing time-dependent oscillation traces, $y(\tau)$, to extract the lift coefficient $C_y(\tau)$ from a fluid-structure force balance equation such as the following:

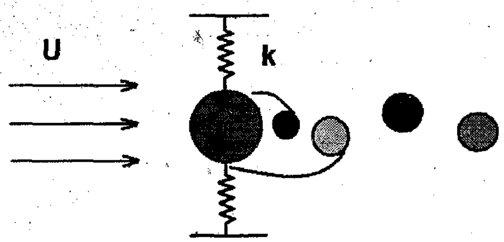

$$\frac{m^*}{U^2}(\ddot{Y}+2\xi\dot{Y}+Y)=C_y(\tau) \qquad \textbf{Equation 6.1}$$

Figure 6.1 Fluid structural model

where $Y(\tau)=y(\tau)/D$ is the non-dimensional displacement, $m^*=2m/\rho_f D^2$ the structural mass ratio, and $2\zeta=b/(km)^{1/2}$ the fraction of the critical damping and $U=U_\infty/\omega_n D$ the non-dimensional flow speed (chapter 2). The structural parameters ζ and ω_n are determined by fitting a free oscillation trace in vacuum to the appropriate dynamical equation of type

$$\ddot{Y}+2\xi\dot{Y}+Y=0 \qquad \textbf{Equation 6.2}$$

and the mass ratio m^* and the free stream velocity U can be measured independently. The displacement velocity, $\dot{Y}$, and acceleration, $\ddot{Y}$, can be obtained through successive numerical derivatives. Having obtained numerical values for all terms on the left-hand side of Equation 5.1, a numerical value for $C_y(\tau)$ is evaluated by substitution. This methodology, however, involves a few intricate points discussed in the following sections.

6.4. Practical Implications

Experimental problems are primarily noise in the captured signal $Y(\tau)$ and non-linearity within the elastic structure and displacement measuring devices. A free decay oscillation of the elastic structure can be used to model the system as a non-linear ordinary differential equation and a variety of filtering techniques can be applied to separate the noise from the signal. Since modeling the system requires numerical derivatives of $y(\tau)$, the proper filtering of the data becomes the most crucial issue. In the following two sections, the general methods for modeling the system and filtering the data will be discussed and details of each subject will subsequently be addressed.

6.5. Modeling the Structural System

A decay vibration, $Y(\tau)$, and its derivatives can be fitted to a nonlinear O.D.E. of the following form

$$\ddot{Y} + 2\zeta\dot{Y} + Y + kY^3 + b_n\dot{Y}\left|\dot{Y}\right|^n + c\,\mathrm{sgn}(\dot{Y}) + \ldots = 0$$ **Equation 6.3**

to obtain possible coefficients on the left-hand side. The kY^3 term represents the nonlinear spring stiffness, $b_n\dot{Y}\left|\dot{Y}\right|^n$ is the *nth* order "fluid-type" damping and $c\,\mathrm{sgn}(\dot{Y})$ stands for Coulomb friction. The displacement trace $Y(\tau)$ needs to be filtered before obtaining the higher derivatives. The need to assume a functional form for the non-linearity is a limitation of this approach.

One may, however, resort to a more general form of the above equation

$$\ddot{Y} + Z(Y, \dot{Y}) = 0$$ **Equation 6.4**

where Z represent a non-linear damping and stiffness term. Since the phase portrait for the free decayed oscillation involves a relatively large domain, numerical values for a continuous Z function may be obtained through interpolation and stored for various values of Y and $\dot{Y}$ (Figure 6.2). After studying various filtering techniques, the simple mass-damping model in **Equation 6.1** will be attempted. Higher order corrections will be made if necessary.

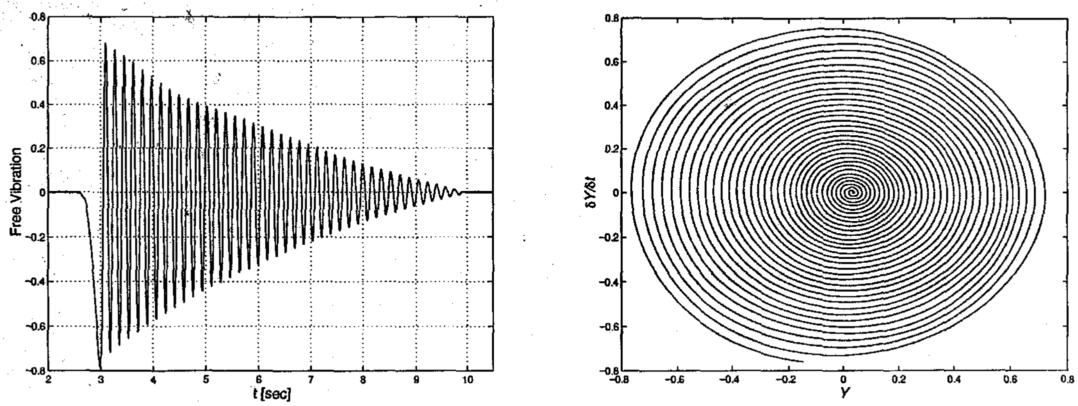

Figure 6.2 Free decay vibration trace *Y(t)*, phase portrait, $\dot{Y}$ vs. *Y*

6.6. Frequency Spectrum

5.1.1. *FFT* High Frequency Behavior

Figure 6.3 shows a trace from *S1* run at *U*=0.956 and the following parameters:

Case	m^*	ζ×100	*m* [kg]	*K* [lb/in]	f_n [Hz]	*D* [in]	*Re [10^3]*
S1	28.0	0.7	5.03	30	5.7	1	10-25

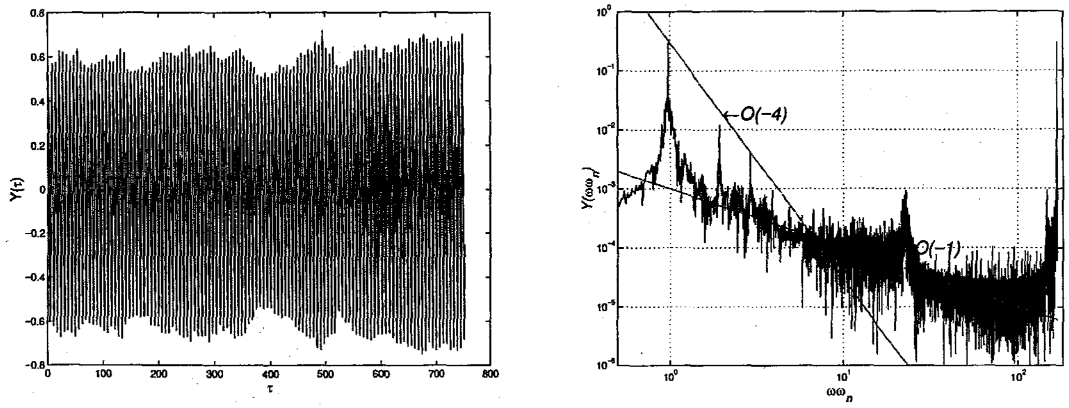

Figure 6.3 Oscillation trace and Frequency spectrum for *U*=0.956, *S1*, m^*=28

The frequency spectrum in Figure 6.3 shows the presence of a few harmonics of important magnitude, a large range of high frequency noise with a peak about ω/ω_n=22.5, (f=128 Hz) and a frequency tail of f/f_n^{-1} type decay. The noise peak may be related to the harmonic of the usual 60 Hz noise. The harmonics decay with $O(-5)$ power based on a line connecting the first and the second harmonics and $O(-4)$ by connecting the following two harmonics. A comparison with the frequency spectrum of a sine wave of same length, frequency, phase and equivalent amplitude in Figure 6.4 serves to show that the (f/f_n^{-1}) tail is a simple byproduct of the *FFT* technique. This $O(-1)$ tail arises from the periodicity assumption in Fourier transform and the discontinuous boundary conditions in the sample at hand.

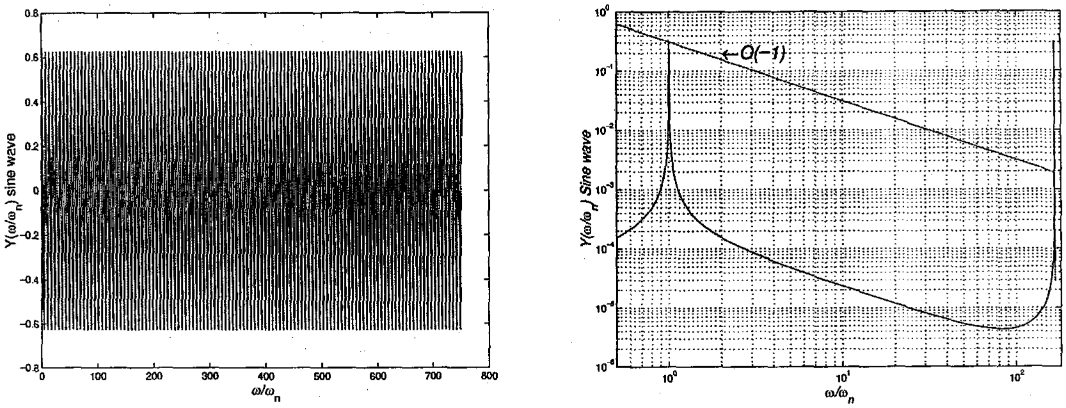

Figure 6.4 A sine wave of equal length, frequency and equivalent amplitude

The noise, the *FFT* tail, and the harmonics need to be separated in a definite manner. Taking two derivatives of $Y(\tau)$ is ideally equivalent to multiplying the frequency spectrum $Y(\omega/\omega_n)$ by a $(\omega/\omega_n)^2$, however, the existence of the nonphysical *FFT* tail precludes manipulation of data in frequency space. Derivatives can both amplify the high frequency noise or the higher harmonics.

6.6.1. Hann Window

Various windows such as Hann are usually used to create periodic signals with smooth boundary conditions to avoid the *FFT* tail mentioned above. Figure 6.5 shows the $Y(\tau)$ and its spectrum after applying a Hann window of $w_H=1/2[1-\cos(2\pi\, t/T)]=\sin^2(\pi\, t/T)$ to the data shown in Figure 6.3. Although Hann does not change the *O(-4)* rate of decay of the harmonics, it helps delineate two noise tails from the rapidly decaying signal base about $2<(\omega/\omega_n)<7$. The apparent *O(-1)* tail in Figure 6.3 is absent in Figure 6.5. The noise spectrum in the range $8<(\omega/\omega_n)<20$ is quite flat. The power spectrum, however, is reduced because of the window and requires appropriate correction. As shown in Figure 6.6, Hann window applied to a pure sine wave reduces the tail observed in Figure 6.4 from *O(-1)* to only about *O(-4)*. This is another indication that the main signal within the displacement trace in Figure 6.5 may in fact be decaying faster than *O(-4)*.

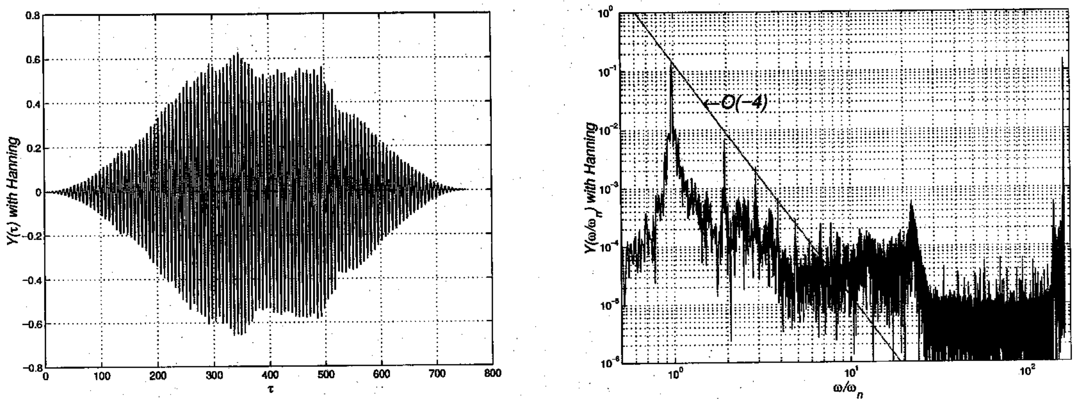

Figure 6.5 A Hann window to create a periodic signal

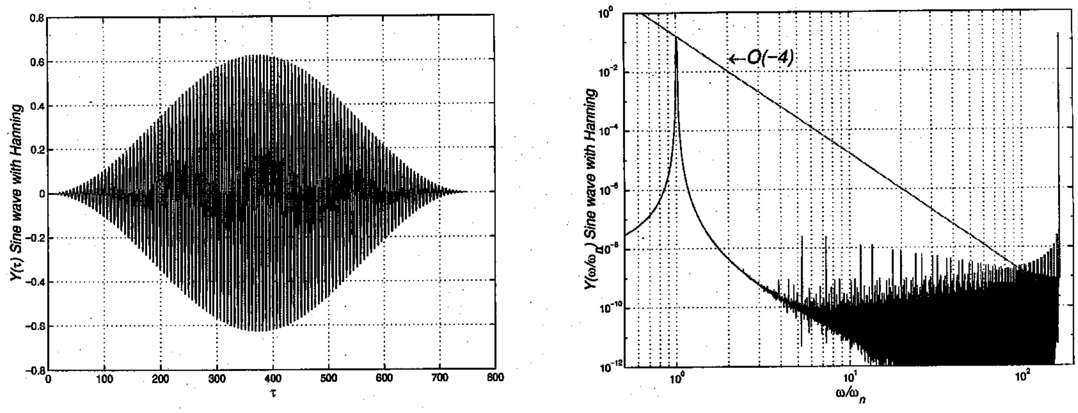

Figure 6.6 Hann window on a sine wave and a $(f/f_n)^{-4}$ decay tail

6.6.2. Smooth Boundary Truncation

As an alternative to Hann, the trace can be truncated at its local minima near the boundaries. The trace is also raised by an appropriate amount so that it smoothly increases from zero to the original trace and reduces to zero at the end. The results are very similar to that of a Hann window without the large power loss (Figure 6.7). A reference line with *O(-5)* decay is used to denote the decay from the fundamental frequency to the second harmonic and to note that the main signal most probably lies within the *O(-5)* pyramid. In Figure 6.8, a short segment of the original signal with a few oscillations of about 1024 points is truncated in the same manner to obtain the same results as in Figure 6.7 with less resolution in the power spectrum. This is mainly to achieve a less crowded spectrum with more clear harmonics. The frequency peak, however, is shifted f/f_n=1.12. This is mainly due to the quasi-periodicity within the signal and serves to show yet another limitation of the *FFT* averaged estimates of the frequency.

For simplicity, a Hann window is used in all spectra presented in the following sections.

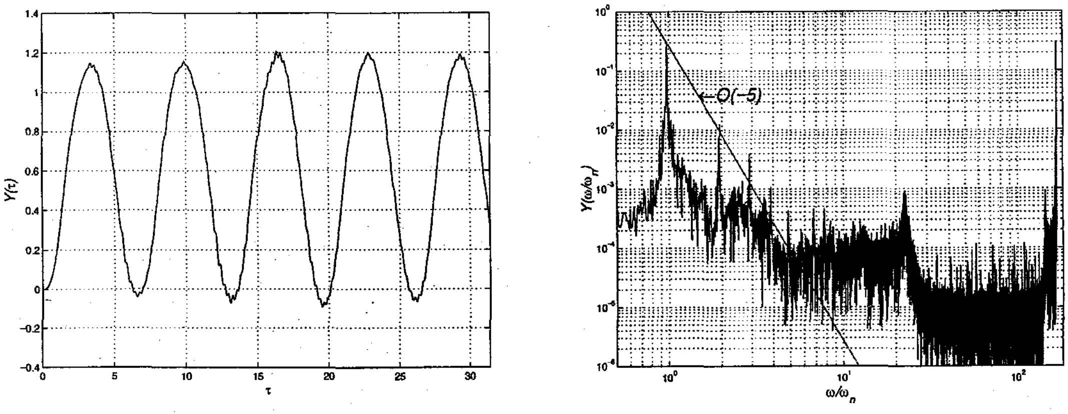

Figure 6.7 The original trace smoothly truncated at ends

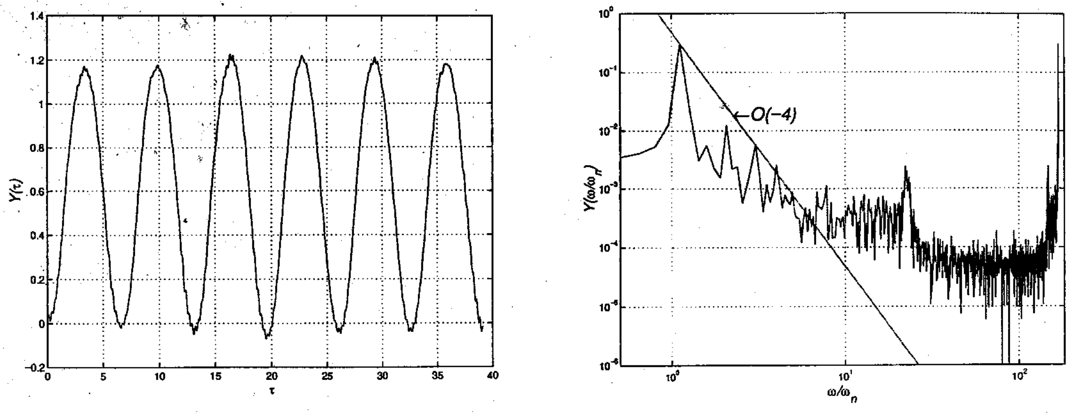

Figure 6.8 A short segment of the original trace smoothly truncated

6.6.3. Computing the Acceleration $\ddot{Y}$ (τ)

Figure 6.9 shows the second derivative of the displacement signal with its *FFT* spectrum after application of a Hann window. The first few harmonics decay like *O(-2)* as expected and the high frequency noise is amplified to dominance. The noise displays a growth in frequency with a positive ramp of about *O(2)*. In the next few sections, different filtering techniques will be examined in search of an appropriate one for the purpose of this chapter.

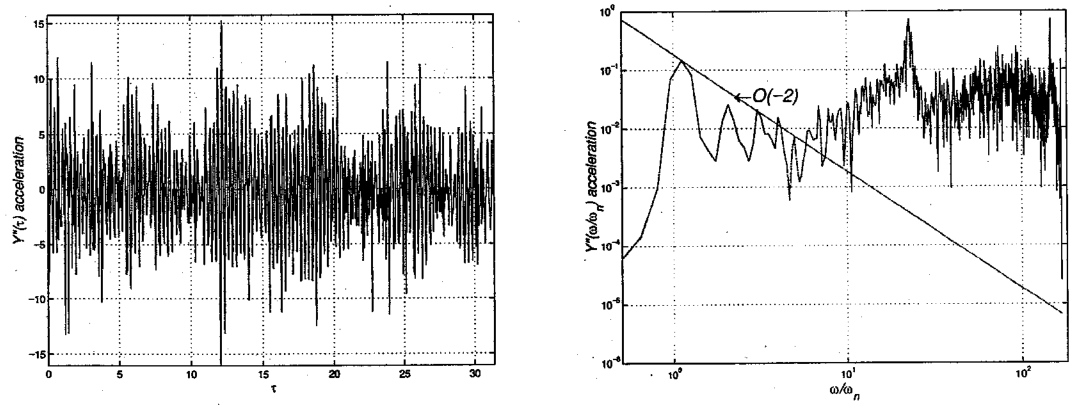

Figure 6.9 Acceleration trace $\ddot{Y}$ (τ) and the spectrum, $\ddot{Y}$ (ω/ω_n)

6.7. Filtering Techniques

Simple filtering techniques require a cutoff frequency that may be difficult to choose. From $Y(\omega/\omega_n)$ spectrum, the first two harmonics seem to be substantial in obtaining correct values of $\ddot{Y}$, however, the exact rate of harmonic decay is not known. This is mainly due to the large amount of high frequency noise and the *FFT* tail that even Hann could not completely remove. Since analytically, the harmonics of a periodic square wave decay like $O(\omega/\omega_n)^{-1}$ and those of a periodic triangular wave with discontinuous derivatives decay like $O(\omega/\omega_n)^{-2}$, it is clear that the harmonics of the trace at hand with discontinuous second derivatives will decay faster than $O(\omega/\omega_n)^{-2}$. The *FFT* spectrum of the trace (Figure 6.3) shows a harmonic decay of at least $O(-4)$. It is plausible that the main signal lies upon a tail due to noise or the *FFT* complications and that the actual harmonic decay is even faster than that observed between the fundamental and the second harmonic ($O(-5)$). Such fast decay would minimize the contribution due to higher harmonics in the acceleration. In the following subsections, an attempt will be made to find an appropriate filtering technique for separating the noise and the signal.

6.7.1. Butterworth Filter

Butterworth filter provides the best Taylor Series approximation to the ideal low pass filter response at $\omega=0$ and $\omega=\infty$. For any order *N*, the magnitude squared response has $2N-1$ zeros derivatives at these locations. In other words, Butterworth involves a magnitude response that is maximally flat in the passband and monotonic overall (maximally flat at $\omega=0$ and $\omega=\infty$). Butterworth filters sacrifice rolloff steepness for monotonicity in the pass and the stopbands (Figure 6.10). Unless the Butterworth's smoothness is needed, an elliptic or Chevyshev filter can generally provide steeper rolloff characteristics with a lower filter order.

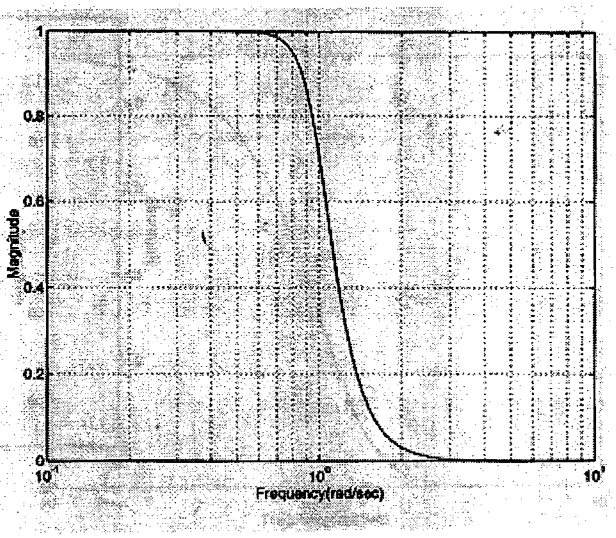

Figure 6.10 Butterworth frequency response curve

Figure 6.11 shows $Y(\tau)$ before and after a 5th order Butterworth filter and its *FFT* spectrum with a cutoff at ω/ω_n=5.5 to exclude the sixth harmonic. The tail is the result of the Butterworth, *FFT* and Hann schemes. Figure 6.12 shows the original displacement trace $Y(\tau)$ and the deduced acceleration after filtering $Y(\tau)$. The acceleration in Figure 6.12, obtained from the filtered data, shows strong evidence of the 2nd and the 3rd harmonics.

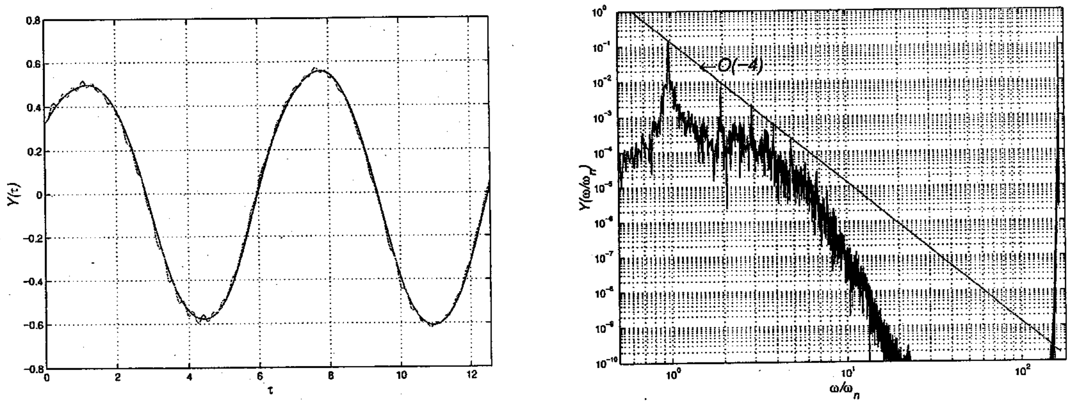

Figure 6.11 Displacement trace $Y(\tau)$ after a 5th order Butterworth filter with f_c/f_n=5.5 and the second derivative of the filtered data

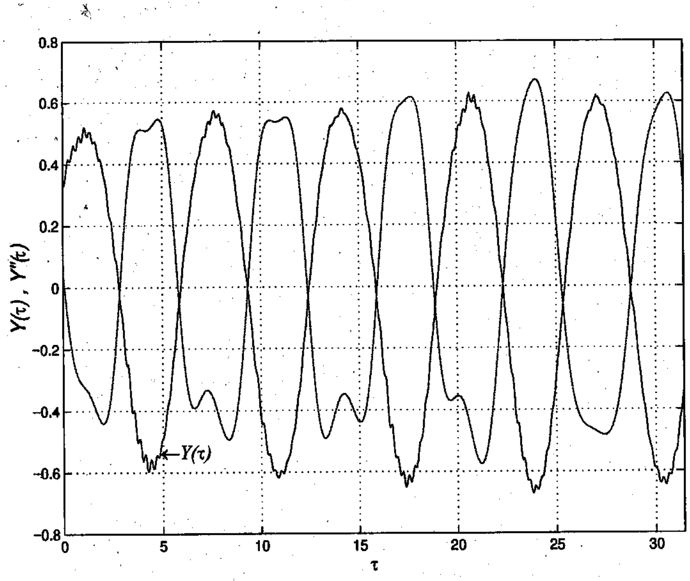

Figure 6.12 Original $Y(\tau)$ trace and $\ddot{Y}(\tau)$ obtained from the filtered trace

6.7.2. Sharp Frequency Cutoff

An ad hoc approach for filtering the data is to obtain the acceleration spectrum without filtering and to truncate it at some point before the noise ramp. In Figure 6.13, a line with an order *O(-3)* decay connects the main peak to the second harmonic. The noise ramp encountered about $\omega/\omega_n=10$ intercepts the above line at $4.5<\omega/\omega_n<6$. The Fourier transform is then set to zero for all frequencies above $\omega/\omega_n=5.5$ and the inverse transform used to obtain the acceleration. The resulting signal can be compared with the raw acceleration trace in Figure 6.9.

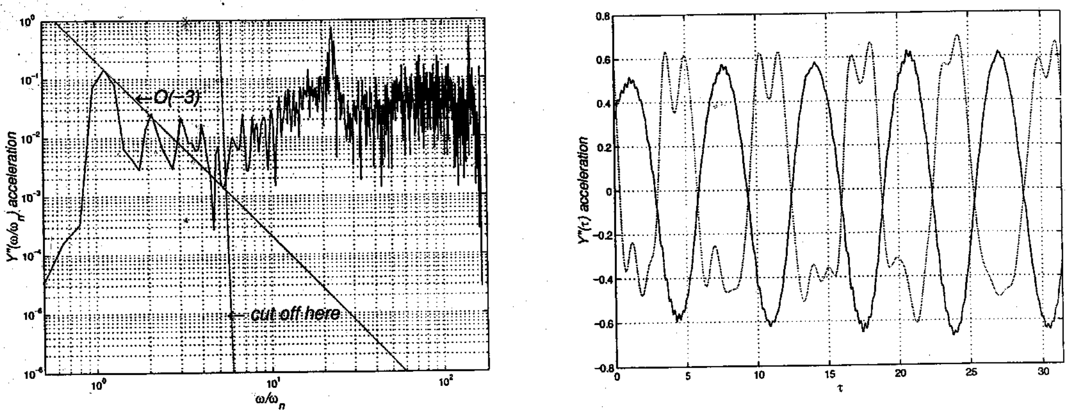

Figure 6.13 Acceleration spectrum, left, and $Y(\tau)$ and $\ddot{Y}(\tau)$ on the right.

6.7.3. Wiener Filter

Wiener filter is a simple technique for removing uncorrelated noise tails from experimental signals. When the power spectrum of the signal plus noise shows a distinct signal peak added to a noise tail, the tail is extrapolated into the signal peak as a noise model. The model does not have to be accurate for the method to be helpful. Subtracting the noise from the whole trace can produce a signal model. A simple algebraic combination of the noise and the signal models is usually used to create the optimum (or Wiener) filter.

The Wiener filter fails to improve the signal in this case (Figure 6.15). Although the noise is uncorrelated in this case, it is difficult to create a signal or noise model effectively. The noise in Figure 6.14 is modeled as a straight line and continued through the main signal. This actual noise spectrum involves large amplitude variations and hence subtracting the noise model (straight line) reduces the noise level by less than one order of magnitude.

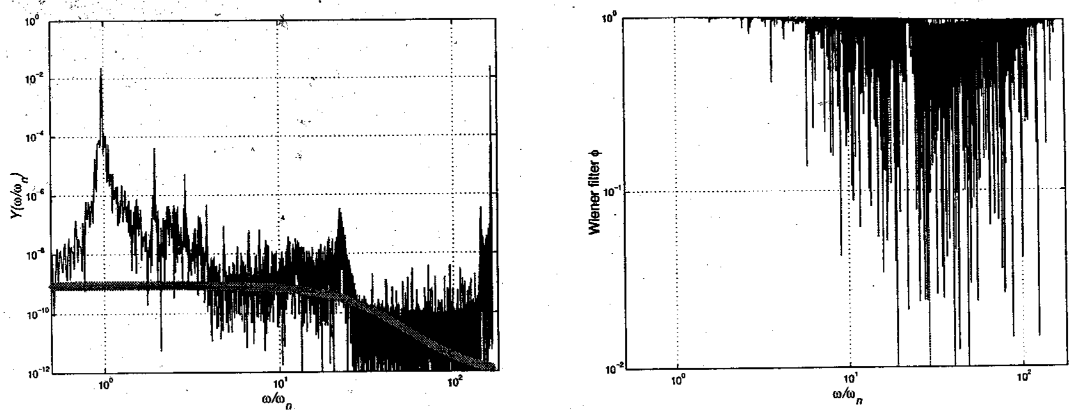

Figure 6.14 The power spectrum and the noise model

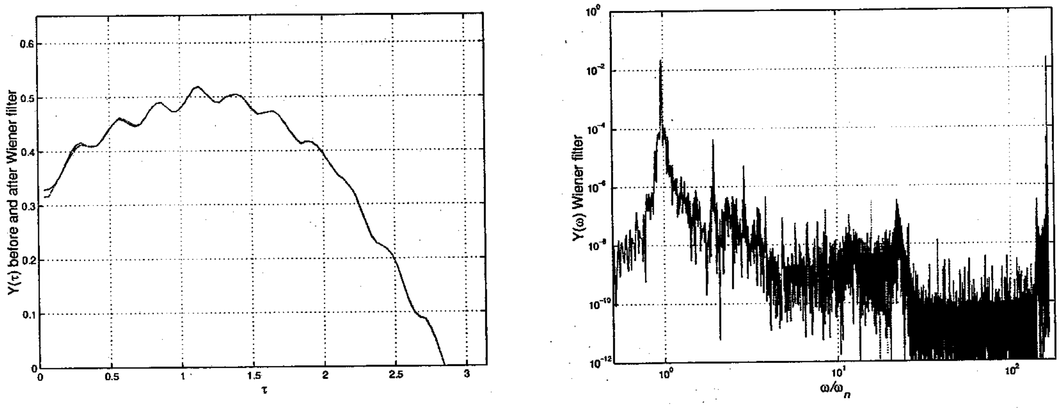

Figure 6.15 Displace trace and power spectrum after Wiener filter

6.7.4. Empirical Mode Decomposition (*EMD*)

Empirical Mode Decomposition (Huang [1998]) is a new technique for extracting modes with different frequency scales from a given experimental data (section 2.8). It employs a sifting technique connecting the local extrema or alternatively the inflection points within a trace as a means of defining the instantaneous frequency scales and through successive iterations extracts components with different frequency ranges.

It is possible to use *EMD* to extract high frequency components from the displacement trace at hand. Applying *EMD* produces the modes shown Figure 6.16. The first three rows, c1 to c3, are what seems to be high frequency noise components (note scales). The main signal components, c4 to c10, seem to indicate the presence of the shedding and structural frequencies. The two traces in c4 and c5 have the largest magnitudes and contain two different frequency ranges. The curve at the bottom, c11, indicates a small moving average. It is worth noting that the large frequency difference between the high frequency noise (rows c1 to c3) and the main signal (rows c4-c11). The are no harmonics present here. Assuming rows 1 to 3 as either noise or extraneous signals, we proceed to subtract them from the raw signal.

Figure 6.17 shows the Poincare map of the raw and the filtered signal. The displacement trace *Y(τ)* is plotted vs. *Y(τ+π/2)*. The main noise component here seems to be the ω/ω_n=22.5 peak mentioned before. The tiny wobbles in the Poincare map compared to the large loop indicate the large difference in frequencies. The flattened circular shape of the Poincare maps is due to the non-linearity within the signals. An *FFT* routine exhibits such non-linearity as harmonics.

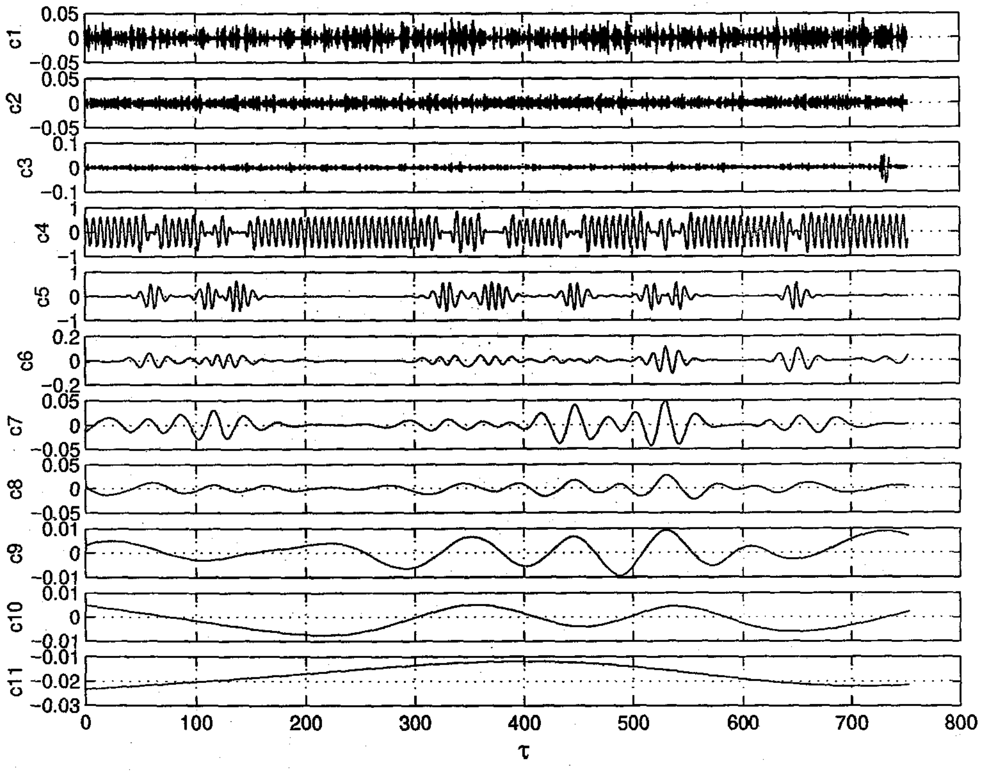

Figure 6.16 *Y(τ)* and the *EMD* components with the displacement signal *Y(τ)*

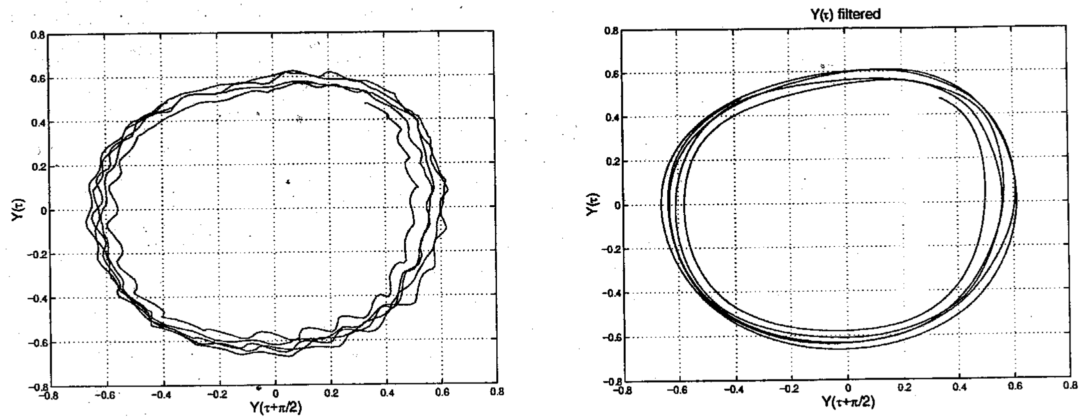

Figure 6.17 Poincare map of the *Y(τ)* with and without the high frequency *EMD* components

Figure 6.18 shows the frequency content of the noise subtracted and that of the remaining signal. Although the main harmonics seem to be well captured within the signal, there is still a considerable amount of noise present between the second and the tenth harmonic shown.

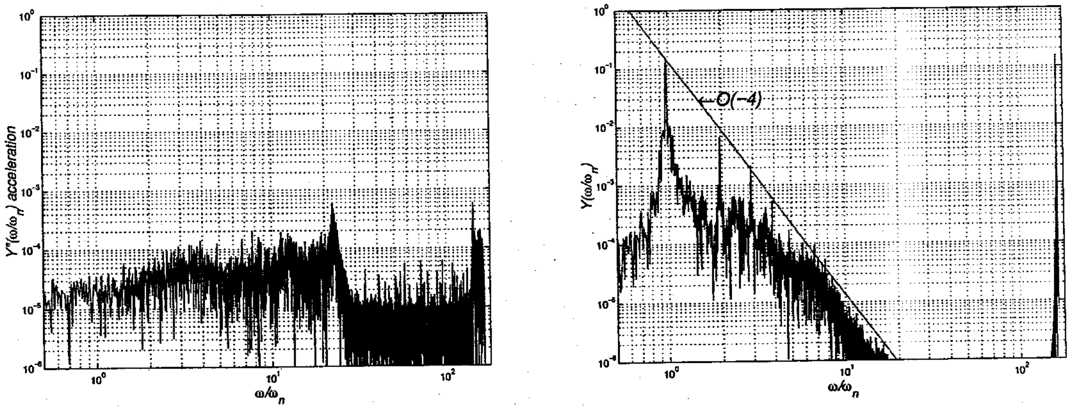

Figure 6.18 The frequency spectra for the *EMD* noise and the remaining signal

Figure 6.19 shows the *EMD* filtered signal *Y(τ)* and its second derivative. The acceleration term shows a more discontinuities than what we obtained using the simple Butterworth filter. We will look more closely at the signal to extract more noise components.

The acceleration is analyzed using *EMD* once again in Figure 6.20. Figure 6.21 shows details of the first eight modes. It is not yet possible to make a valid judgement about the third and the fourth modes. Modes 1 and 2 are however subtracted as noise and intermittency. Figure 6.22 shows the new acceleration trace and the displacement $Y(\tau)$ for reference.

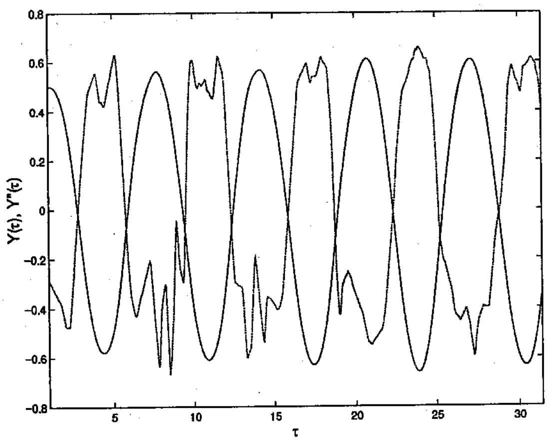

Figure 6.19 The *EMD* filtered oscillation trace $Y(\tau)$ and its second derivative

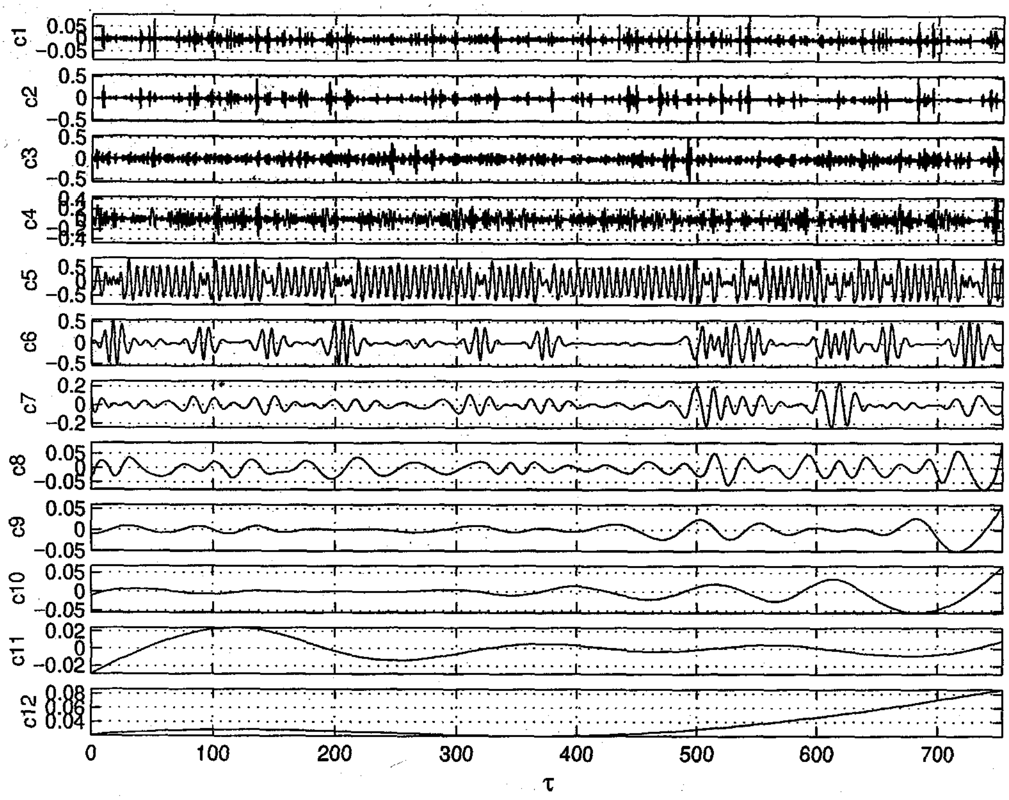

Figure 6.20 *EMD* components of the acceleration trace

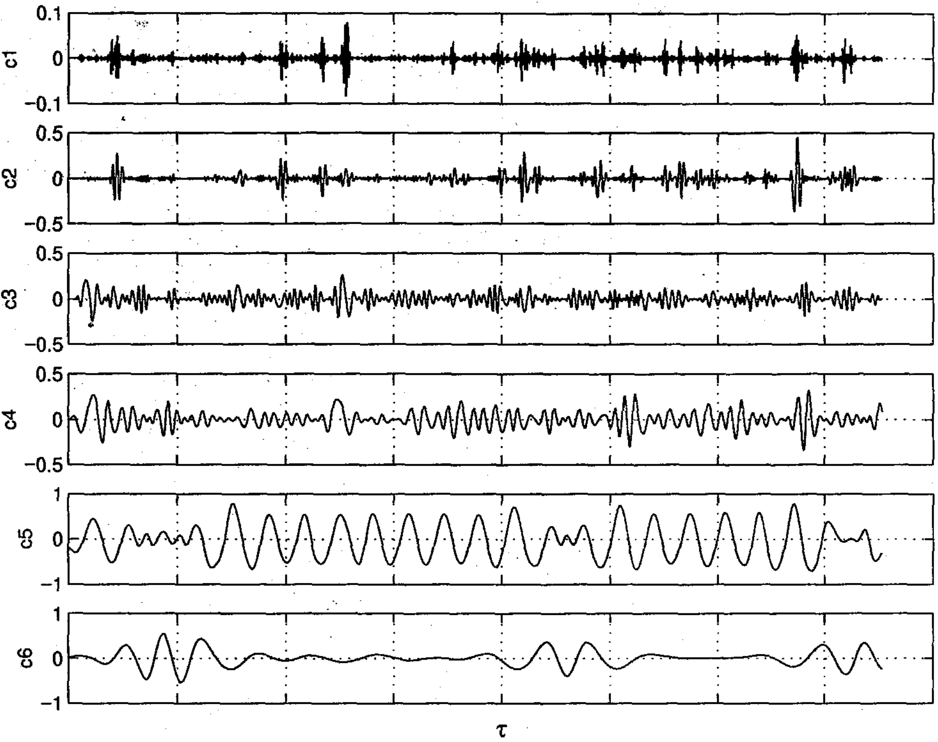

Figure 6.21 Detailed view of the first six modes

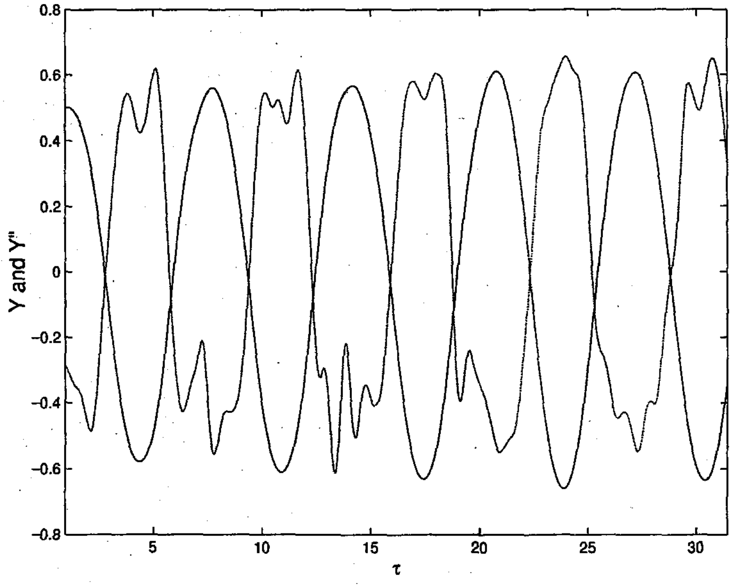

Figure 6.22 The *EMD* filtered oscillation trace $Y(\tau)$ and the filtered acceleration

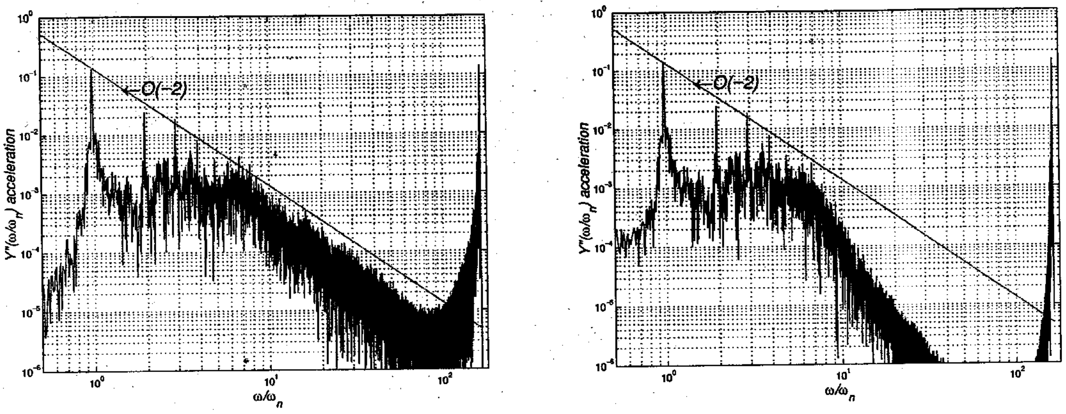

Figure 6.23 Acceleration spectrum before and after *EMD* filtering

Figure 6.23 shows the frequency content of the acceleration before and after subtracting the first two modes. Comparing the two figures, the two modes removed appear to have a large high frequency content about ω/ω_n=10. Figure 6.24 shows the raw displacement trace *Y(τ)* and the deduced acceleration after subtracting the third *EMD* component in acceleration.

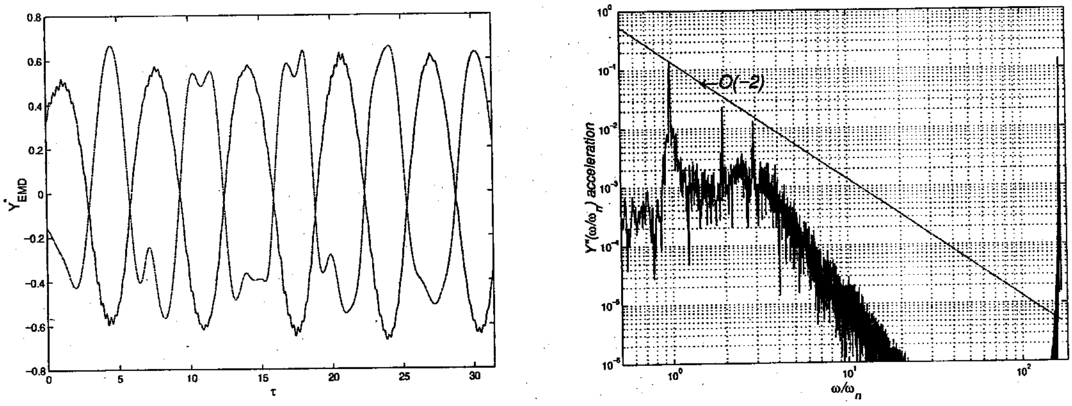

Figure 6.24 Deduced acceleration and the raw displacement *Y(τ)*

6.8. An Optimum Filtering Method

The acceleration traces in Figure 6.13, Figure 6.12, and Figure 6.22 appear to indicate a convergence in amplitude and frequency content. As indicated in 5.6.2, the application of Hann on a discrete sine wave leads to a frequency tail of only $O(-4)$. This and the $O(-5)$ decay tail connecting the first two harmonic peaks of the spectrum indicate that the harmonics of main signal within the trace may decay like $O(-4)$ or faster and that they may not be as crucial beyond the fifth harmonic. The *EMD* approach, on the other hand, replaced the idea of harmonics with a new view of a non-linear signal affected by different sources of noise. A sharp frequency cut off $f/f_n=5.5$ eliminating the 6th and higher harmonics seems to be a safe limit and will be used in the following sections.

6.9. Free Decay Oscillation in Air and Modeling a Dynamic Equation

Figure 6.25 shows a free decay oscillation trace of the structure used in case *S1*. The cylinder was replaced by a small piece of lead of the same mass. The trace is quite smooth with many oscillations; an indication of the small damping coefficient present. Using the conventional linear formula for damping:

$$\zeta = -1/(2\pi n)\ ln(P_n/P_1) \qquad \textbf{Equation 6.5}$$

where P_1 and P_n are $Y(\tau)$ at the first and the nth peak under consideration, gives

$$0.0065<\zeta<0.012$$

depending on the number peaks selected. The frequency peak before non-dimesionalization is at $\omega_n=5.7$ Hz and the spectrum in Figure 6.25 shows a harmonic decay of order $O(-6)$ between the fundamental and the second harmonic. The trace considered has non-oscillatory ($y=0$) segments contaminating the spectrum and hence is truncated so that it represents oscillation amplitudes with $0.1<A/D<0.5$ most commonly present in the *VIV* experiments (Figure 6.26). The final damping parameter is slightly sensitive to the exact truncation point, however damping plays a less important role in computing the lift coefficient $C_y(\tau)$ than the natural frequency f_n. The frequency spectrum of the truncated trace shows a sharper decay of order $O(-7)$ and a natural frequency of f_n=5.95 Hz. After rescaling the trace according to the new natural frequency, the acceleration trace in Figure 6.27 and its frequency spectrum are obtained.

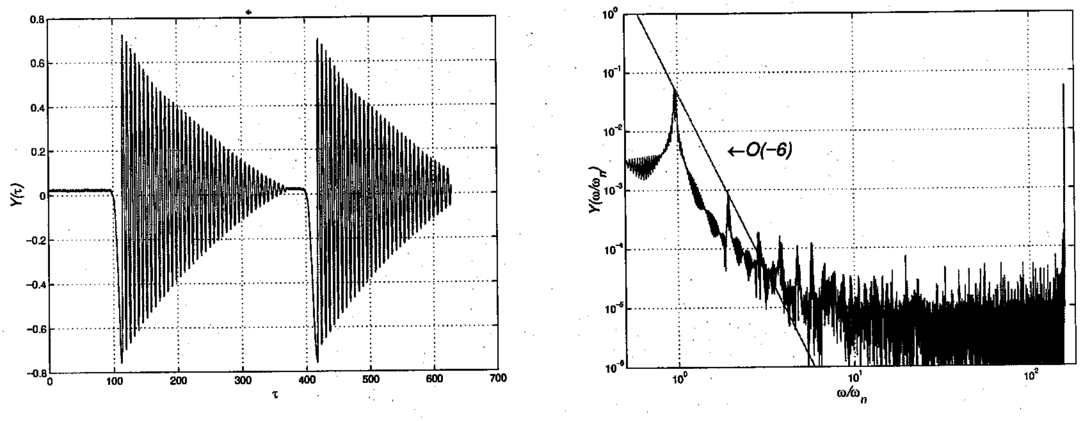

Figure 6.25 Free vibration in air

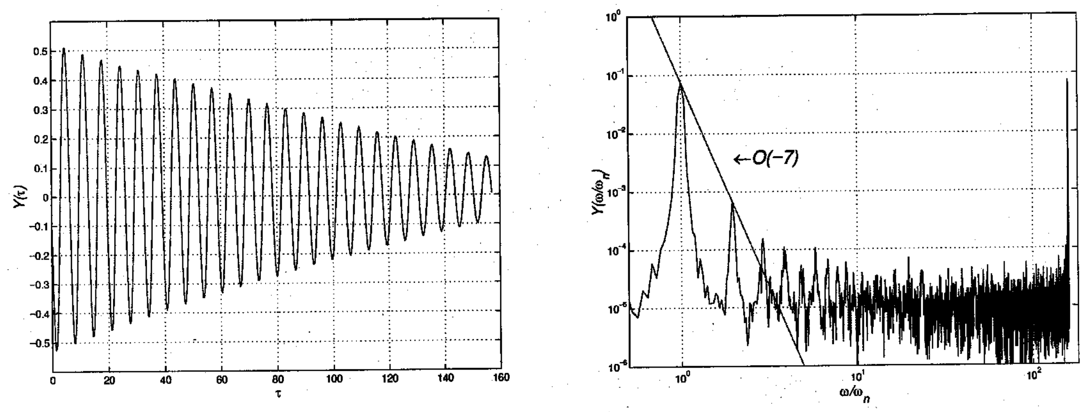

Figure 6.26 Truncated free vibration of the system in air

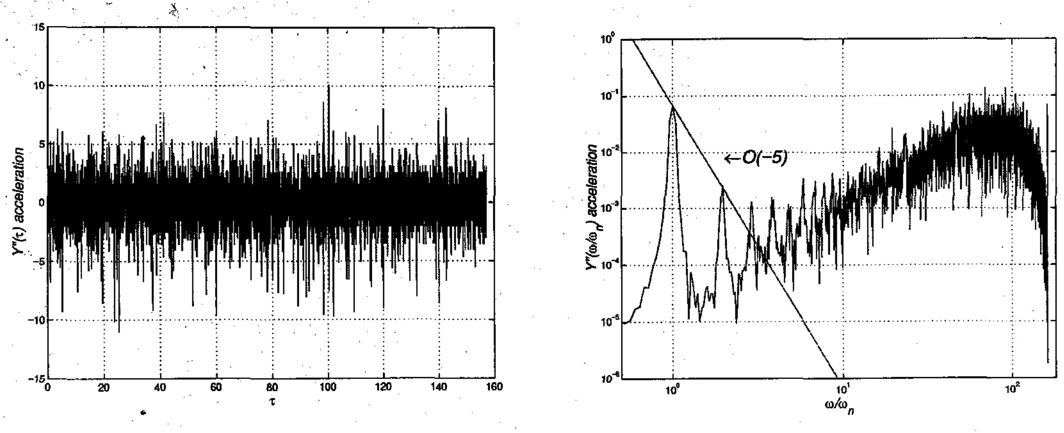

Figure 6.27 Free decay acceleration

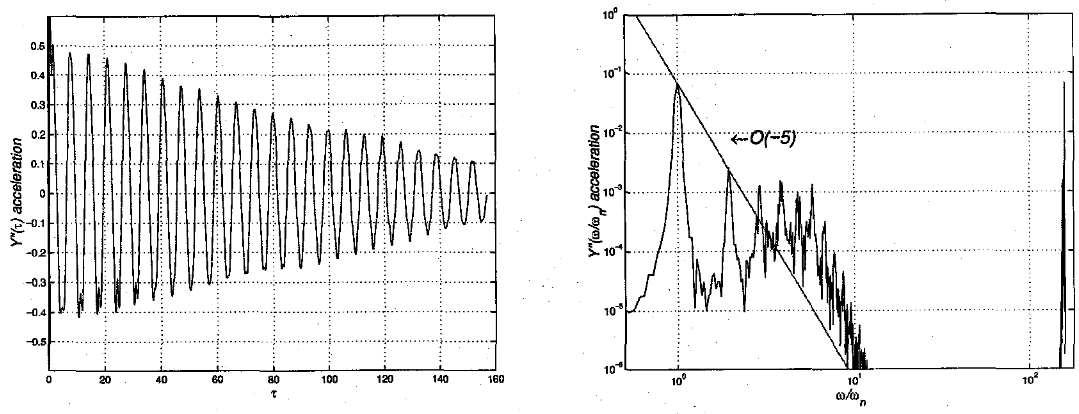

Figure 6.28 Free vibration acceleration filtered at f/f_n=5.5

6.10. Least Square Fit

A least square fit is used to find the structural parameters from the values of *Y(τ)* and its derivatives at the sampled points. We start with a simple mass-spring model ($\ddot{Y}+2\xi\dot{Y}+Y=0$) and proceed to higher order models if necessary. Assuming a DC component within *Y(τ)* to be included in the fit and evaluating the *ODE* at sampled points, we have

$$a\ddot{\vec{Y}}+b\dot{\vec{Y}}+c\vec{Y}+d=0 \qquad \textbf{Equation 6.6}$$

where $\vec{Y}$ represents the time series of Y at sampled points and a, b, and c the structural coefficients and d the possible DC component. Since the time trace is already non-dimensionalized according to $\tau=\omega_n t$, the coefficients a and c should be close to 1. Equation 1.4 represents a redundant system of linear equations with as many rows as the number of signal points used and only four columns. Manipulating the above equation, we have

$$\begin{bmatrix} \dot{\vec{Y}} & \vec{Y} & \vec{I} \end{bmatrix} \begin{bmatrix} b/a \\ c/a \\ d/a \end{bmatrix} = -\begin{bmatrix} \ddot{\vec{Y}} \end{bmatrix}$$ **Equation 6.7**

which is in ***Ax=b*** form. Using the usual technique for solving such redundant systems, we multiply both sides by A^T and solve the resulting square matrix equation

$$(A^T A)\vec{x} = A^T b$$ **Equation 6.8**

by multiplying both side by $(A^T A)^{-1}$

$$\vec{x} = (A^T A)^{-1} A^T b$$ **Equation 6.9**

This method is equivalent to defining and minimizing a fit remainder function $R = \ddot{\vec{Y}} + b/a\dot{\vec{Y}} + c/a\vec{Y} + d/a$ .through derivatives. The following values are obtained:

$c/a = 0.9241$

$b/a = 0.0416$

$d/a = -0.0008$

The parameter *d/a* is quite small since an estimate of the offset based on a non-oscillatory segment of the original trace was already subtracted. The value of *c/a* is close to one, but the small difference indicates that ω_n based on the *FFT* of the segment was slightly different from that determined by the fit. Comparing the two equations below

$$\ddot{\vec{Y}} + b/a\dot{\vec{Y}} + c/a\vec{Y} + d/a = 0 \qquad \text{and} \qquad \ddot{\vec{Y}} + 2\zeta\omega_n\dot{\vec{Y}} + \omega_n{}^2\vec{Y} = 0$$

the natural frequency ω_n and damping ζ are obtained as

$$\omega_n=(c/a)^{1/2}=0.962 \text{ and } 2\zeta= b/a/(c/a)^{1/2}=0.043.$$

Since the trace was non-dimensionalized using ω_n=5.95 Hz, the fitted physical value for ω_n is

$$\omega_n=5.95\times0.962=5.719 \text{ Hz}$$

which is very close to the *FFT* natural frequency computed based on the entire trace (0.720). The damping coefficient ζ=0.022 is somewhat larger than the previous estimate based on the linear theory ($0.0065<\zeta<0.012$ from Equation 5.5). This large discrepancy is most probably due to an inherent non-linearity which the fitting technique attempts to capture in the linear damping term.

It is worth noting that the signal at hand does not appear to be strongly non-linear at sight and that linear estimates such as Equation 5.5 are commonly used by researchers. As we shall see, the exact value of ζ does not play an important role in deducing the force magnitude. Reporting an exact value for ζ is, nevertheless, crucial in comparing *VIV* results for it influences the amplitude response curve.

Figure 6.29 shows a comparison of the acceleration term $\ddot{Y}$ and $\ddot{Y}$ prediction for the acceleration $b/a\dot{\vec{Y}} + c/a\vec{Y} + d/a$ based on the fit and the fit error on the right, the part of the signal not accounted for by the fit $R = \ddot{\vec{Y}} + b/a\dot{\vec{Y}} + c/a\vec{Y} + d/a$. The amount of the error declines to half as the signal is filtered more strongly (cutoff at f_c/f_n=2), the ω_n value is quite stable and ζ declines slightly to ζ=0.02.

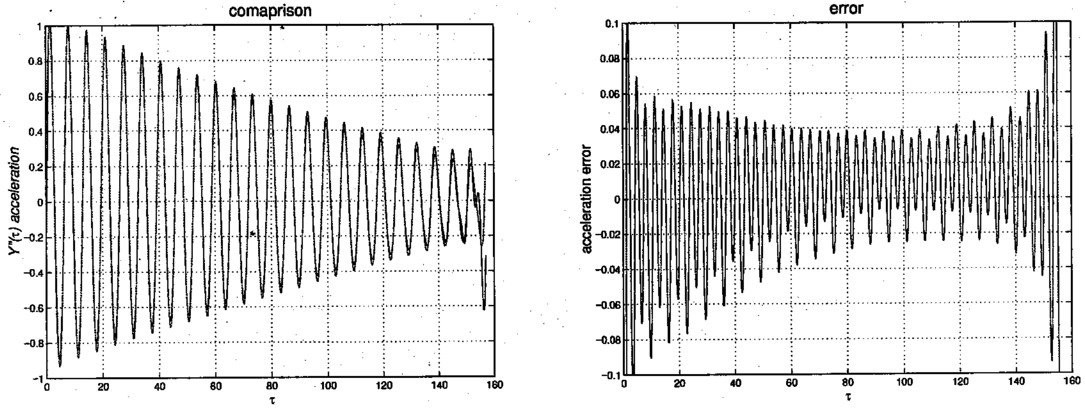

Figure 6.29 Fit success, $\ddot{Y}$ and $b/a\vec{\ddot{Y}}+c/a\vec{Y}+d/a$ on left and the error on the right

The values of damping reported in chapters 4 and 5 are based on the linear theory in Equation 5.5 ($\zeta = -1/(2\pi n) \ln(P_n/P_1)$) so that they can be compared to the values reported by other researchers.

6.11. Fluid Force

In this section a linear model of the structure along with the parameters found through the fitting technique in the previous section is used to find the instantaneous fluid force coefficient $C_y(\tau)$ for the time trace studied in section 6.6.

$$C_y(\tau)=\frac{m^*}{U^2}(\ddot{Y}+2\xi\dot{Y}+Y) \qquad \text{Equation 5.1}$$

The two terms Y and $\ddot{Y}$ are $O(1)$ and the damping term $2\zeta\dot{Y}$ is $O(0.01)$ and hence less crucial. Close to the natural frequency Y and $\ddot{Y}$ nullify to a large extent, and only then, is the exact values of ζ of importance. For the same reason, accurate non-dimensionalization of time is important. The flow structure parameters are as follows: case *S1*, $m^*=28$, $2\zeta=0.043$, $U=0.956$, $\omega_n=5.719$ Hz. Figure 6.30 shows the time trace $Y(\tau)$ and its second derivative after a filter with $f_c/f_n=5.5$. The sum of the two traces Y and $\ddot{Y}$ is also shown on the left and the force coefficient on the right.

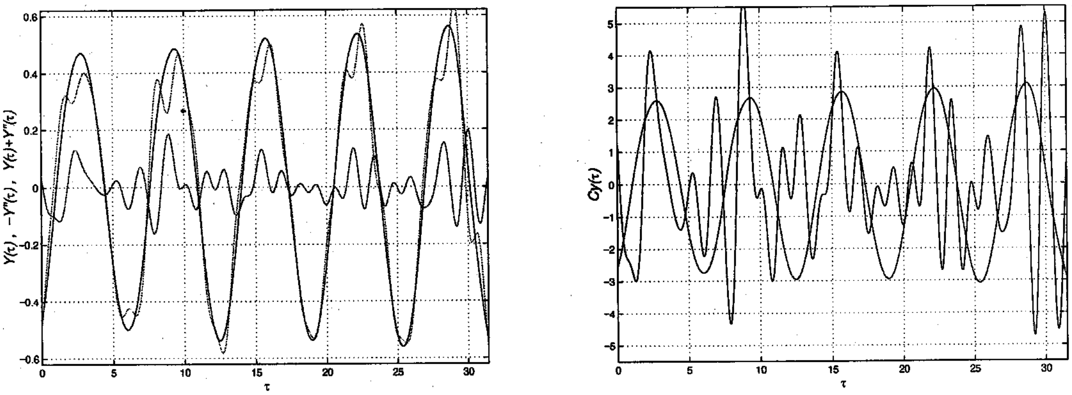

Figure 6.30 Y, $\ddot{Y}$, $Y+\ddot{Y}$ (left) and $C_y(\tau)$ and $Y(\tau)$ (right) $f_c/f_n=5.5$ (the sinusoidal-like signal on the right is the displacement $Y(\tau)$ rescaled for comparison)

Since $\omega/\omega_n=0.984$ for this trace is very close to 1, the two main components of the force $Y(\tau)$ and $\ddot{Y}(\tau)$ nullify to a large extent and the sum contains large high harmonic content. The lift coefficient $C_y(\tau)$ seems to have a larger than expected amplitude (C_y=3.24) and much harmonic activity.

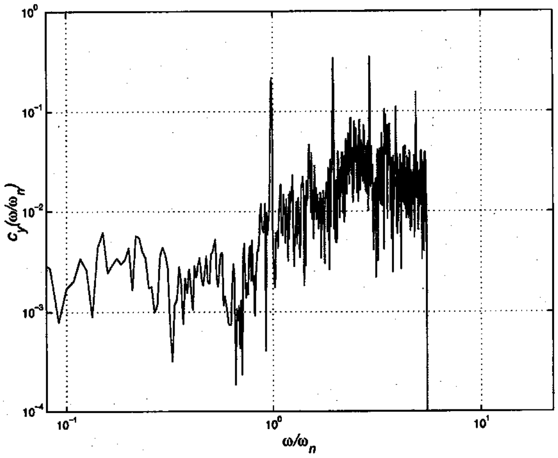

Figure 6.31 C_y frequency spectrum

This harmonic content is obviously sensitive to the filter cutoff f_c. Choosing a cutoff frequency of $f_c/f_n = 3.5$ with large risk of over-filtering the data yields C_y=2.7 and the curves in Figure 6.32.

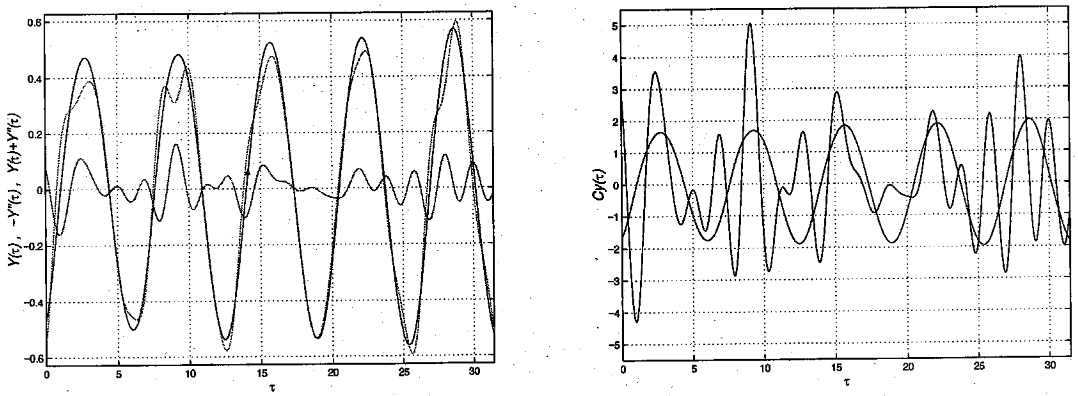

Figure 6.32 Y, $\ddot{Y}$, $Y+\ddot{Y}$ **(left) and** $C_y(\tau)$ **and** $Y(\tau)$ **(right) with** $f_c/f_n = 3.5$ **filter cutoff**

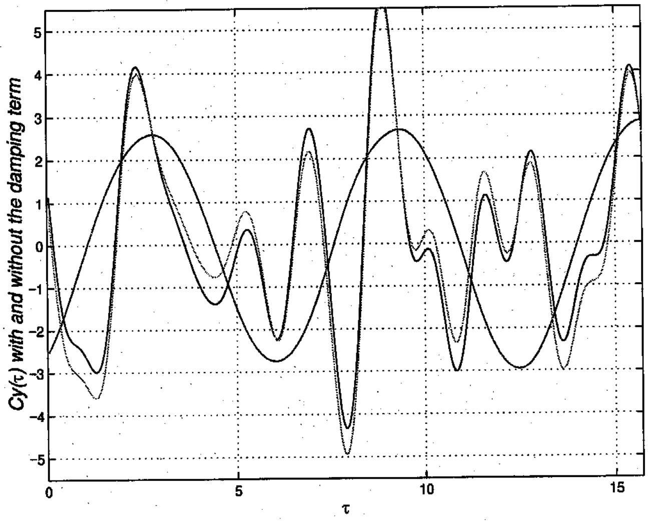

Figure 6.33 $C_y(\tau)$ **with and without the damping term** $\xi\dot{Y}$ $(f_c/f_n = 5.5)$

Figure 6.33 shows the lift coefficient $C_y(\tau)$ where the damping term $\xi\dot{Y}$ is excluded along with $Y(\tau)$ for reference. It serves to show that the damping parameter does not play an important role in retrieving the instantaneous fluid force.

6.12. Higher Order Structural Models

After studying the fit error trace in Figure 6.29, it is possible to employ higher order models to minimize the energy frequency content of the fit error. Assuming the model in Equation 6.3 $\ddot{Y}+2\zeta\dot{Y}+Y+kY^3+b_n\dot{Y}\left|\dot{Y}\right|^n+c\,\mathrm{sgn}(\dot{Y})+\ldots=0$ and even higher order models (up to 18 terms tested) can help reduce the magnitude of the error to only a half. Using the a general equation for the system as in $\ddot{Y}+Z(Y,\dot{Y})=0$ leads to the general structural function $Z(Y,\dot{Y})=-\ddot{Y}$ depicted in Figure 6.34. The warped shape of this function does improve with lower filter cutoff. However at f_c/f_n=5.5, there is only so much one can accomplish with higher order structural models. In other words, capturing such warped asymmetric shape by assuming simple non-linear terms is quite challenging. As previously mentioned the fit error diminishes as stronger filters are employed. Although the final lift coefficient is not sensitive to accurate contributions to damping, the phase of the force signal relies solely on such terms.

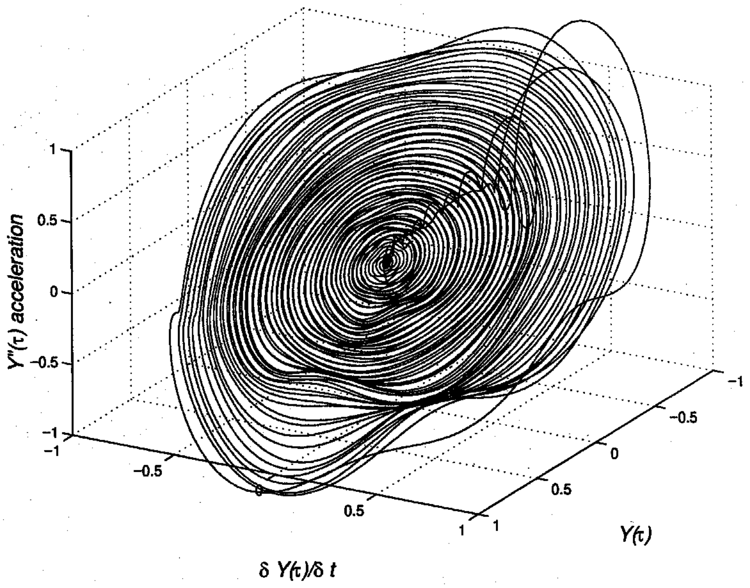

Figure 6.34 Free decay vibration $\ddot{Y}=-Z(Y,\dot{Y})$, filter cutoff at f_c/f_n=5.5.

6.13. Conclusion

A novel technique for deducing time-dependent fluid forces was introduced that involves numerical evaluation of the structural forces such as inertia, damping and stiffness to deduce the fluid force causing the vibration. A least-square fitting technique was employed to obtain the structural parameters from a free decay oscillation of the structure. A variety of filtering experiments was conducted to obtain a safe filter cutoff in order to achieve the second derivative of the displacement traces. A frequency cut-off at $f_c/f_n = 5.5$ was finally chosen to exclude the high frequency noise as well as preserving the signal contents. The magnitude of the force signal obtained is more sensitive to an accurate measurement of the natural frequency than the damping parameter. Force traces show large harmonic activity and relatively small content at the fundamental $f=f_n$ depending on values of f/f_n. When $f/f_n=1$, the force trace contains little fundamental frequency content. An accurate modeling of the damping terms while negligible in force magnitudes is crucial in deducing the force-displacement phase.

SUMMARY

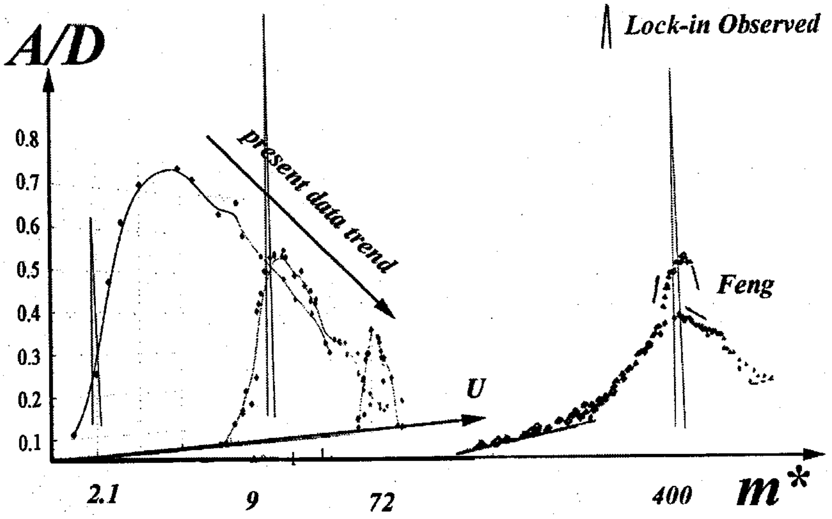
Lock-in Observed
A/D
0.8
0.7
0.6
0.5
0.4
0.3
0.2
0.1
present data trend
Feng
U
2.1
9
72
400
m*

Summary

Vortex-induced vibrations (*VIV*) of an elastically held cylinder in cross flow was studied for low to medium values of the mass ratio parameter $2<m^*<72$. A new *VIV* mode was discovered with no lock-in behavior. Lock-in, as observed in Feng's [1968] experiment, was absent in most cases studied. The oscillation and the shedding frequencies coalesced but their values increased with increasing flow speeds and smoothly deviated from the nominal Strouhal frequency of $St=0.2$ to smaller values. For mass ratios $m^*>10$, and with increasing mass ratios, the frequency growth with the free stream velocity U either approached the lock-in limit or no *VIV* was detected. The oscillation amplitude and frequency range diminished with increasing m^*. This general trend does not support the relatively large amplitudes observed in the high mass ratio study of Feng. A lock-in interval was observed in a 2D oscillation run involving $m^*=9$ where no frequency growth with U was detected.

The common absence of lock-in at low mass ratios, the significant deviation from Feng's results, and the common absence of any vibrations at medium to high mass ratios were explained using the effective stiffness introduced in chapter 2. According to this novel approach, for a single frequency response, the lift coefficient C_y and the oscillation amplitude A^* are related as $C_y=A^*\ k^*_{eff}$ where the effective stiffness k^*_{eff} is defined as $k^*_{eff}= m^*/U^2(1-(f/f_n)^2)$. A minimum value of the effective stiffness thus can result in pronounced oscillation amplitudes. Although a large mass ratio as in Feng's experiment can maximize the effective stiffness according to the above definition, a lock-in behavior, $f/f_n=1$, can minimize it effectively rendering large vibration amplitudes. When the lock-in condition is not encountered, increasing mass ratios result in smaller response amplitude and range. Lock-in may be observed at any mass ratio; however, at high mass ratios, lock-in is a prerequisite for *VIV*. *VIV* at high mass ratios is thus synonymous with lock-in.

At small to medium values of the mass ratio such as in the experiments at hand, effective stiffness is relatively small and the sheer fluid momentum can drive the system without any lock-in requirement. Lock-in may occur however and cause large oscillations in this range.

A novel technique was also developed to deduce time-dependent fluid forces using time traces of the structural vibration and its derivatives. The lift coefficients obtained are significantly larger than values from previous studies and involve much high frequency content. An accurate modeling of the structural parameters and an accurate filtering technique for obtaining numerical derivatives of the displacement can help reconstruct accurate fluid forces. The force magnitude relies on the exact measurement of the system natural frequency. On the hand, the force-displacement phase ϕ requires an accurate modeling of other system parameters. Improved fitting techniques may help model such small terms.

Other Observations

Two-dimensional figure 8 oscillations of cylinders in cross flow with $m^*<10$ supported the common absence of lock-in for the most part. Unprecedented oscillation amplitudes above one diameter were observed.

Feng's results seem to involve relatively large amplitudes compared to the trends studied in this chapter. According to the effective stiffness theory, lock-in behavior, that is $f/f_n=1$ for a certain range in U is the only possible explanation for Feng's result. The fluid mechanical reason behind such behavior is not fully understood. The present study simply shows that lock-in small at values of m^* is either less likely to occur or is engulfed by a different phenomenon, *VIV* due to large fluid forces.

Forced oscillation experiments involve a different physical phenomenon where the structural motion dominates the fluid mechanics. The natural competition between the structural and fluid forces and their corresponding frequencies is absent there. The dominance of the fluid forces and frequencies in small mass ratios as observed in this study is not reflected in such experiments. More experiments need to be conducted on freely oscillating structures. Simple models can not capture the complexities revealed in this work. Models may need to include history.

Steady *VIV* for medium to large mass ratios ($m^*>30$) was difficult to achieve within laboratory limits. The cases presented are part of a large number experiments that did not result in *VIV*. Free stream velocity predictions based on natural frequency, linear damping and mass ratio did not always guarantee a *VIV* behavior.

Using effective stiffness, $k^*_{eff}=-\omega^{*2}m^*+k^*$, the amplitude response curves seem to exhibit largest amplitudes in a range $0<k^*_{eff}<5$. Assuming nominal values of the lift coefficient, one can estimate the oscillation amplitudes for zero values of damping b^* using this parameter. It is, however, impossible to predict f^* behavior a priori. In the present study the variations in amplitude for given values of k^*_{eff} are due to variations in b^*. It is also possible to obtain a single frequency estimate to the lift coefficient using this concept according to $C_y=A^* k^*_{eff}$.

Comparison of the amplitude response, A/D vs. k^*_{eff}, with Numerical results of Shiels [1998] at Re=100 shows great similarity, emphasizing the similarities in wake dynamics for different values of the *Reynolds* number.

VIV Oscillations studied seem to occur within the *2P* region on the Williamson-Roshko plane. The actual shedding modes for these experiments are not known and may not necessarily be *2P*. The results do not necessarily resemble those obtained by Brika and Laneville [1993].

The mass-damping parameter, $m^*\zeta$, does not seem to uniquely determine a trend for the maximum amplitude A_{max}. Larger values of mass-damping may involve larger oscillation amplitudes. This is mainly due to the unpredictable frequency response. The absence or existence of a lock-in behavior can greatly influence the amplitude of oscillation. Other factors such as history and shedding modes that affect C_y may also change the A_{max} values.

The amplitude A/D vs. U response curve may have different overall shapes. These Shapes vary from round and smooth at small values of m^* to double-peaks with humps at medium values of m^* (similar to those reported by Khalakh and Williamson [1997]) and finally to intermittent behavior at large values of m^*. Damping and possibly different shedding modes may be important. The frequency response on the other hand exhibits similar deviation from *Strouhal* curve to various extents.

The maximum amplitude of oscillation, A_{max} may not be reached at U=1. Damping and nonlinearity may be important (Hover and Triantafyllou [1998]). Using f_{Amax}, the oscillation frequency at maximum oscillation amplitude may help compare the amplitude and frequency graphs vs. the free stream velocity. Frequency data from various runs seem to fall in a narrow band using this method.

Simple *FFT* may not reflect small changes in frequency as peak counting or Empirical Mode Decomposition do. Quasi-periodicity and nonlinearity within signals can result in inaccurate *FFT* frequency results. Both *EMD* and sectional *FFT* analysis, however, show the existence of multiple frequencies. Present plotting methods may be too simplistic.

REFERENCES

References

Anagnostopoulos, P., 1994, "Numerical Investigation of Response and Wake Characteristics of a Vortex-Excited Cylinder in a Uniform Stream," *Journal of Fluids and Structures*, Vol. 8, pp. 367-390.

Bearman, P. W., 1984, "Vortex Shedding form Oscillating Bluff Bodies, "*Annual Review of Fluid Mechanics*, Vol. 16, 195-222.

Berger, E., 1987, "On a Mechanism of Vortex-Excited Oscillations of a Cylinder, "In: *Proceedings of 7th International Conference on Wind Engineering*, Aachen.

Bert, C. W., 1973, "Material Damping: An Introductory Review of Mathematical Models, Measures and Experimental Techniques, "*Journal of Sound and Vibration*, Vol. 29(2), pp. 129-153.

Billah, K. Y. and Scanian, R. H., 1991, "Resonance, Tacoma Narrows Bridge Failure, and Undergraduate Physics Textbooks," *American Journal of Physics*, Vol. 59(2), pp. 118-122.

Bishop, R. E. D. and Hassan, A. Y., 1964, "The Lift and Drag Forces on a Circular Cylinder Oscillating in a Flowing Fluid," *Proceeding of the Royal Society of London*, Vol. 277, pp. 51-75.

Blackburn, H. and Henderson, R., 1996, "Lock-In Behavior In Simulated Vortex-Induced Vibration," *Experiments in Thermal and Fluid Science*, Vol. 12(2), pp. 184-189.

Blackburn, H. and Henderson, R., 1998, "A Study of Two-dimensional Flow Past an Oscillating Cylinder," to appear in the *Journal of Fluid Dynamics*.

Blevins, R. D., 1990, "Flow-Induced Vibration, 2nd Edition," Krieger Publishing, Malabar, Florida.

Blevins, R. D., 1991, "Application of the Discrete Vortex Method to Fluid-Structure Interaction," *Journal of Pressure Vessel, ASME*, Vol. 113(3), pp. 437-445.

Brika, D., and Laneville, A., 1993, "Vortex-induced Vibrations of a Long Flexible Circular Cylinder," *Journal of Fluid Mechanics*, Vol. 250, pp. 481-508.

Feng, C. C., 1968, "The measurement of Vortex-Induced Effects in Flow past Stationary and Oscillating Circular and D-section Cylinders," M.A.Sc., Thesis, University of British Columbia, Vancouver, B. C., Canada.

Ferguson, N., Parkinson, G. V., 1967, "Surface and Wake Flow Phenomena of the Vortex-Excited Oscillation of a Circular Cylinder," *ASME Journal of Engineering for Industry*, Vol. 89, pp. 831-838.

Gharib, M. R., Shiels, D., Gharib, M., Leonard, A., and Roshko A., 1997, "Exploration of Flow-Induced Vibration at Low Mass and Damping," *ASME 4th International Symposium on Fluid-Structure Interaction, Aeroelasticity, Flow-Induced Vibration, and Noise*, Dallas, TX, Nov. 16-21.

Gharib, M. R., Gharib, M., Leonard, A., and Roshko, A., 1998, "The Absence of Lock-in and the Role of Mass-ratio," *ASME 5th International Symposium on Fluid-Structure Interaction, Aeroelasticity, Flow-Induced Vibration, and Noise*, Washington DC.

Gharib, M. R., Shiels, D., Leonard, A., and Roshko, A., "Flow-Induced Vibration of a Cylinder at Zero Mass and Damping," submitted to the *Journal of Fluids and Structures*.

Gharib, M. R., Leonard, A., and Roshko, A., "The Absence of Lock-in and the Role of Mass-ratio," to be submitted to the *Journal of Fluids and Structures*.

Griffin, O. M., 1971, "The Unsteady Wake of an Oscillating Cylinder at Low Reynolds Number," *Journal of Applied Mechanics*, Vol. 38, pp. 729-738.

Griffin, O. M., Skop, A. R. and Koopman, G. H., 1973, "The Vortex-Excited Resonant Vibrations of Circular Cylinders," *Journal of Sound and Vibration*, Vol. 31, pp. 235-249.

Griffin, O. M. and Ramberg, S. E., 1974, "The Vortex Street Wakes of Vibrating Cylinders," *Journal of Fluid Mechanics,* Vol. 66, pp. 553-576.

Griffin, O. M., Ramberg, S. E., 1982, "Some Recent Studies Of Vortex Shedding With Application To Marine Tubulars And Risers," *Journal of Energy Resources, ASME* Vol. 104 (1), pp. 2-13.

Griffin, O. M., 1982, "Vortex Streets And Patterns," *Mechanical Engineering*, Vol. 104 (3), pp. 56-61.

Griffin, O. M., 1983, "Modification Of Vortex Shedding In The Synchronization Range," *Journal of Fluid Engineering, ASME* Vol. 105 (1), pp. 123-123.

Griffin, O. M., and Hall, M. S., 1991, "Review- Vortex Shedding Lock-on and Flow Control in Bluff Body Wakes," *ASME Journal of Fluid Engineering*, Vol. 113, pp. 526-537.

Griffin O. M., Hall, M. S., 1991, "Vortex Shedding Lock-On And Flow-Control In Bluff Body Wakes – Review," *Journal of Fluid Engineering, ASME* Vol. 113 (4), pp. 526-537.

Gopalkrishnan, R., 1992, "Vortex-Induced Forces on Oscillating Bluff Cylinders," Ph.D. thesis, Massachusetts Institute of Technology, Cambridge, MA.

Hall, M. S., Griffin O. M., 1993, "Vortex Shedding And Lock-On In A Perturbed Flow," *Journal of Fluid Engineering, ASME* Vol. 115 (2), pp. 283-291.

Hall S. S., Iwan, W. D., 1984, "Oscillations of a Self-Excited Nonlinear System," *Journal of Applied Mechanics*, Vol. 51, pp. 892-898.

Hartlen, R. T., and Currie, I. G., 1970, "Lift-oscillator Model of Vortex-Induced Vibration," *Journal of the Engineering Mechanics Division of ASCE*, Vol. 96, EMS, pp. 577-591.

Hover, F. S., Miller, S. N., and Triantafyllou, 1997, "Vortex-Induced Vibration of Marine Cables: Experiments Using Force Feedback," *Journal of Fluids and Structures*, Vol. 11, pp. 307-326.

Huang, E. et al., 1998, "The Empirical Mode Decomposition and the Hilbert Spectrum for Non-linear and Non-stationary time series analysis," *Proceedings of the Royal Society of London*, Vol. 454, pp. 903-995.

Jones, G. W., 1968, "Unsteady Lift Forces Generated by Vortex, Shedding about a Large, Stationary and Oscillating Cylinder at High Reynolds Number mp. Unsteady Flows," *ASME*, Philadelphia, May 1968.

Khalak, A., Williamson, C. H. K., 1997, "Dynamics of a hydroelastic cylinder with very low mass and damping," *Journal of Fluids and Structures*, Vol. 10, pp. 455-472.

King, R., Prosser, M., 1972, "Criteria for Flow-Induced Oscillations of a Cantilevered Cylinder in Water," IUTAM-IAHR Symposium on Flow-Induced Structural Vibrations, Karlsruhe, editor: E. Naudascher, pp. 488-503.

King, R., Prosser, M., 1973, "On Vortex Excitation of Model Piles in Water," *Journal of Sound and Vibration*, 29(2), pp. 169-1888.

Moe, G., and Wu, Z. J., 1990, "The Lift Force on a Cylinder Vibrating in a Current," *ASME Journal of Offshore Mechanics and Arctic Engineering*, Vol. 112, pp. 297-303.

Naudasher, N. and Rockwell, D., 1994, "Flow-Induced Vibration, an Engineering Guide", A. A. Balkema, Rotterdam, Netherlands.

Newman DJ, Karniadakis G. E., 1997, "A direct numerical simulation study of flow past a freely vibrating cable," *Journal of Fluid Mechanics*, Vol. 344, pp. 95-136.

Noca, F., 1996, "On the Evaluation of Instantaneous Fluid-Dynamic Forces on a Bluff Body," *GALCIT Report*, FM96-5.

Noca, F., 1997, "On the Evaluation of Instantaneous Fluid-Dynamic Forces on a Bluff Body (Part II)," *GALCIT Report*, FM96-5.

Noca, F., Shiels, D., and Jeon, D., 1997, "Measuring Instantaneous Fluid Dynamic Forces on Bodies, Using Only Velocity Fields and their Derivatives," *Journal of Fluids Structures*, Vol. 11, 345.

Noca, F., Shiels, D., and Jeon, D., 1998, "Measuring Instantaneous Fluid Dynamic Forces on Bodies, Using Only Velocity Fields and their Derivatives," *Journal of Fluids Structures*, submitted.

Norberg, C., 1994, "An Experimental Investigation of the Flow Around a Circular Cylinder - Influence of Aspect Ratio," *Journal of Fluid Mechanics*, Vol. 258, pp. 287-316.

Ongoren, A. and Rockwell, D., 1988, "Flow Structure from an Oscillating Cylinder," Part 1: "Mechanisms of Phase Shift and Recovery in the Near Wake," *Journal of Fluid Mechanics*, Vol. 191, pp. 197-223.

Ongoren, A. and Rockwell, D., 1988, "Flow Structure from an Oscillating Cylinder," Part 2: "Mode Competition in the Near Wake," *Journal of Fluid Mechanics*, Vol. 191, pp. 225-245.

Otter, A., 1990, "Damping Forces on a Cylinder Oscillating in a Viscous Fluid," Technical Note, *Applied Ocean Research*, Vol. 12(3), pp. 153-155.

Pantazopoulos, M. S., 1994, "Vortex-Induced Vibration Parameters: Critical Review," *Proceedings of the Offshore Mechanics and Arctic Engineering Conference*, Vol. 1, pp. 199-234.

Parkinson, G. V., 1989, "Phenomena and Modeling of Flow-Induced Vibrations of Bluff Bodies," *Progress in Aerospace Science., Vol.* 26, pp. 169-224.

Parkinson, G. V., Feng, C. C., Ferguson, N. 1972, "Mechanisms of Vortex-Excited Oscillation of Bluff Cylinders," *Proceedings of Symposium on Wind Effects on Buildings and Structures,* Loughborough, England, paper 27.

Parkinson, G. V., 1972, "Mathematical Models of Flow-Induced Vibrations of Bluff Bodies," General Lecture, *Proc. IUTAM Symposium on Flow-Induced Structural Vibrations,* Springer Verlag Berlin, Heidelberg, New York, pp. 81-127.

Press, W. H., Teukolsky, S. A., Vetterling, W. T., Flannery, B. P., 1992, "Numerical Recipes in C, The Art of Scientific Computing," second edition, Cambridge University Press.

Roshko, A., 1954, "On the Development of Turbulent Wakes from Vortex Streets," National Advisory Committee for Aeronautics, NACA Tech Report 1191.

Roshko, A., 1954, "On the Drag and Shedding Frequency of Two-Dimensional Bluff Bodies," *NACA TN 3169*.

Roshko, A., 1961, "Experiments on the Flow Past a Cylinder at Very High Reynolds Number," *Journal of Fluid Mechanics*, Vol. 10, 345.

Sarpkaya, T., 1978, "Fluid Forces on Oscillating Cylinders," *ASCE Journal of Waterway, Port, Coastal, and Ocean Division* Vol. 104, pp. 275-290.

Sarpkaya, T., 1979, "Vortex-Induced Oscillations - A Selective Review," *ASME Journal of Applied Mechanics*, Vol. 46, pp. 241-258.

Sarpkaya, T., 1989, "Computational Methods With Vortices," The 1988 Freeman Scholar Lecture, *Journal of Fluid Engineering-T, ASME* Vol. 111 (1), pp. 5-52 Mar 1989.

Sarpkaya, T., 1994, "Unsteady Flows: A Selective Review," *Handbook of Fluid Dynamics*, ed., Joseph A. Schetz, McGraw-Hill, New York, NY.

Sarpkaya, T., 1995, "Hydrodynamic Damping, Flow-Induced Oscillations, and Biharmonic Response," *ASME Journal of Offshore Mechanics and Arctic Engineering*, Vol. 117, pp. 232-238.

Shiels, D., 1998, "Simulation of Controlled Bluff Body Flow with a viscous Vortex Method," Ph.D. thesis, California Institute of Technology, Pasadena, California.

Shiels, D., Leonard, A., Roshko, A., 1998, "Flow-Induced Vibration of a Circular Cylinder at Limiting Structural Parameters," submitted to *Journal of Fluids and Structures*.

Smirnov, L.P., Pavlihina, M. A., 1957, "Vortical Traces for Flow around vibrating cylinders," presented at the I.M.A. Communications Meeting, Moscow, October 1957.

Stansby, P. K., 1976, "The Locking-on of Vortex Shedding due to the Cross Stream Vibration of Circular Cylinders in Uniform and Shear Flows," *Journal of Fluid Mechanics*, Vol. 74, Part 4, 1976, pp. 641-665.

Staubli, T., 1983, "Calculation of the Vibration of an Elastically Mounted Cylinder Using Experimental Data from Forced Oscillation," *Journal of Fluids Engineering*, Vol. 105, pp. 225-229.

Staubli, T., 1983, "Eine Untersuchung der Instationaeren Kraefte am Querangestroemten, Erzwungen Schwingenden Kreiszylinder," Ph.D. thesis, Swiss Federal Institute of Technology, Zurich, Nr. 73 22.

Tanaka, H., and Takahara, S., 1969, "Unsteady Air Forces Acting on a Vibrating Circular Cylinder," *Proceedings of the 19th Japan National Congress App. Mech.*

Williamson, C. H. K., and Govardhan, R., 1997, "Dynamics and Forcing of a Tethered Sphere in a Fluid Flow," *Journal of Fluids and Structures*, Vol. 11, pp. 293-305.

Williamson, C. H. K., and Khalak, A., 1997, "Fluid Forces and Dynamics of a Hydroelastic Structure with Very Low Mass and Damping," Special Brief Note, *Journal of Fluids and Structures*, Vol. 11, pp. 973-982.

Williamson, C. H. K., and Roshko, A., 1988, "Vortex Formation in the Wake of an Oscillating Cylinder, "*Journal of Fluids and Structures*, Vol. 2, pp. 355-381.

Zdravkovich, M. M., 1996, "Different Modes of Vortex Shedding: An Overview," *Journal of Fluids and Structures*, Vol. 10, pp. 427-437.

Zdravkovich, M. M., 1996, "Flow around Circular Cylinders, Vol. 1," *Oxford: Oxford University Press.*

APPENDICES

A Appendices

A.1 Detailed View of the Experimental Setup

A detailed view of the experimental setup and their components is presented. A brief description will be given in figure caption. The reader may refer to chapter 3 for further explanation of the setup.

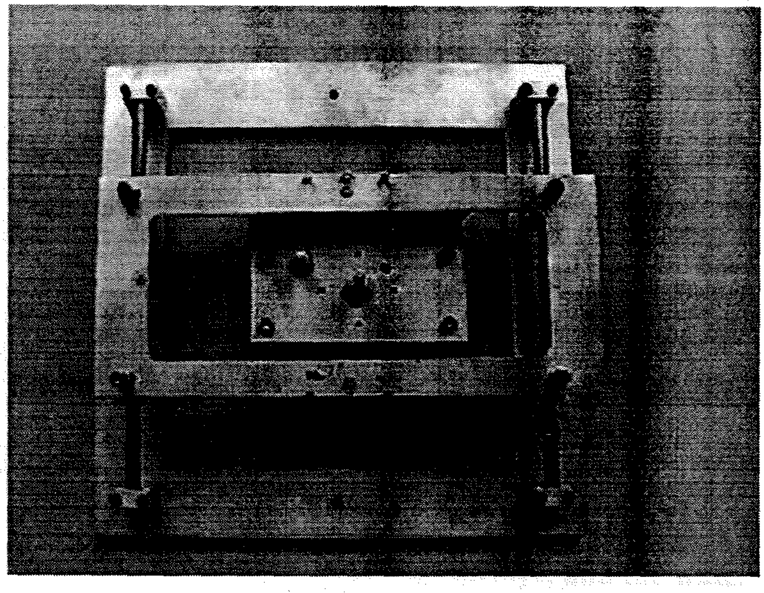

Fig. 1 The traverse and the cylinder attachment in the center with a center piece capable of moving in *x* and *y*. Flow from left to right conceptually

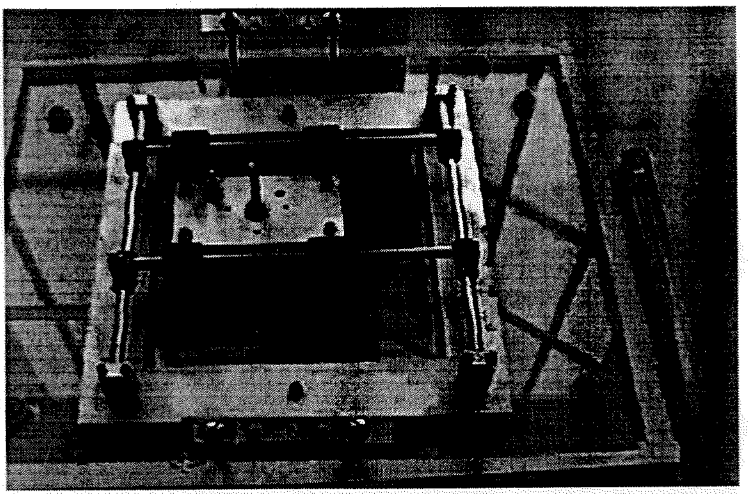

Fig. 2 The x and y rods and bearings, the Plexiglas platform and the spring brackets on the sides

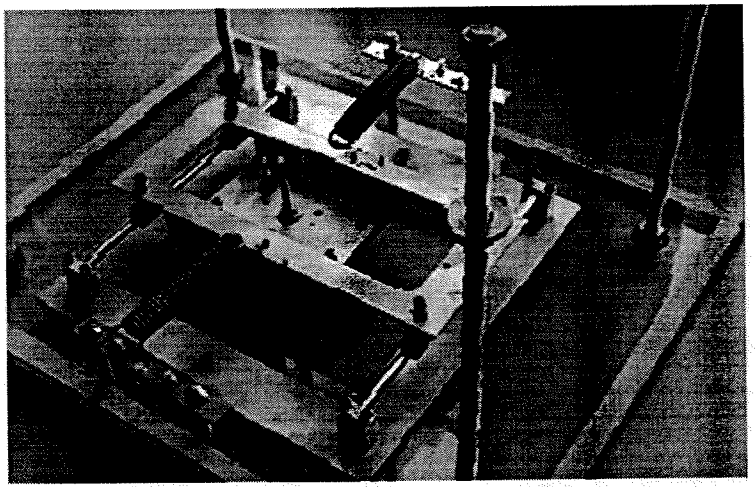

Fig. 3 The Plexiglas platform, the complete traverse, springs, and the water tunnel attachments

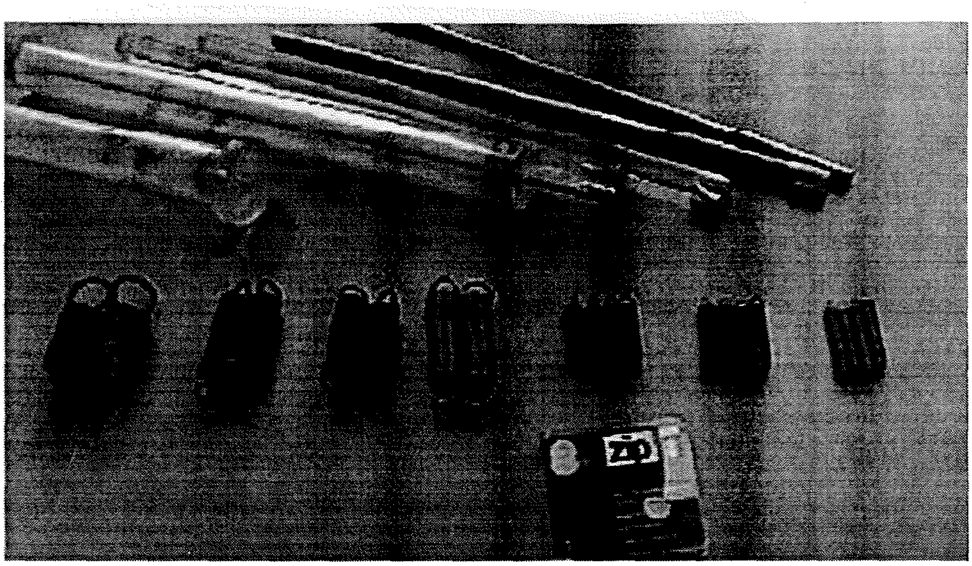

Fig. 4 Cylinder models, springs (1.2[lb/in]<k<46[lb/in]) and a 4 inch zip disk for comparison

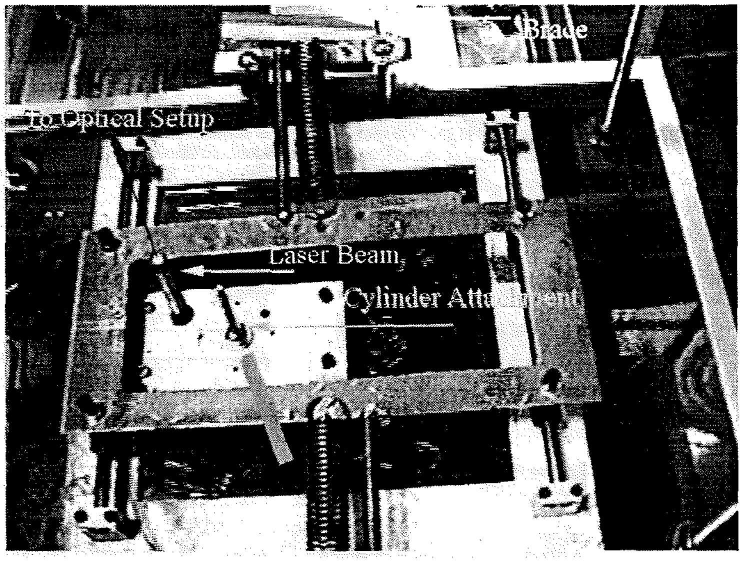

Fig. 5 Tunnel mounting, LED laser, braces against tunnel walls and cylinder attachment

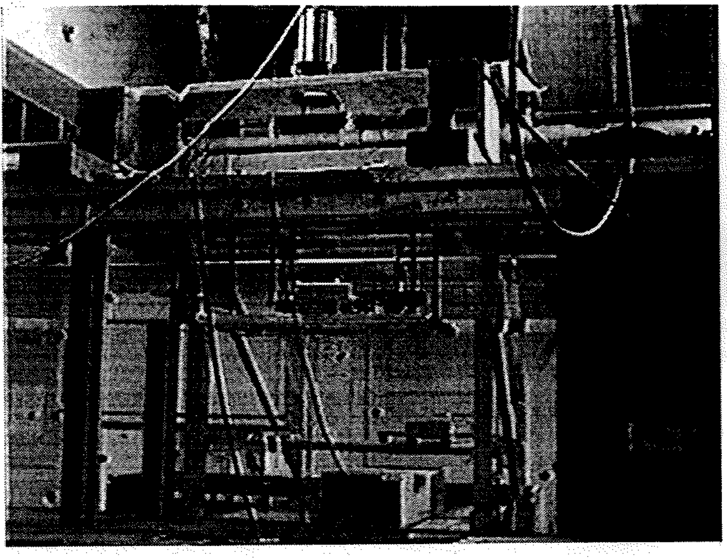

Fig. 6 The entire setup including the platform on the free surface, a Plexiglas cylinder and the optical setup on top of the tunnel. The *LDA* and the hot film not clearly visible. Flow from right to left

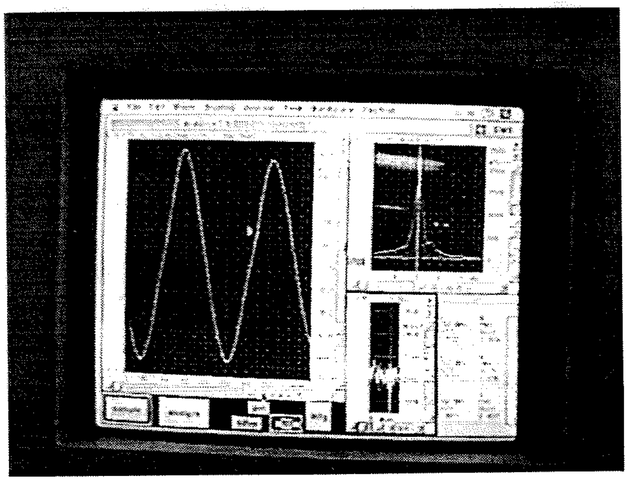

Fig. 7 Superscope data acquisition and the computer interface

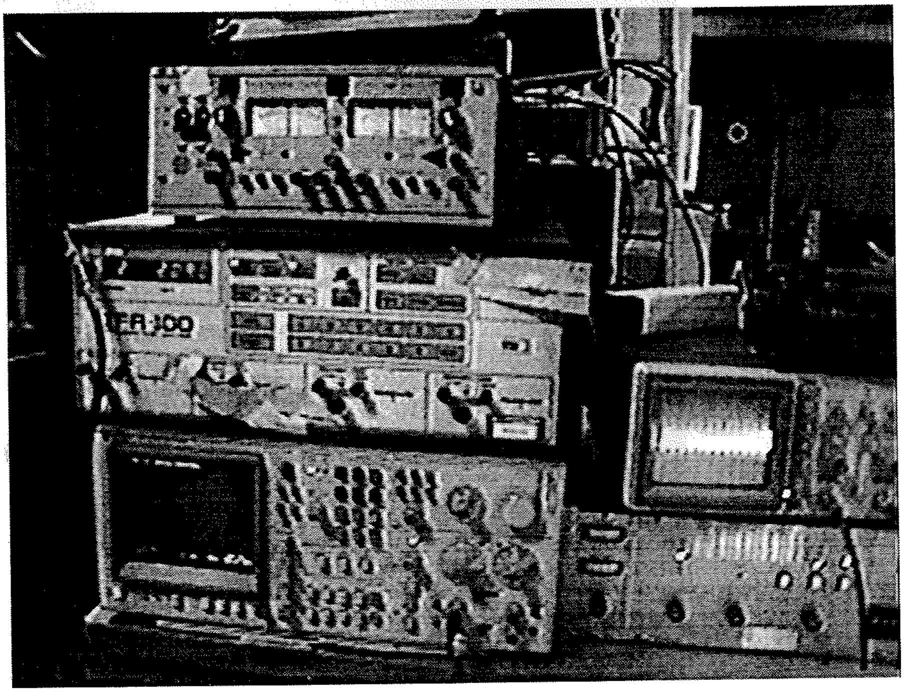

Fig. 8 IFA-100 Flow Analyzer for hot film anemometery, power supply, a HP frequency analyzer for the wake signals and an oscilloscope

A.2 Optical Calibration

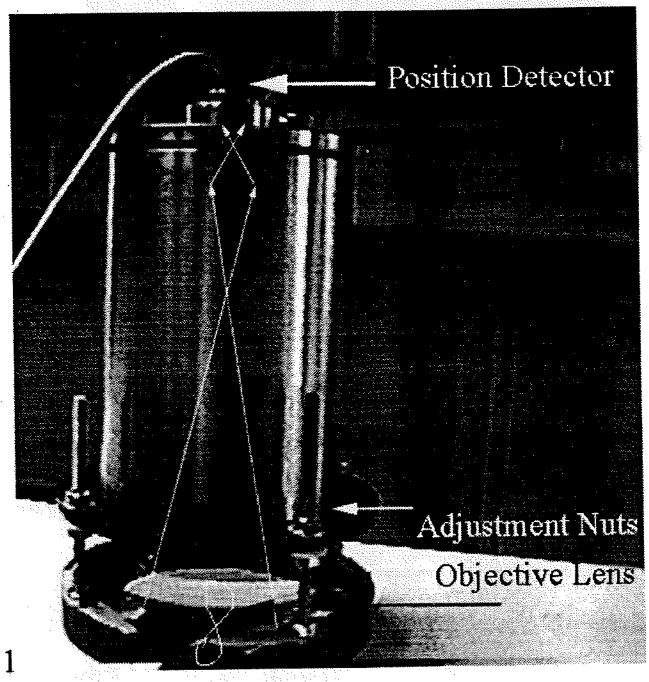

Fig. 9 The optical mapping system with the objective lens, lens adjustment screws and the position sensor on top and an ocular lens inside

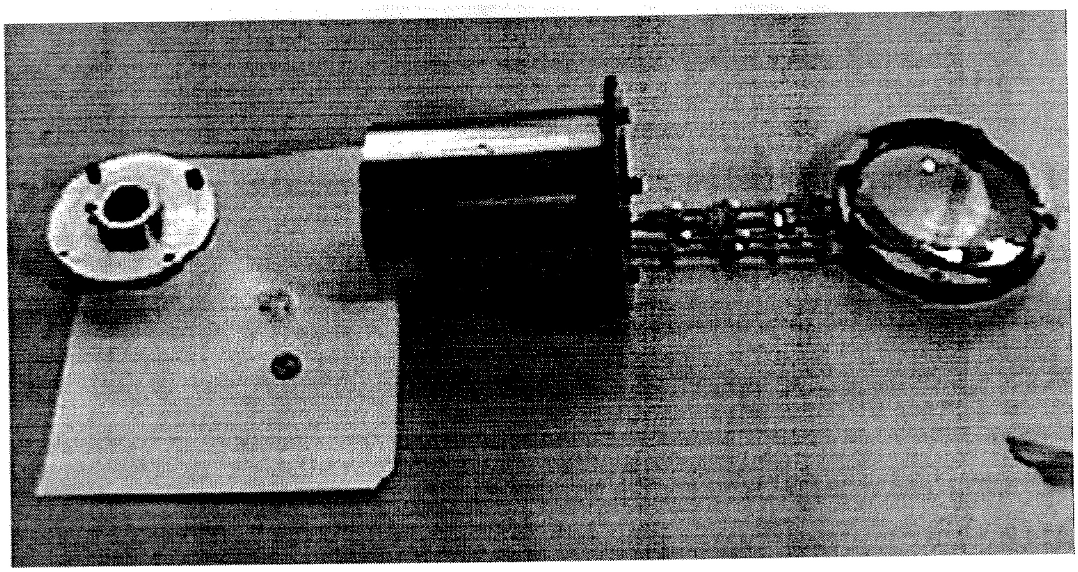

Fig. 10 Inner components of the optical setup

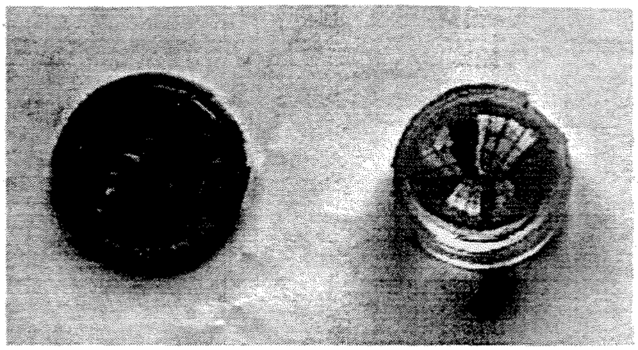

Fig. 11 Ocular lens inside

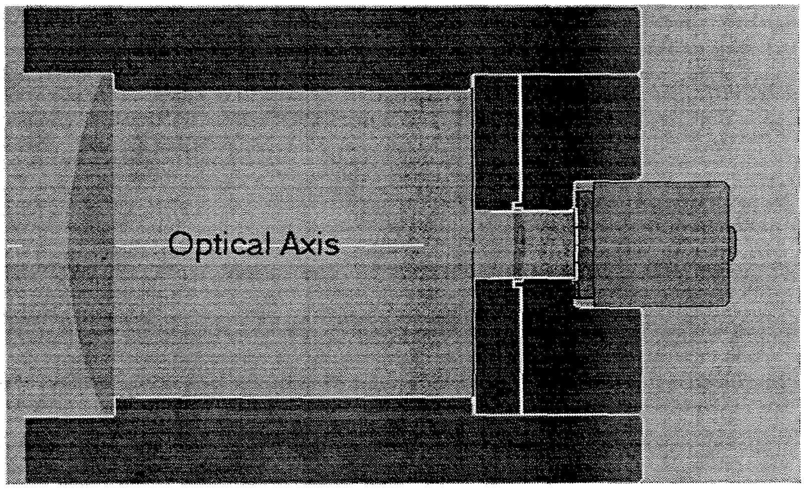

Fig. 12 The optical setup, the two lenses and the position detector inserted on the right

Due to the short length of the setup, thick lenses were used that would not allow a linear or bifocal mapping (spherical aberration). The distance between the two lenses were adjusted in such a manner as to minimize the nonlinearity of the mapping and the overall calibration. The large cylinder diameters called for in the low mass ratio cases (the *R* series) gave rise to slightly more non-linearity in the *R* runs (see Fig. 14). The smaller cylinder diameters *D* and the smaller amplitudes *A/D* achieved in the high mass ration cases (the *S* series) made the corresponding calibrations more linear.

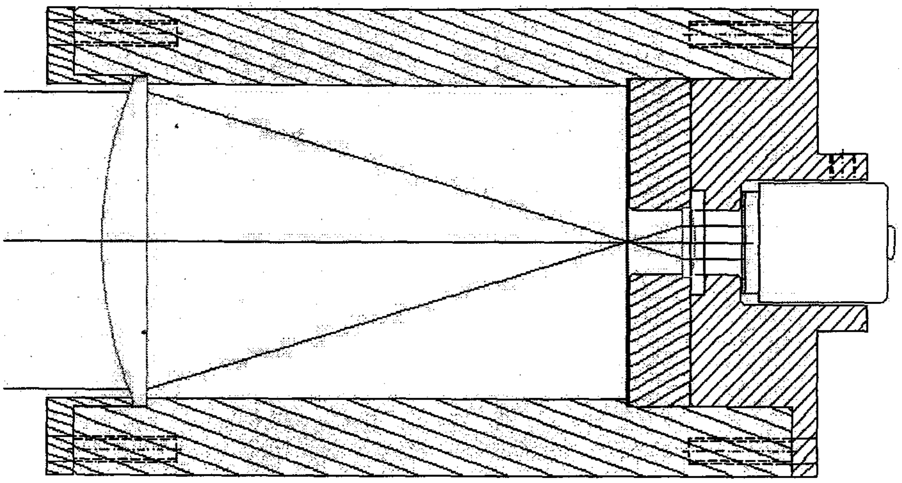

Fig. 13 The optical mapping for a bifocal system

The calibrations shown in Fig. 14 and Fig. 15 were obtained by recording the final acquired voltage (amplified signal from the photo position sensor sampled by Superscope) for each incremental displacement of the traverse. The calibration was repeated in both *R* and *S* experimental series at least four times, before, during and after the experiments. In order to subtract the offset values in voltage *Vy[Volts]* and displacement *y [in]*, each data set was first fitted to a 3rd degree polynomial. The inflection point for each set of data was then calculated from the coefficients of the polynomial and subtracted from the data in order to shift all data to a common center at the origin. After two iterations of the above procedure, the polynomial fits contained large odd terms with even term coefficients that were at least 6 orders of magnitude smaller. All calibration data for each series (*R* or *S*) were then combined to find a final fit to all data.

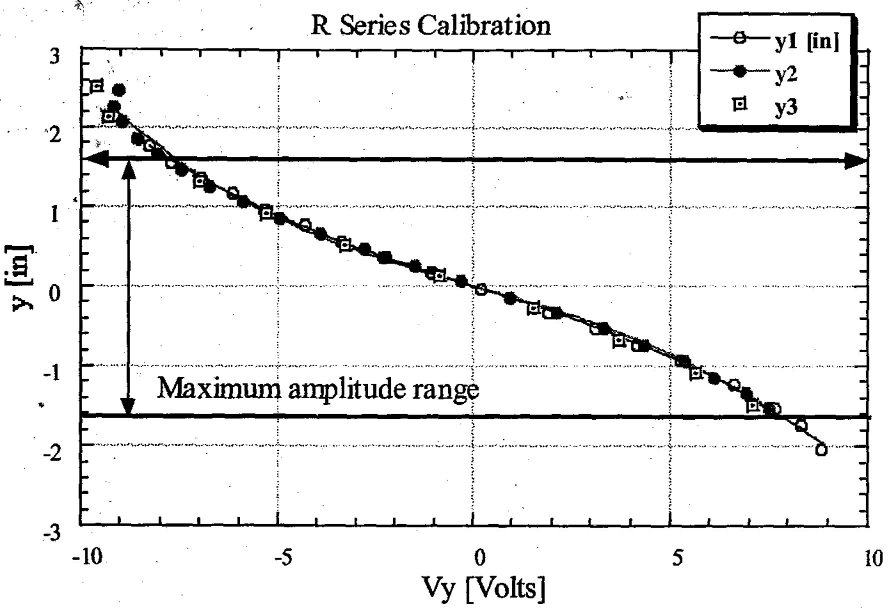

Fig. 14 The optical calibration for the R cases ($m^*<10$) and the maximum range achieved (A_{max} in case *R3*)

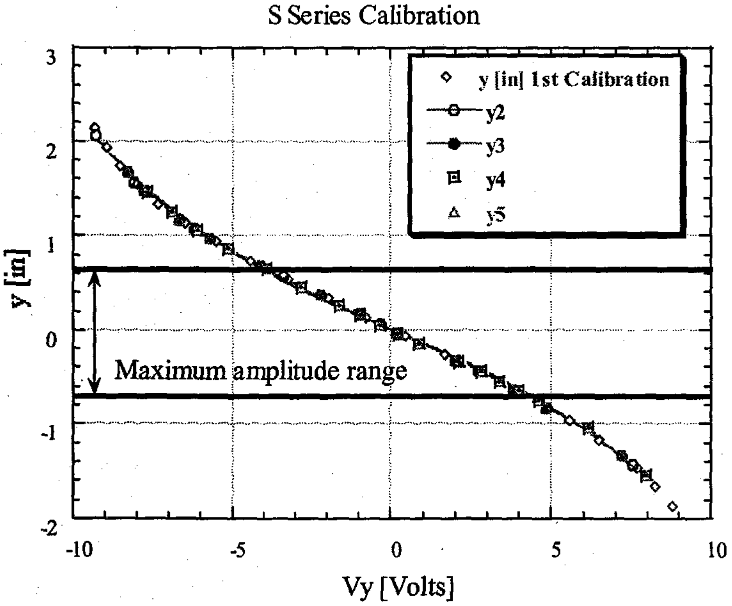

Fig. 15 The optical calibration for the *S* cases ($m^*>10$) and the maximum physical amplitude achieved (A_{max} in case *S1*)

The final polynomial fit for R series was as follows:

$$y[inch]=3.48\times10^{-7}-0.1475Vy+1.37\times10^{-8}Vy^2-1.025\times10^{-3}\,Vy^3$$

The final polynomial fit for S series was as follows:

$$y[inch]=6.34\times10^{-5}-0.1516Vy+5.72\times10^{-8}Vy^2-6.39\times10^{-4}\,Vy^3$$

The offset and the even terms are negligible and the calibration polynomial can be considered an odd function as expected. This reassures us that the challenging task of aligning and positioning the laser beam and the optics was performed correctly.

Is is also worth noting that any error in the non-linear calibration can be a possible source of problems in the force deduction technique discussed in chapter 6. This is mainly due to the fact that higher derivatives amplify the effect of a nonlinearity. Assuming the calculated displacement, yc, to be a nonlinear perturbation of the true displacement, y, we have:

$$y_c=y(1+\alpha y+\beta y^2)$$

which yields the following second derivative:

$$y_c''=(2\alpha+3\beta y)y'^2+(1+2\alpha y+3\beta y^2)y''$$

Since the y and its derivatives are $O(1)$ after non-dimensionalization, the 1st order error in yc'' is proportional to the nonlinear coefficients α nad β. Considering the ratio of the non-linear to linear coefficients in the above calibration polynomials would suggest that such an error would be at most $O(-2)$ if we assume that the calibration error is as large as the nonlinear terms present, i.e. the difference between a linear and a non-linear calibration.